Multimodal ventricular tachycardia analysis: towards the accurate parametrization of predictive HPC electrophysiological computational models

Ph.D. Thesis

Mariña López Yunta

Computer Applications in Science & Engineering dpt.
Barcelona Supercomputing Center (BSC)

Doctorat en Matemàtica Aplicada
Universitat Politècnica de Catalunya

June 2018

Multimodal ventricular tachycardia analysis: towards the accurate parametrization of predictive HPC electrophysiological computational models

Submited in partial fulfillment of the requirements for the Ph.D. Degree in Applied Mathematics

Mariña López Yunta

Advisors

Dr. Mariano Vazquez

Dr. Jazmín Aguado-Sierra

Computer Applications in Science & Engineering dpt.
Barcelona Supercomputing Center (BSC)

Doctorat en Matemàtica Aplicada
Universitat Politècnica de Catalunya

June 2018

Agradecimientos

Ahora que por fin termina este proceso quería agradecer su ayuda a todas las personas que en algún momento me dieron apoyo para seguir adelante.

Para empezar quería mencionar especialmente a David Filgueiras, que desde el CNIC ha hecho posible que este trabajo salga adelante. Me ha descubierto en mundo de la cardiología y me ha ayudado en todo momento para dar sentido a esta tesis. Quiero agradecer su trabajo como codirector de la tesis, a pesar de que por aspectos burocráticos no figure como tal. Y quiero dar la gracias a mis directores de tesis Mariano y Jazmín, por contratarme y darme la oportunidad de realizar este trabajo.

A todos los compañeros de CASE quiero darles las gracias por estar siempre dispuestos a ayudar con cualquier duda. En especial quería agradecer su ayuda a Eva, por introducirme en el mundo de Alya y los sólidos; Alfonso y Matias, ahora ya señores doctores, por todas las conversaciones para arreglar miles de dudas y para sobrevivir al doctorado (Alfonso gracias por la revisión de esta tesis). También quería mencionar a los mallasmen, Xevi y Abel, gracias por haberme ayudado muchas veces a seguir para adelante. Por supuesto a María, compañera de los cotilleos, las conversaciones en bucle y las cervezas de los viernes. Y también al resto de doctorandos de CASE: Simon, Jordi, Federica, Pastrana, ... Además quiero dar la gracias a Laura por sustentar el departamento y organizar los retreats!

Como es lógico, las comidas son el mejor momento del día. Yo necesito desconectar del ordenador y socializar con buena compañía, así que gracias a Albert, Claudia, Raul, María y Natalia. Y los viernes menos mal que nos adoptaron en el equipo Repsol.

Por supuesto, tengo que dar las gracias a Natalia por acompañarme en este camino, escuchar mis rollos mentales infinitas veces, aguantar mis nervios, ayudarme y hacerme sentir casa :)

Cunado uno se va lejos de casa, siempre está bien tener una secta de gallegos cerca. Así que gracias a Paula, Nacho, Lydia, Elena y Dorribo (y a las charlas de doctorandos anónimos) por formar la nuestra en Barcelona.

Los miércoles de fútbol fueron un gran momento para desconectar de todo y planear la fiesta del finde, gracias por la fiestas y partidos a todas a las que han ido pasando por el equipo Undercover.

Y por supuesto dedicárselo a mi familia. A mi madre porque aunque estemos lejos por teléfono podemos reír, rollar y contarnos todo sin que se note la distancia. A mi padre por confiar siempre en mi. A mi hermano Carlos. A mi abuela. Y también a Minia, María y Manuel. A mi familia de Barcelona, sobretodo a mi tía y mi abuelo. Y también a mis tíos de Sevilla.

También quiero acordarme de todos mis amigos de Galicia. De los Clementinos, aunque superviejas glorias, seguimos siéndolo cada vez que nos encontramos en cualquier parte del mundo: Irene, Juan, Anhyela, Alberto, Samu, Óscar, Ana, Sara, Elena, Pedro, ... De las de Vigo. De las matemáticas: las Marías y Natalia. Y también de las catalanas de París, que me ayudaron a no aburrirme cuando llegue a Barcelona.

Por último, agradecer a todos los profesores de matemáticas que he tenido desde que era pequeña hasta ahora (aunque no se vayan a enterar de esto). He tenido la suerte de que, además de gustarme las matemáticas, me he encontrado con profesores transmitían ganas de descubrirlas y proponían retos que eran como juegos para mi. También gracias a ellos he llegado hasta aquí.

Este trabajo ha sido posible gracia a la financiación del ministerio de economía y competitividad bajo el proyecto Severo Ochoa (SEV-2011-00067), mediante la beca FPI-SO (SVP-2013-067908).

Abstract

After a myocardial infarction, the affected areas of the cardiac tissue suffer changes in their electrical and mechanical properties. This post-infarction scar tissue has been related with a particular type of arrhythmia: ventricular tachycardia (VT). A thorough study on the experimental data acquired with clinical tools is presented in this thesis with the objective of defining the limitations of the clinical data towards predictive computational models. Computational models have a large potential as predictive tools for VT, but the verification, validation and uncertain quantification of the numerical results is required before they can be employed as a clinical tool.

Swine experimental data from an invasive electrophysiological study and Cardiac Magnetic Resonance imaging is processed to obtain accurate characterizations of the post-infarction scar. Based on the results, the limitation of each technique is described. Furthermore, the volume of the scar is evaluated as marker for post-infarction VT induction mechanisms.

A control case from the animal experimental protocol is employed to build a simulation scenario in which biventricular simulations are done using a detailed cell model adapted to the ionic currents present in the swine myocytes. The uncertainty of the model derived from diffusion and fibre orientation is quantified. Finally, the recovery of the model to an extrastimulus is compared to experimental data by computationally reproducing an S1-S2 protocol.

Results from the cardiac computational model show that the propagation wave patterns from numerical results match the one described by the experimental activation maps if the DTI fibre orientations are used. The electrophysiological activation is sensitive to fibre orientation. Therefore simulations including the fibre orientations from DTI are able to reproduce a physiological wave propagation pattern. The diffusion coefficients highly determine the conduction velocity. The S1-S2 protocol produced restitution curves that have similar slopes to the experimental curves.

This work is a first step forward towards validation of cardiac electrophysiology simulations. Future work will address the limitations about optimal parametrization of the O'Hara-Rudy cell model to fully validate the cardiac computational model for prediction of VT inducibility.

Resumen

Tras un infarto de miocardio, las zonas de tejido cardiaco afectadas sufren cambios en sus propiedades eléctricas y mecánicas. Este substrato miocárdico se ha relacionado con la taquicardia ventricular (TV), un tipo de arritmia. En esta tesis se presenta un estudio exhaustivo de los datos experimentales adquiridos con protocolos clínicos con el objetivo de definir las limitaciones de los datos clínicos antes de avanzar hacia modelos computacionales. Los modelos computacionales tienen un gran potencial como herramientas para la predicción de TV, pero es necesaria su verificación, validación y la cuantificación de la incertidumbre en los resultados numéricos antes de poderlos emplear como herramientas clínicas.

La caracterización precisa del sustrato miocárdico, cicatriz, se realiza mediante el procesado de los datos experimentales porcinos obtenidos del estudio electrofisiológico invasivo y la resonancia magnética cardiaca. Como consecuencia, se describen las limitaciones de cada técnica. Ademas, se estudia si el volumen da la cicatriz puede actuar como indicador de la aparición de VT.

El escenario de simulación para los modelos computacionales biventriulares se construye a partir de los datos experimentales de un caso control incluido en el protocolo experimental. En el, se realizan simulaciones electrofisiológicas empleando un modelo celular detallado adaptado a las propiedades de las corrientes iónicas en los miocitos de los cerdos. Se cuantifica la incertidumbre del modelo generada por la difusión y la orientación de las fibras. Por ultimo, se compara la recuperación del modelo a un extraestímulo con datas experimentales mediante la simulación de un protocolo S1-S2.

Los resultado numéricos obtenidos muestran que los patrones de propagación de la onda de las simulación cardiaca coinciden con los descritos por los mapas de activación experimentales si la fibras incluidas en el modelo corresponden a los datos de DTI. El modelo de activación es sensible a la orientación de fibras impuesta. Las simulaciones incluyendo la orientación de fibras de DTI es capaz de reproducir los patrones fisiológicos de la onda de propagación eléctrica en ambos ventrículos. El velocidad de conducción obtenida es muy dependiente del coeficiente de difusión impuesto.

El protocolo S1-S2 protocolo genera curvas de restitución con pendientes simulares a las curvas experimentales.

Esta tesis es un primer paso hacia la validación de las simulaciones electrofisiológicas cardiacas. En el futuro, se mejoraran las limitaciones relacionadas con una optima parametrización del modelo celular de O'Hara-Rudy para validar por completo el modelo computacional cardiaco para avanzar hacia la predicción de la predicción de VT.

Contents

Agradecimientos **v**

Abstract **vii**

Resumen **ix**

1 Introduction **1**

1.1 Motivation 1

1.2 Biological background 2

1.2.1 Anatomy and function 2

1.2.2 Cardiac electrophysiology 4

1.2.3 Infarct-related ventricular tachycardias 7

1.3 State of the art review 8

1.3.1 Post-infarction scar characterization 8

1.3.2 Computational cardiac simulations 9

1.3.3 Current challenges 11

1.4 Goals and contributions of this thesis 12

1.5 Structure of this thesis 14

I Post-infarction substrate characterization and clinical implications **17**

2 Experimental protocol and data acquisition **19**

2.1 Animal model of myocardial infarction 20

2.2 Cardiac Magnetic Resonance (*in vivo*) 21

2.3 Electrophysiological study 22

2.3.1 Electroanatomic mapping 23

2.3.2 Ventricular stimulation protocol 24

2.3.3 Activation maps 24

2.4 Cardiac Magnetic Resonance (*ex vivo*) 25

2.4.1 Explanted heart preparation 25

2.4.2 CMR *ex vivo* sequences 26

3 Data processing 29

3.1 Electrophysiological data processing 29

3.1.1 Scar definition on electroanatomical maps 30

3.2 Segmentation of post-contrast CMR 32

3.2.1 Ventricle segmentation 32

3.2.2 Scar segmentation 33

3.2.3 Dense scar characterization 43

3.3 Integration of EAM and CMR scar on a surface 45

3.3.1 Surface Registration 47

3.3.2 Scar projection 52

3.4 Fibre orientation from DTI 56

4 Implications of infarct-related scar characterization 59

4.1 Multi-modal scar characterization 60

4.1.1 Electrophysiological scar characterization 61

4.1.2 Volume scar characterization from post-contrast CMR 63

4.1.3 Comparisons of voltage-based substrates with surface scar projections from CMR 65

4.1.4 Interpretation of voltage maps based on post-contrast CMR scar descriptions. 69

4.2 Ventricular arrhythmia inducibility 71

4.2.1 Left ventricle ejection fraction analysis 71

4.2.2 Scar volumes from *ex vivo* post-contrast CMR 72

4.2.3 Scar volumes from *in vivo* post-contrast CMR 73

4.3 Main conclusions of experimental study 75

II Electrophysiological simulations 77

5 Computational electrophysiology model 79

5.1 Governing equations 79

5.1.1 Ionic cell model 83

5.2 Computational implementation 84

5.2.1 Solving strategy 85

5.3 Alya 86

6 Simulation scenario 89

6.1 Geometry discretization 89

6.1.1 Mesh for controls 91

6.2 Fibre orientation 93

6.2.1 DTI 93
6.2.2 Rule-based model 94
6.3 Electrical characterization of the problem 95
6.3.1 Pacing point location 95
6.3.2 Wave propagation velocity 96
6.4 Computational electrophysiology experiments methodology . 99

7 Computational simulations results 101
7.1 Electrophysiological model verification 101
7.2 Sensitivity analysis to diffusion 104
7.3 Control case 107
7.3.1 Numerical and experimental description of a beat . . . 108
7.3.2 S1-S2 protocol to compare experimental and simulated restitution curves 112
7.4 Main conclusions of computational electrophysiology experiments 115

8 Discussion, limitations and future work 117
8.1 Discussion 117
8.2 Limitations 120
8.3 Achievements of this thesis 122
8.4 Future work 123
8.5 Scientific Work 125

Chapter 1

Introduction

1.1 Motivation

Post-infarct patients are prone to suffer sudden death. After a myocardial infarction (MI) there is a change on tissue properties in the affected areas. In some cases, these changes can induce arrhythmias that cause sudden death. The risk stratification of ventricular tachycardia (VT), a type of arrhythmia related with post-infarction substrate, is still not well understood. Currently, there are many open question related with protocols performed to stratify the risk of sudden death in patients that have suffered MI [2].

Many engineering tools have been developed in the last decades to facilitate the diagnosis and treatments. Cardiac Magnetic Resonance (CMR), electrocardiogram, echocardiography or electroanatomic mapping (EAM) have been introduced in the clinical protocols to help on the early diagnosis and therapies employed in cardiovascular diseases.

However, there is a lack of consensus about how evaluate the risk of VT based on mentioned tools. It seems necessary to review the interpretation of the data extracted from imaging and invasive tools. We aim to describe the limitations of each technique and evaluate any image-derived marker that can act as a predictor for VT.

Moreover, the cardiac simulations field is an under development tool with potential applications as predictive models. Computational simulations could help doctors to know in advance how patients will evolve, i. e. predict VT episodes, and reduce the number of animal experimental studies. Electrophysiological models are able to reproduce the cardiac beat of healthy and pathological heart from the organ level. It is however important that computational models are validated and approved by medical and regulatory agencies before they can be applied on patients [63].

Following a path of Verification, Validation and Uncertainty Quantification (VVUQ) protocols is key to assure computational cardiac simulations are correct. In this thesis we aim to work in this direction and evaluate how our inhouse code Alya can reproduce the electrical activity of a healthy heart comparing with the experimental data. To do so, we want to create a data processing pipeline able get the best structural and electrical description of the heart, based on hight quality animal experimental data, and run the cardiac simulations based on it. Our main motivation is to provide comparison between numerical and experimental propagation patterns of the cardiac beats. This is fundamental step to advance to a validation of the models, before moving into pathological simulations.

The strong interdisciplinary field needs the interaction of cardiologists, engineers, biologists and mathematicians to go from the experimental medical data towards cardiac computational models. The work described in this thesis comes from a close collaboration between Barcelona Supercomputing Center (BSC) and the Spanish National Center for cardiovascular research (CNIC). This work try to answer some of the questions that cardiologists of CNIC have regarding post-infarction VT.

1.2 Biological background

1.2.1 Anatomy and function

The heart is the main organ of the cardiovascular system, it is in charge of pumping blood to the body. It is composed by four cavities, right ventricle (RV), left ventricle (LV), right atria (RA) and left atria (LA). The left and right heart cavities are divided by the septum, a muscle wall between them. The main external three dimensional views of the heart are called anterior and posterior view, as showed in Figure 1.1.

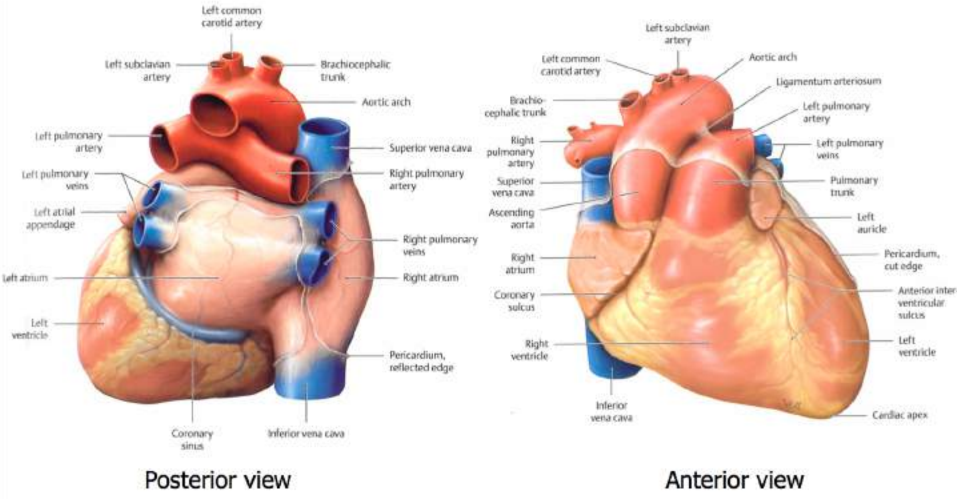

Figure 1.1: Biological background. Anatomical scheme of the heart from a posterior and anterior view. Image modified from [80]

The influx of blood in the heart is regulated by four valves: left atria (LA), tricuspid valve (TriV), aortic valve (AV) and pulmonary valve (PV). The plane formed in the top of ventricles by the valves dividing atria and ventricles is called base. The lowest part of the ventricles is called the apex.

Myocytes. The muscular tissue of the heart is composed by myocytes, muscular tubular cells relatively short. Myocytes have two main functions: electrical conduction and mechanical contraction. They are organized in fibres, which in turn from laminar sheets. The cardiac fibres orientation define the way the electrical impulse is propagated and how the cardiac muscle contracts.

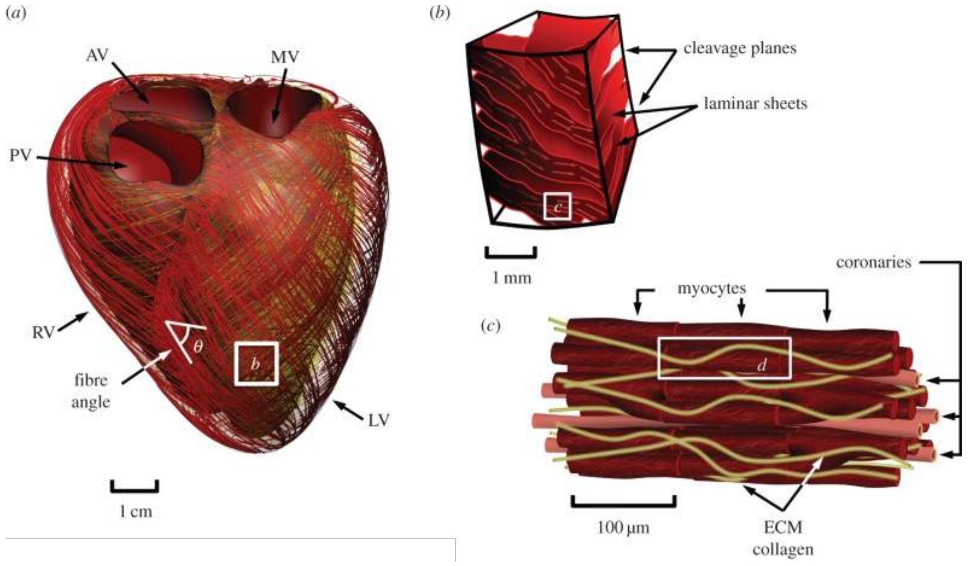

Figure 1.2: Biological background. Scheme of ventricle fibre orientation (a), laminar sheers of fibres (b) and myocytes joined to from fibres (c). Image modified from [20].

From the outside to the inside, the heart can be divided into three layers: epicardium (EPI), myocardium and endocardium. Endocardium includes the inner layer of left and right cavities (LV endocardium and RV endocardium). Fibre orientation changes through them. On the outer layer, epicardium, fibres are oriented approximately with $\theta = +60°$ and on the inner layer, endocardium, fibres have an angle of $\theta = -60°$ of the heart (Figure 1.2).

Cardiac function. The main function of the heart is to pump blood to the rest of the body. The RV pushes de-oxygenated blood into lungs and the LV pushes oxygenated blood to the systemic circulation. As the afterload of the LV is higher, compared with the RV, it has thicker walls. The blood from veins enters on the RV or LV and passes to the RV and LV, respectively, through valves. Finally, the blood is pumped into the arteries. The four valves regulate the blood flow inside the heart, as shown in Figure 1.3.

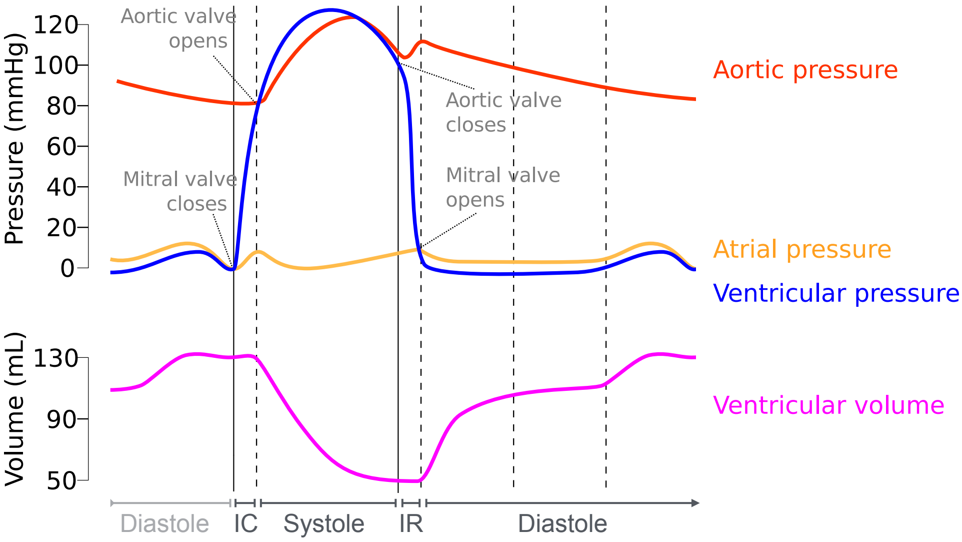

Figure 1.3: Biological background. Changes of cardiac pressure and ventricle volume during the four phases of the cardiac cycle.

The cardiac cycle can be split in four different phases: isovolumic contraction (IC), systole and isovolumic relaxation (IR) and diastole. When ventricles start to contract, the IC begins. It is a short phase when the intracavity pressure rises without changing ventricle volume. Systole starts with the opening of the aortic valves, that occurs when the intraventricular pressure rises above the pressure on the arteries. This phase ends when the ventricular and aortic pressures return to equilibrium and the aortic and pulmonary valves are closed. This leads to the isovolumic relaxation of the ventricles. In this phase, volume is constant while the intracavity pressure drops until it is low enough to open the atrioventricular valves. The pressure differences between the atrial and ventricular cavities let the blood flow from the atrium to the ventricles during diastole. The described cycle is regulated by electrical impulses that generates cardiac contraction.

1.2.2 Cardiac electrophysiology

A heartbeat starts with ion fluxes through the myocyte membrane that create a transmembrane potential that propagates through the myocardial tissue. A specialized type of myocardial cells, placed in defined areas of the heart, builds a branching structure called conduction system that orchestrate the cardiac activation. The sinoatrial node acts as a pacemaker spontaneously starting depolarization without external stimulus. This stimuli is therefore propagated through the conduction system to the rest of the heart.

The electrical impulse, generated in the sinoatrial node, depolarises the atria starting contraction. The electrical impulse is transmitted through the internodal fibres to the atrioventricular node located in the septum. The bundle of His is split into two, each resulting bundle goes to a ventricle and forms the Purkinje fibres in the endocardium that transmit the impulses to both ventricles (Figure 1.4). When the impulse arrives to the Purkinje fibres, both ventricles are almost instantaneously depolarized, producing the systolic phase of cardiac cycle.

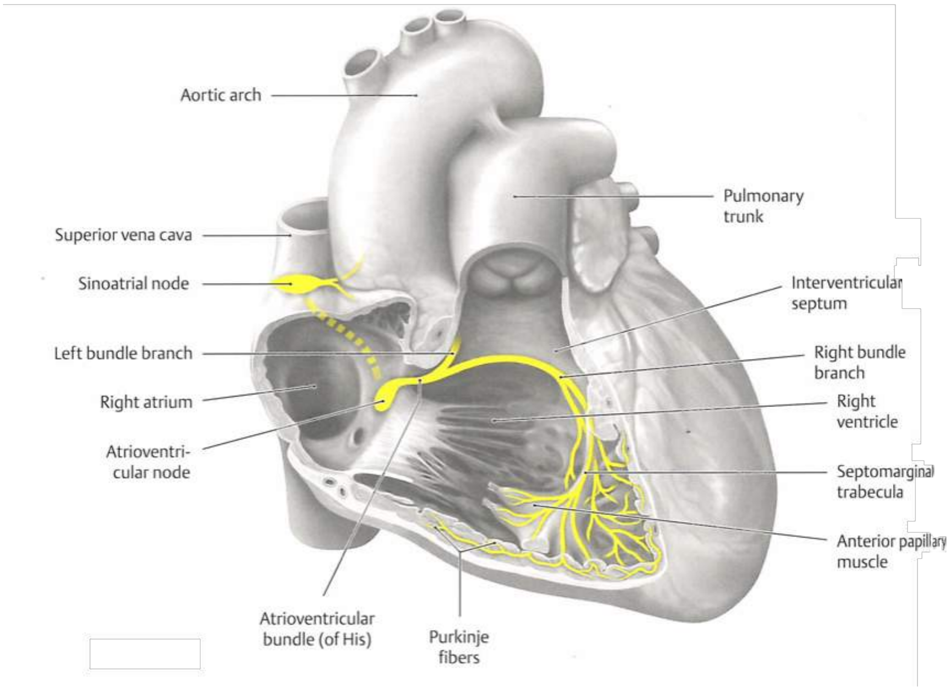

Figure 1.4: Biological background. Scheme of the cardiac electrical conduction system.Image from [80]

Action potential. Describes the change in the transmembrane potential of the myocyte. When the cell gets activated, the ion channels trigger the cell depolarization. The propagation of the action potential is possible thanks to the membrane structures composed by several intercellular ion channels, called gap-junctions, that make communications easier between myocytes. Four phases compose the entrance of positive charges, Ca^{2+} and Na^{+}, that initiates the action potential (Figure 1.5).

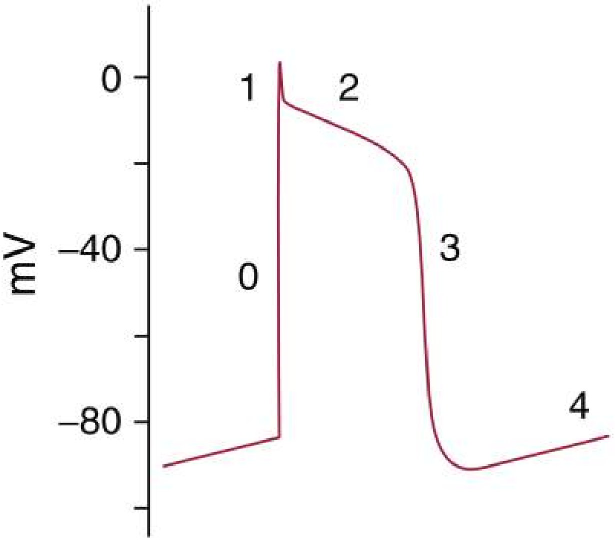

Figure 1.5: Biological background. Action potential scheme indicating the four phasesof cardiac myocites [32].

Action potential phases

0-Depolarization: Na^+ enters into the cell thanks to the opening of Na^{2+} channels. A rapid depolarization of the cell occurs.

1-Early repolarization: Repolarization starts when the cell reach the maximum depolarization. The fast Na^+ channels are inactivated and K^+ ions go out of the cell.

2-Plateau: The cell tries to equilibrate the Ca^{2+} entrance and K^+ exit. Ca^{2+} is liberated from the sarcoplasmic reticulum of cells causing the myocytes contraction.

3-Complete repolarization: Ca^{2+} channel are closed and K^+ channels are open. Potassium exits the cell until resting membrane potential is reestablished at ~ -90 mV.

4-Rest: The cell is repolarized and membrane potential is ~ -90 mV.

The action potential duration (APD) is defined as the length of the action potential. The APD at 90% of repolarization is denoted by APD_{90} and by APD_{50} at 50% of repolarization. The diastolic interval (DI) is defined as the time between 90% repolarization and the start of the next beat. The effective refractory period (ERP) is the time between the starting of a beat and the time it takes for the cell to became excitable again. These definitions help to characterized an action potential.

Electrocardiogram (ECG). The cardiac electrical impulse can be registered by electrodes placed on the skin. The electrical activity phases of the cardiac cycle can be visualized using ECG. The ECG plot has three main features: the P wave, the QRS complex, and the T wave. The P wave is produced by the atrial depolarization, the QRS complex by the ventricular depolarization and the T wave by the ventricular repolarization. The atrial repolarization is a small wave hidden inside the QRS complex.

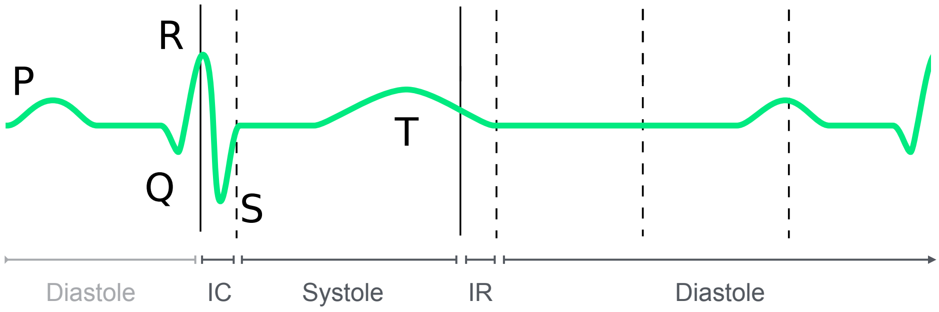

Figure 1.6: Biological background. Electrocardiagram of a cardiac beat

1.2.3 Infarct-related ventricular tachycardias

Myocardial infarction (MI) occurs when there is an occlusion of the coronary arteries. The blood is not able to reach some areas of ventricles producing ischemia. The affected areas of the myocardium gets damaged, which creates a particular substrate called scar. In this pathological tissue, the electrical and mechanical properties change. There is a remodelling effect in the affected myocardial tissues. This tissue undergo changes in shape and in size during the recovery period after a MI. The remodelling changes may lead to monomorphic VT, a type of arrhythmia strongly related with sudden death after MI.

The post-infarction scar can be classified into dense and heterogeneous. The dense scar has no surviving myocytes, so no intrinsic electrical activity. The heterogeneous scar is an intermingling of viable myocyte and collagen with potentially slow conduction velocity areas. The re-entry channels causing VT seem to be related with heterogeneous scar, where some slow conduction channels appear.

Re-entrance is an arrhythmic mechanism that occurs when ventricle areas, that were not activated with the initial depolarization wave, are excited before the impulse disappears. Therefore, areas that have recovered from the initial depolarization are re-excited. The criteria to identify the re-entry circuits are [8, 85]:

- Unidirectional conduction block.

- Excitatory wave progresses along a distinct pathway, returning to its origin and following the same path again.
- Interruption of the re-entrant circuit at any point along its path should terminate the circuit re-activation.

In the case of post-infarction VT, re-entry appears around an anatomical obstacle. A tissue that can sustain circular wavefronts, a substrate where conduction and refractory condition change and a block zone given by inexcitable tissue, are needed to starts the re-entry. Low conduction areas produce a delay on the wavefront, so the areas around unidirectional block can recover.

After an infarction, the ventricular remodelling modifies the volume and shape; plus electrical properties change on the affected areas of the heart. As a consequence, in post-infarcted hearts, there is an inexcitable area, a dense scar, and a low conduction zone, i.e. the heterogeneous scar. This generates an electrophysiological and anatomical substrate where an unidirectional wave can begin the re-entry circuit.

1.3 State of the art review

1.3.1 Post-infarction scar characterization

Imaging tools are able to characterize the behaviour of normal and pathological hearts. In particular, post-infarction scar can be defined using different tools, such as EAM, CMR or *post mortem* histology. The characterization of the scar is a fundamental step when studying the mechanisms that trigger a VT on post-infarct patients.

Currently, the left ventricle ejection fraction (LVEF) is the main criteria employed in clinical protocols to evaluate the risk of sudden death [2], although it has been reported that it is not directly related [38, 27, 22]. In consequence, the post-infarction substrate characterization is crucial to study the mechanisms that trigger a VT on patients and to find VT risk markers that help on patient stratification. In addition, the scar description is also important in computational models, that are tools under development that could help to predict VT.

The scar form EAM can be described by voltage criteria on electroanatomic maps [76]. This tool is employed for ablation treatment in patients suffering VT that show no improvement with antiarrhythmic drugs. Only subendocardial and subepicardial scar description are available, as no transmural information can be obtained using EAM. In addition, the accuracy of the scar definition depends on the catheter employed during the electrophysiological study [95].

Contrast enhanced CMR has been described as the preferred tool to evaluate structural changes in infarct areas of the heart [96]. A three dimensional description of the scar is obtained through segmentation, including transmural scar. The main limitation of this technique is the lack of a standard procedure for scar segmentation [40]. Furthermore, the scar definition can be affected by partial volume effects [79]. In the literature, we can find contradictory studies relating scar volume and VT [44, 17]. The reported range of scar volumes associated with VT and the range of scar volumes not associated wit VT are overlapped. Those results might be the reason why scar volume quantification from CMR is still not incorporated with clinical protocol for evaluating the risk of VT.

The structural changes produced during MI and the posterior remodelling affect fibres. The Diffusion Tensor Imaging (DTI) is a CMR sequences able to describe fibres orientation. But this technique is under development for *in vivo* image acquisition, nowadays it has a low precision and accuracy [59]. On the contrary, *ex vivo* procedures have shown good results for describing fibre orientation [82]. Some groups have suggested the relevance of fibre orientation on the initiation and maintenance of VT [7], but it is still an open question.

Most of the studies comparing scar definition from imaging and invasive tools only include *in vivo* techniques, with low resolution [5, 90]. Moreover, none of these studies include the analysis of both ventricles. The RV endocardium is not studied due the complexity added by the RV geometry. In addition, there is not a standard methodology to perform EAM-CMR comparisons and the optimal thickness of the subendocardial or subepicardial layer from post-contrast CMR compared against electroanatomic maps is unknown.

Establishing limitations of each imaging tool would help to quantify the accuracy of scar definitions, so that we can understand some of the contradictions between studies relating scar volume with VT induction. Computational models are still under development, but they have the potential to become in the close future a powerful tool for predict VT [92].

1.3.2 Computational cardiac simulations

Cardiac computational models can reproduce the electrical propagation through the myocardium. The first electrophysiological cell model was proposed to describe transmembrane voltage in a neuron axon by Hodgkin and Huxley in 1952 [33]. A simplified model for excitable media that has been modified and used for cardiac modelling is the one published by Fitzhugh and Nagumo in 1961. However, the first cardiac cell model was published by Denis Noble in 1962, a purkinje cell model. Phenomenological models have been evolving to more complex ones.

Nowadays, cell models are more complex and include systems of ordinary differential equation fitted to experimental measures of transmembrane ion currents. We highlight two models that have described the human ion kinetics, the one proposed by Ten-Tusscher in 2004 [91] and the one proposed by O'Hara and Rudy in 2011 [61]. Cell models are used to simulate the normal and pathological electrical activity of the heart, for example under complex depolarization patterns like re-entrance [71, 57]. Despite detailed cell models are preferred due to the physiological description of the transmembrane currents, these are more computationally expensive and rely on a large set of parameters difficult to personalize.

Moreover, creating a simulation scenario based on experimental medical data is not straightforward. We need to face several problems such as: cardiac and scar geometry definition, mesh generation, fibre orientation description, boundary conditions and model parametrization. In this thesis an effort has been done in the pre-processing part, the experimental data processing. Based on experimental medical data, we create an optimal simulation scenario.

For VT simulation, the electrophysiological models employed must be able to reproduce pathological dynamics of wave propagation in the myocardium, such as re-entrant circuits in the tissue level. Also, the models must be prepared to introduce changes on the electrical properties of normal and scar tissue during the parametrization of the model. The Priebe and Beuckelmann model was proposed in 1998 to study the consequences of heart failure included 5 ionic currents defined in human myocytes [68]. A simplified version of this model was proposed in [14]. In 2004, the Ten-Tusscher model was proposed [91] that includes almost all the human cell ion currents. The model proposed by Bueno-Orovio in 2008 improved the computational aspects of the model with a good capability to reproduce in detail the human action potential. In [18], it was presented a comparison of the mentioned electrophysiological models by reproducing a two dimensional re-entry circuit. More recently, in 2011 the O'Hara-Rudy model was proposed. This human electrophysiological model was able to simulate the main arrhythmogenic phenomena [61]. This last model was the one chosen for the simulations performed in this thesis.

The definition of the scar is a key step to parametrise the pathological model that want to simulate VT. Changes on the electrical and structural properties that occurs due to remodelling in the infarct areas are set on the scar defined from post contrast CMR segmentations [94].

The complex parametrization process of the electrophysiology models makes difficult the translation into clinics. It is however important that computational models are validated and approved by medical and regulatory agencies before they can be applied on patients [63]. An effort in this field must be done to establish validation protocols that can assure computational cardiac simulations are correct before cardiac simulations can be used in clinics. A standard process is needed to perform the verification, validation and uncertainty quantification (VVUQ) of the cardiac simulation that remains an issue [63]. In the cited publication, the verification is defined as *"[...] the process of ensuring that the computational model accurately solves the underlying mathematical model"*. A n-version verification benchmark has been proposed for cardiac electrophysiological models comparing its implementation on different codes [58]. The validation as defined in [63] is *"[...] the process of using data to evaluate the extent that the computational model accurately represents the real-world process which it attempts to simulate"*. Comparing the experimental data against numerical results seems an adequate pipeline for validations, but measuring techniques on biological experimental set-up contain large errors. To deal with this, uncertainty quantification is required. The definition given by [63] describes the uncertainty quantification as *"[...] the process of determining how uncertainty in inputs to the computational model (such as parameters and initial conditions) affect the results of the model"*. The error contained in the input parameters for the numerical models needs to be evaluated [37]. The uncertainty quantification is closely related to sensitivity analysis where the impact of the variation of a input parameters is evaluated in the computational results.

The computational models employed for the cardiac simulations on this thesis have been implemented in Alya, a multiphysics inhouse code able to run fluid-electromechanical cardiac simulations [47, 11, 77]. In this thesis we will focus in electrophysiological simulations, because adding mechanics requires experimental data to validate, such as myocardial tagging sequences of CMR, that was not included in our set of experimental medical data.

1.3.3 Current challenges

Despite imaging and invasive tools have enormously improved during the last decades, the techniques to quantify the risk of developing a post-infarction VT are still an open question. The mechanisms that make re-entry appear and trigger VT are not well defined yet. Despite the lack of specificity of the LVEF, it is included on clinical protocols because none alternative predictor for VT have been accepted. Scar volume from segmented post-contrast CMR could be powerful as a marker, but remains controversial. Evaluating the limitations of the imaging and invasive tools might help to analyse this the relationship between VT and scar volume, and also investigate other markers that trigger VT.

In the cardiac computational field, the validation protocol of the simulations remains an important issue. The complex parametrization process needed and the lack of standard protocol for verification, validation and uncertainty quantification makes harder the translation into clinics.

We have highlighted the main current challenges related with the fields presented in this thesis:

Scar segmentations of CMR. Scar volume analysis directly depends on the scar segmentation. It is essential to find a standard pipeline to get scar segmentations from *in vivo* contrast enhanced CMR to reduce the variability of the published results. In addition, it is also important to describe how the acquisition resolution affects scar segmentation due to partial volume effects.

Thickness of subendocardial layer of EAM. It is known that catheters are able to map subendocardial and subepicardial layers, but it is not possible to map transmural scar. When comparing CMR and EAM, it is crucial to know which is the thickness of the layer mapped by the catheters. Moreover, the interpolation of electroanatomic voltage points must be also taken into account.

VT mechanism. Being able to predict VT requires a good understanding of the mechanism that creates it. Some possible markers such as LVEF or volume of the scar have been mentioned, but it is also important to look for new markers, such as the geometry of the scar, instead of its volume. Also, computational models may provide insights on VT as they allow the measurement, visualization and analysis of the electrophysiology to help the understanding of this type of arrhythmia.

Verification, validation and uncertainty quantification of cardiac computational models. Before computational models can be applied to clinical situations a protocol to evaluate the efficiency and accuracy of the results must be done. This require efforts in the verification, validation and uncertainty quantification (VVUQ) of electrophysiological models.

1.4 Goals and contributions of this thesis

A complete study starting from the experimental medical data acquisition up to computational modelling is presented in this thesis (Figure 1.7).

The experimental data, mainly from imaging tools, is analysed to evaluate its limitations when characterising post-infarction substrate. The clinical implications of this characterization are scar evaluated, including an evaluation of the power of volumetric scar as a VT risk predictor.

Moving into the computational models, a simulation scenario is created based on the experimental medical data. Electrophysiology simulations are preformed using the inhouse code Alya with the main objective of validating the models. It is a fundamental step before moving into VT predictive computational models in further works.

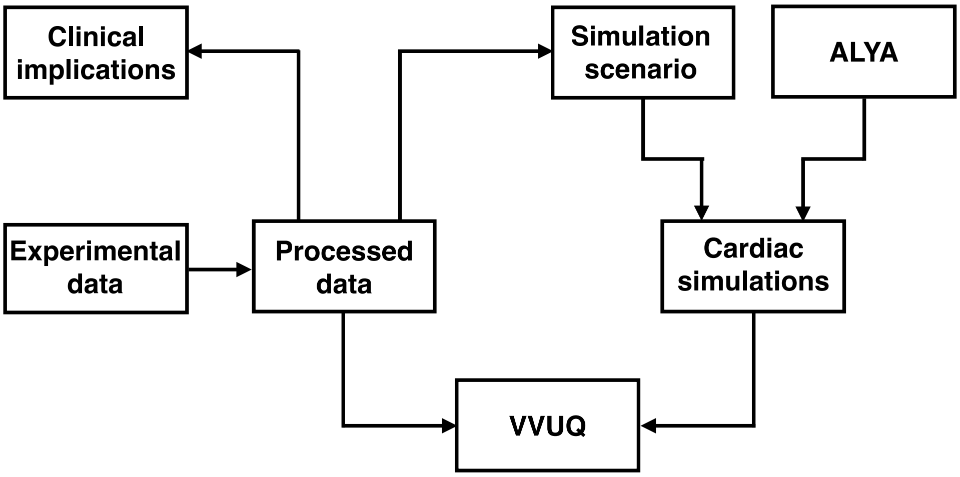

Figure 1.7: Goals and contributions of this thesis. Thesis scheme from experimental data towards computational model validation (VVUQ).

Goals. This thesis has four main goals, the first two related with experimental data processing and the last one with cardiac computational models:

1. Characterized the post-infarction substrate based on clinical imaging and invasive tools against experimental imaging tools.

2. Compare the electrophysiological computational models against experimental data.

The Ph.D. thesis work differentiates from other publications mainly because, to achieve goal (1) the comparisons between CMR and EAM were done in both ventricles, including RV endocardium which is in general not taken into account. Moreover, we have compared EAM and *in vivo* CMR against the *ex vivo* CMR, a higher resolution reference. We have described the limitations of each techniques when describing the post-infarction scar before evaluating its power as a VT predictor. In the case of goal (2), the computational models were compared against electroanatomical maps during pacing. An accurate analysis against experimental data increases the value of the performed simulation. In addition, we have evaluated the role of fibre orientation in cardiac simulation. A fibre orientation description based on mathematical models was included on the models to evaluate the resulting simulations. This algorithm for synthetic fibres is commonly due the difficulty of having DTI, only available on *ex vivo*.

Contributions. The main contributions of this thesis were:

- Expose limitations of clinical imaging tool (*in vivo*).
- Propose an interpretation of the *in vivo* tools for describing post-infarct substrate.
- Characterize the post-infarct substrate by CMR and EAM on both ventricles, and propose algorithms of the pipeline to compare them.
- Comparison of the electrophysiological cardiac simulation from a healthy case (control) against experimental medical data.
- Perform a sensitivity study of the influence of fibre orientation on computational models.

To achieve the described contributions, we have develop these tools:

- A new methodology to find the optimum threshold for scar segmentation on a set of images obtained with the same conditions.
- A methodology to adapt the scar segmentation procedure to post-contrast *ex vivo* CMR sequences.
- An application of the existing registration algorithms to RV endocardium.
- A new methodology to project volumetric scar onto the walls where the subendocardial thickness layer is not predefined.
- A new methodology to quantified the wavefront propagation velocity from activation time maps.

1.5 Structure of this thesis

This document is divided into two main parts. In Part I, the imaging and invasive tools are studied to get descriptions of the post-infarction substrate. It is composed by Chapters 2, 3 and 4. In Part II, the computational models are presented. Cardiac simulation are performed and validated based on experimental medical data processed in Part I. Chapters 5, 6 and 7 are included in Part II of the thesis. Finally, the main contributions and limitations of this thesis will be described in Chapter 8. We will now give a brief overview of each chapter.

Chapter 2 describes the experimental protocol followed to obtain the medical data that is employed on this work. A detailed description of the animal model of MI is provided. Specifications about the *in vivo* cardiac magnetic resonance protocol and electrophysiological study are presented.

Finally, the protocol to perform the *ex vivo* cardiac magnetic resonance from the explanted heart.

Chapter 3 explains how experimental data is post-processed. Here, the methodologies to solve the challenges of this thesis are provided: scar segmentation of *ex vivo* post-contrast CMR, RV surface registr$^{\circ}$ation or volume scar projection into the ventricle walls. The main objective of this chapter is to present the methodologies employed to describe the scar from experimental data and get the data in a common reference geometry, so that we can compare their substrate description.

Chapter 4 presents the main results obtained from the experimental data processing. On one hand, scar quantifications from data of different nature are exposed and compared. Thanks to the *ex vivo* CMR scar description, we present the limitations and propose interpretations of the *in vivo* data. On the other hand, it is studied if the volume of post-infarction scar described by CMR segmentations can be a possible marker for VT. At the end of the chapter, the main conclusions, contributions and limitations of this part of the study (Part I) are presented.

Chapter 5 introduces the mathematical models to simulate cardiac electrophysiology. A brief review of the existing models and a detailed mathematical description of the models employed are shown. The computational implementation of the models is also provided. At the end, Alya, the code used to solve the simulation is presented.

Chapter 6 describes how the simulation scenario is generated based on experimental medical data. First, the mesh generation is described. Then, fibre orientation is included and finally the pacing point is located. The wavefront velocity is computed from experimental activation maps during pacing. An synthetic model for fibre orientation is presented, for further comparisons between simulation including DTI fibre orientation and mathematical model orientation during Chapter 7.

Chapter 7 presents simulation results. A verification test is shown to assure the electrophysiological model was correctly implemented. Then, a sensitivity analysis for the diffusion parameter and the fibre distribution is presented. The results from a control case simulation are compared against experimental data. The main conclusions, contributions and limitation of Part II of the Thesis are described at the end of the chapter.

Chapter 8 summarizes the main contributions and limitations of the thesis. The lines that are proposed to follow as future work are also described in this chapter.

Part I

Post-infarction substrate characterization and clinical implications

Chapter 2

Experimental protocol and data acquisition

Myocardial infarction (MI) can be studied using imaging and invasive tools, which are particularly important for characterizing the infarct size and the tissue properties.

In this chapter, we will describe the experimental protocol followed for obtaining the experimental data from imaging tools like CMR and invasive EAM techniques. Details on the data processing will be given in Chapter 3, that will be followed by a description of the quantifications and conclusions of the study in Chapter 4. The main objective of the complete animal protocol was to study the characteristics and the limitations of each tool when describing post-infarct scar. A VT inducibility protocol was also included to study possible factors that could predict this type of arrhythmia.

The experimental protocol and data acquisition process will be described in a sequential order throughout this chapter. Starting with the pig model of myocardial infarction (Section 2.1). After a period of 10-12 weeks to ensure remodelling, animals underwent *in vivo* CMR (Section 2.2). The day after the CMR study, animals were subjected to the invasive electrophysiological study (Section 2.3). In the end of the electrophysiological study, animals were euthanized and the *ex vivo* CMR was performed (Section 2.4).

The experimental protocol was conducted in accordance with institutional guidelines and National (ECC/566/2015, RD53/2013) and European (2019/63/EU) regulation guidelines for the care and use of laboratory animals. All CMR studies and intervention procedures were performed under general anaesthesia. More details about all experimental protocol can be found in publications [31] and [49].

2.1 Animal model of myocardial infarction

Nineteen castrated male pigs (large-white strain, 35 kg) were part of this study. Sixteen animals underwent percutaneous catheterization of the left anterior descending coronary artery under general anaesthesia. The other three animals were included on the study as controls, they did not undergo any occlusion of coronary arteries.

Anaesthesia induction was achieved with intramuscular ketamine injection (15 mg/kg), xylazine (2 mg/kg) and midazolam (0.5 mg/kg) and maintained with continuous intravenous infusion of ketamine (2 mg/kg/h), xylazine (0.2 mg/kg/h) and midazolam (0.2 mg/kg/h). Animals were intubated and mechanically ventilated with oxygen (fraction of inspired O_2 of 21 %). Amiodarone (150 mg/h) was administrated during the procedure to reduce the risk of arrhythmias. Unfractionated heparin (300 mg/kg) was also administrated.

The infarct was generated by left anterior descending coronary artery occlusion by an angioplasty balloon placed and inflated during 60 minutes. The location of balloon was proximal or distal to the first diagonal branch, depending on the case (Figure 2.1). Balloon location and maintenance was monitored by angiography.

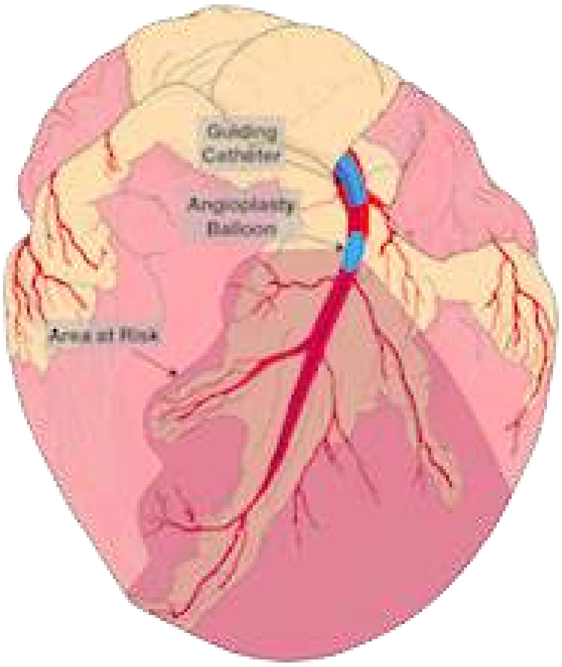

Figure 2.1: Animal model of MI. The left anterior descending infarct model scheme of the angioplasty balloon location respect during occlusion. Image from [31]

After the 60 minutes, the balloon was deflated and a coronary angiogram was recorded to confirm reperfusion. Five days later, all animals were transferred to specific animal research facilities for 10-12 weeks. Four animals suddenly died on this period.

2.2 Cardiac Magnetic Resonance (*in vivo*)

After 10-12 weeks the surviving animals underwent a cardiac resonance imaging, just 1-3 days before the invasive electrophysiology study. A Philips Achivea 3 T-Tx whole-body scanner (Philips Healthcare, Best, The Netherlands) was employed for the CMR procedure. Different sequences were obtained during the *in vivo* CMR, such as: Cine and contrast-enhanced sequences. All CMR data was exported as Digital Imaging and Communication in Medicine (DICOM) files.

Cine

Cine sequences provide a description of the cardiac function. It is a useful tool to quantify time changes of the myocardial thickening or ventricular volume during a beat, for example between systole and diastole. The ECG gating of cine sequences allows the acquisition of images at discrete states of the cardiac cycle, such as systole and diastole.

A ECG-gated cine steady-state free precision (SSFP) was performed to acquire 11-13 short axis slices covering the heart from base to apex, so that we can evaluate the LV motion. The acquisition parameters were: 280×280 mm as field of view; 6 mm of slice thickness without gap; repetition time 2.8 ms; echo time 1.4 ms, flip angle 45; cardiac phases 25; 3 NEX (number of excitations) and voxel size 1.8×1.8 mm [31].

Contrast-enhanced cardiac magnetic resonance

Contrast-enhanced cardiac magnetic resonance (CE-CMR) is a non-invasive technique widely accepted to characterize myocardial heterogeneous and dense scar. This classification is based on the fact that CE-CMR is able to differentiate areas with none, moderate and severe fibrosis using the signal intensity of the image.

The gadolinium contrast was injected 10 minutes before the CMR protocol. The CE-CMR sequences were acquired using an inversion-recovery spoiled turbo field echo with isotropic acquisition resolution of $1.5 \times 1.5 \times 1.5$ mm^3. Inversion acquisition was previously adjusted using look-locker scout with different inversion times to ensure healthy myocardium had null signal. All images were acquired under free breathing conditions and the acquisition time was reduced using parallel imaging in both phase encoding directions.

The rest of imaging parameter were: 2.41 ms for repetition time, 1.12 ms echo time and 10 degrees non-selective excitation angle. Finally, the reconstructed images had a resolution of $0.57 \times 0.75 \times 0.57$ mm^3.

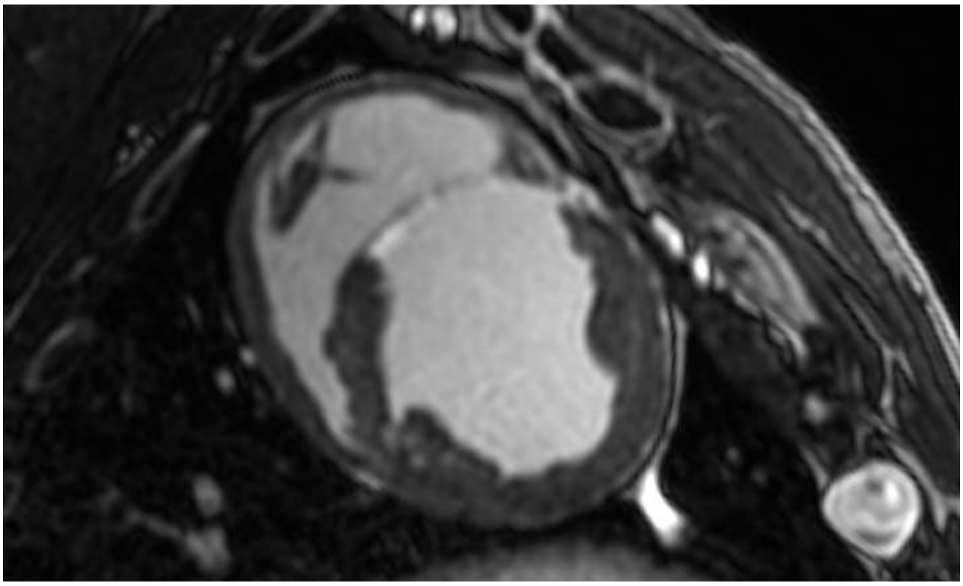

Figure 2.2: Cardiac magnetic resonance (*in vivo*). CE-CMR *in vivo* image of the short axis view including both ventricles.

2.3 Electrophysiological study

Between one and three days after the *in vivo* CMR acquisitions, the electrophysiological studies were performed. Cardiac EAM is an invasive tool widely used in the clinics for guiding ablation procedures.

Under general anaesthesia, the access to RV and LV cavities was achieved using percutaneous venous and arterial femoral, respectively. For epicardial access, a subxiphiod percutaneous approach was employed. A screw-in catheter was fixed in the right ventricle endocardium, for programmed ventricular stimulation. To record simultaneously atrial and ventricular electrograms, a 24-pole catheter was positioned in the epicardium. The hemodynamic changes were recorded by a 6-F pigtail catheter in the aorta. Electrical and blood pressure signals were continuously monitored using the LabSystem-Pro electrophysiology recording system (Boston Scientific).

First, electroanatomic mapping was performed to obtain basal voltage information on epicardic and endocardic walls. Then, a programmed ventricle stimulation was done to study the inducibility of VT or ventricular fibrillation (VF). On the control cases, the electrical activation maps were recorded during pacing.

2.3.1 Electroanatomic mapping

The electroanatomic mapping describes the geometry of ventricle cavities and local voltage information of measured locations on the walls. With the adequate density of information points, a voltage map can be built to find low conduction areas and locate conduction channels.

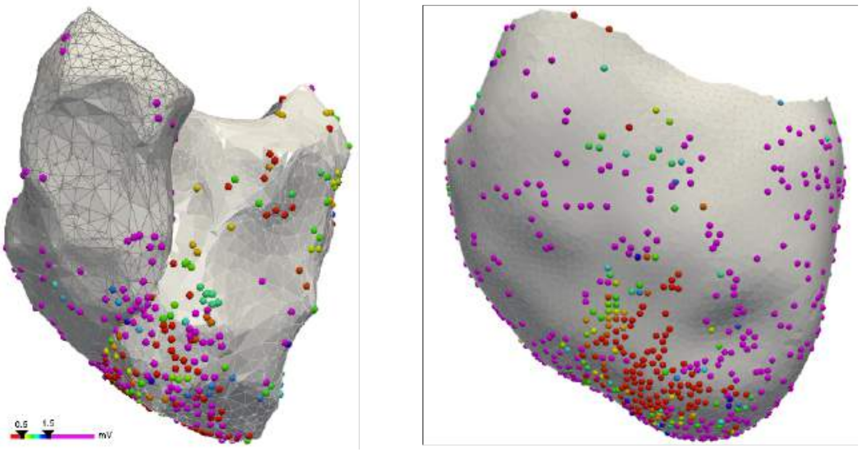

Figure 2.3: Electrophysiological study. Endocardial (LV, RV) and epicardial surfaces with voltage information points from electroanatomic mapping.

The geometry description of epicardium and endocardium (LV, RV) was generated by the fast anatomical mapping technology of the Carto3 electroanatomical mapping system (Biosense Webster). A 3.5-mm irrigated tip mapping catheter (Navistar Thermocool, Biosense Webster) was employed, a linear catheter standard for clinical procedures. We obtained both ventricle maps with a high density of local voltage information points, as the one shown on Figure 2.3. We could have increased the number of voltage points acquired by using multielectrode catheters for mapping instead the linear [95], usually employed in clinics, but it was not the aim of this study.

Table 2.1: Number of measurements locations on the electroanatomic voltage mapping.

	Geometry points	**Voltage points**
Voltage mapping:		
LV endocardium	**3043**	**1123**
	(2922, 3840)	(1064, 1172)
LV endocardium	**3220**	**370**
	(3018, 3574)	(324, 407)
Epicardium	**14951**	**1112**
	(14014, 16000)	(1059, 1218)

The number of points acquired for the geometry description and the voltage information points is shown by regions: epicardium and LV and RV endocardium. A detailed description of all cases mean and interquartile range can be found in Table 2.1.

Data from electroanatomic maps will provide a surface description of the ventricular geometry. It will define the surface area of the scar (Chapter 3).

2.3.2 Ventricular stimulation protocol

A programmed ventricular stimulation protocol was performed to induce ventricular arrhythmias. A screw-in catheter on the right ventricular chamber was employed for pacing.

The stimulation protocol consisted of five sequential basic drive cycle lengths (BDCL) for 10 beats (S1) at 350, 300, 280, 260 or 250 ms. For each BDCL up to four extrastimuli (S2, S3, S4, S5) were included, that is, up to four delivered premature stimulus at precise intervals decremented in 10 ms steps until refractoriness or 180 ms, the minimum coupling interval. All stimuli start on a fixed point of the RV endocadium.

2.3.3 Activation maps

The activation maps were performed during the electrophysiological study to record the activation times on points of the ventricles walls.

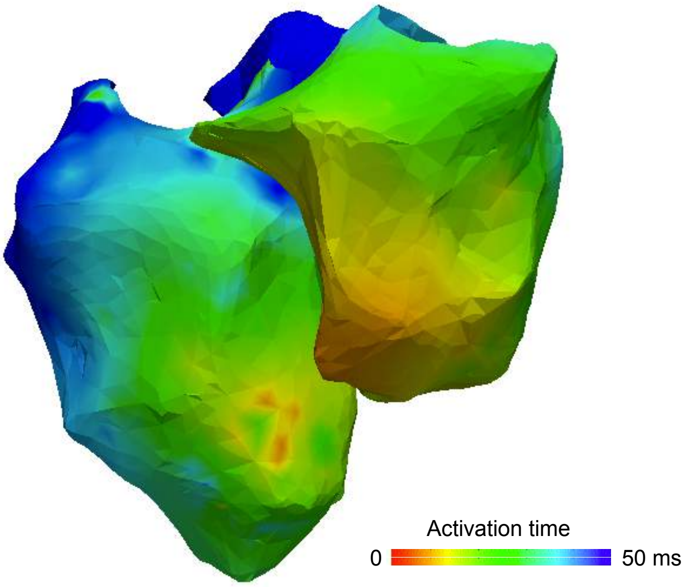

Figure 2.4: Electrophysiological study. Activation mapping of LV and RV endocardium during pacing of a control case.

The recording of electrograms, with a fixed reference, provides activation activation maps in the control cases during pacing on a fixed point of the endocardium (Figure 2.4).

Finally, a single intravenous bolus (0.2 mM/kg) of gadolinium-based contrast agent (Dotarem, Guerbet) was administered 10 minutes before euthanasia and heart excision. For further details refer to [31].

2.4 Cardiac Magnetic Resonance (*ex vivo*)

Cardiac magnetic resonance on *ex vivo* data is an experimental technique able to improve the accuracy of the images, in comparison to *in vivo* CMR. This mostly occurs because there is no movement artefacts and the acquisition times can be longer. Two types of sequences were acquired during the CMR procedure: post-contrast sequence that will describe the scar structures, thanks to the contrasts injected before excision of the heart; and DTI sequences that will describe the fibre orientation.

The magnetic resonance DTI is a non-invasive technique able to describe the cardiac fibre organization based on the properties of water diffusion. *In vivo* DTI imaging remains inaccurate due to motion and technical difficulties. In the contrary, *ex vivo* DTI has great reproducibility [82, 62]. In this study, DTI sequences were only acquired on the *ex vivo* CMR.

2.4.1 Explanted heart preparation

Immediately after euthanasia, the hearts were explanted and prepared for *ex vivo* CMR studies in order to ensure that the tame contrast perfusion on the heart was the same as the *in vivo* CMR protocol. To ensure *in vivo* and *ex vivo* CMR images had similar geometries, volume preservation of the *ex vivo* anatomy was key. It is also important to avoid ventricle walls to collapse since that would affect the fibre orientations and scar reconstructions.

To avoid the mentioned problems, the heart was filled with a 2% warm agarose gel solution (∼ 38° Celsius). First, an atrial transseptal puncture was performed. Second, all vein orifices were closed with surgical threads to avoid volume leaks during heart filling. The heart was filled until the ventricular cavities resembled an *in vivo* heart during diastole (Figure 2.5).

A custom-designed watertight container made of plastic and magnetic resonance compatible was employed while in the CMR procedure. Once the container was filled with a bed of 2% agarose gel, the filled heart was introduced. Finally, additional 2% agarose solution was added until hearts were fully embedded. Agarose gel was fully consistent after a cooling-down time of 20 minutes at room temperature [31].

Figure 2.5: Cardiac Magnetic Resonance (*ex vivo*). Explanted heart filled and the container Magnetic Resonance compatible . Figure from [31].

2.4.2 CMR *ex vivo* sequences

The container was introduced in the magnetic resonance antennae and the *ex vivo* CMR sequences were acquired. The CMR data were exported as DICOM files and processed offline.

R1 sequence

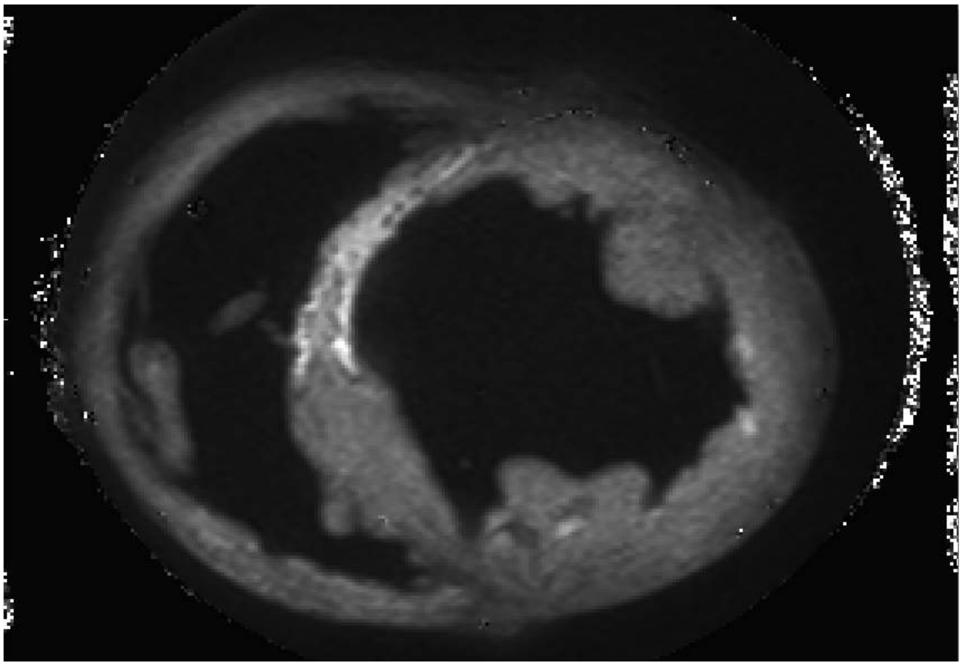

Figure 2.6: Cardiac Magnetic Resonance (*ex vivo*). R1 sequence with short axis view.

Post-contrast CMR sequences (T1 mapping) were acquired using a Look-Locker inversion recovery-turbo field echo sequence: TR=5.9 ms, TE=2.8 ms and flip angle of 7°. Inversion pulses were applied every 6 s, a total of 36 inversion times in 147 ms steps.The acquisition resolution was isotropic, $0.6 \times 0.6 \times 0.6$ mm^3.

The R1 images were calculated from the 36-inversion times of the T1 images with a customized software (IDL 8.1, Berkshire, UK) as published on [53]. The R1 reconstructed images had a final voxel isotropic resolution of 0.451389 mm^3. An example of R1 image is shown on Figure 2.6.

Diffusion Tensor Imaging (DTI)

Two dimensional DTI was acquired with a single-shot spin echo-EPI. The acquisition resolution was isotropic 1.1 mm^3. The reference image (b=0 s/mm^2) and 15 different diffusion directions (b=600 s/mm^2) were applied (Figure 2.7). Further details in [31].

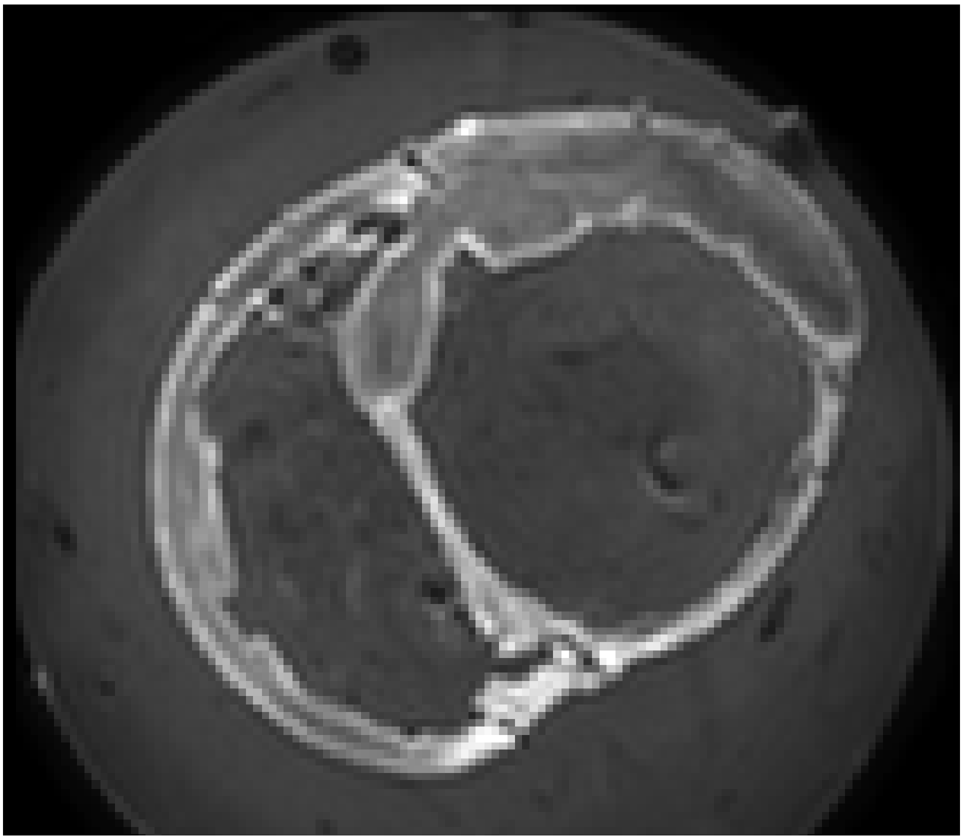

Figure 2.7: Cardiac Magnetic Resonance (*ex vivo*). Slice of DTI in the axial from a post-infarct case.

Chapter 3

Data processing

Data obtained during the experimental procedure (Chapter **??**) has to be processed so that the cardiac function and structure can be analysed. In this chapter, different processing techniques will be presented and applied depending on the nature of the experimental data and the comparisons between techniques that will be analysed in Chapter 4.

The post-infarction substrate will be defined from electroanatomic maps by voltage thresholding (Section 3.1) and from post-contrast *in vivo* and *ex vivo* CMR sequences through segmentation (Section 3.2). We will obtain a surface scar description on the ventricle walls from EAM and a volume scar description from post-contrast CMR, *in vivo* and *ex vivo*. In addition, the three techniques have different level of accuracy that can affect to the scar descriptions.

The study of scar characterization differences between *in vivo* techniques (EAM and contrast enhanced CMR) compared with *ex vivo* post-contrast CMR is not straight forward. Extra data processing will be needed. The integration of surface voltage data from electroanatomical mapping and volume data from CMR scar segmentation (Section 3.3). Myocardial fibre orientation description will be obtained from *ex vivo* DTI sequences in Section 3.4.

The methodologies described on this chapter were presented in [49, 31].

3.1 Electrophysiological data processing

The experimental electrophysiological study was performed as described in Section 2.3. Now, we will describe the post-process of these electrophysiological data. We will present how the voltage maps were built and how the dense and heterogeneous scar were described by voltage thresholds.

3.1.1 Scar definition on electroanatomical maps

During the EAM procedure, epicardial and endocardial ventricle walls geometries were obtained as surface meshes. The local basal voltage of the electrical impulses was measured on several points of the surface.

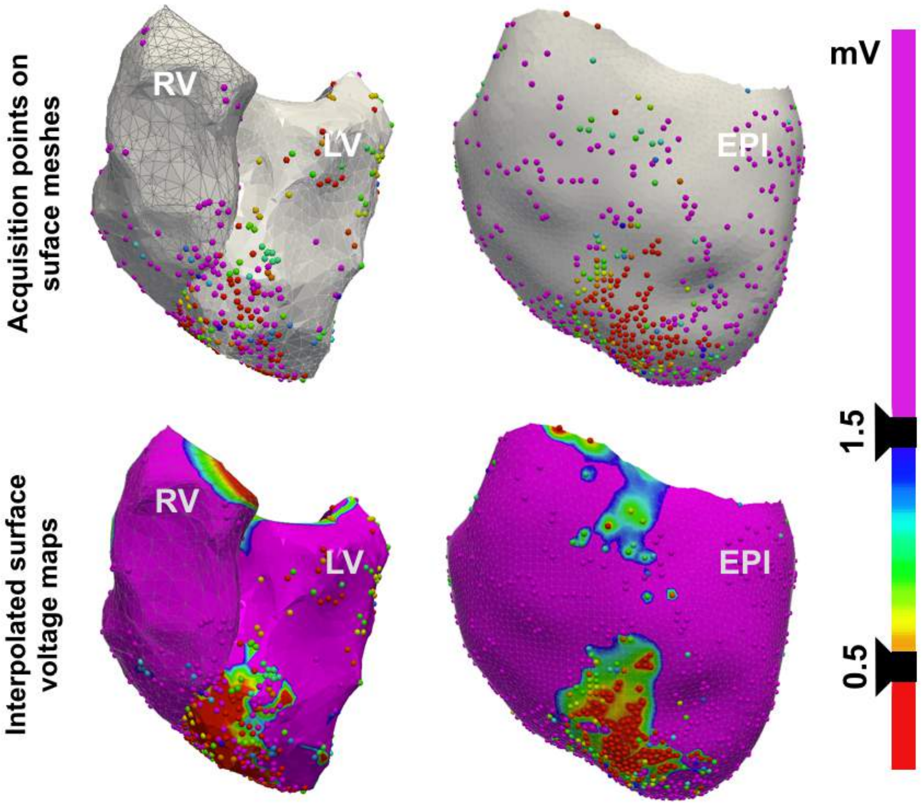

Figure 3.1: Electrophisiological data processing. On the top, acquired bipolar electrograms projected on the surface meshes (LV , RV and EPI). On the bottom the voltage information interpolated among the surface nodes (LV, RV and EPI). The same colour-voltage scale was applied to points and surface meshes.

Acquired bipolar electrograms were projected onto the electroanatomic surface meshes using a minimum distance-based algorithm (Figure 3.1, top). But, the electrical information must be interpolated to all mesh nodes. The most popular interpolation tool is the one given by CARTO®3 mapping system (Biosense Inc.). It was employed during the experimental procedure, but an improvement of the interpolation was done in the offline data processing to obtain a more accurate voltage definition of the scar.

An inverse distance weighted algorithm was employed to interpolate voltage-information among the nodes of the surface mesh [48]. It is based on a weighted linear combination of the neighbouring nodes voltage information.

As a result, we obtained a whole-heart description of the voltage in basal rhythm (Figure 3.1, bottom). For all cases, the voltage maps were saved as surface meshes with nodal information of voltages for further analysis.

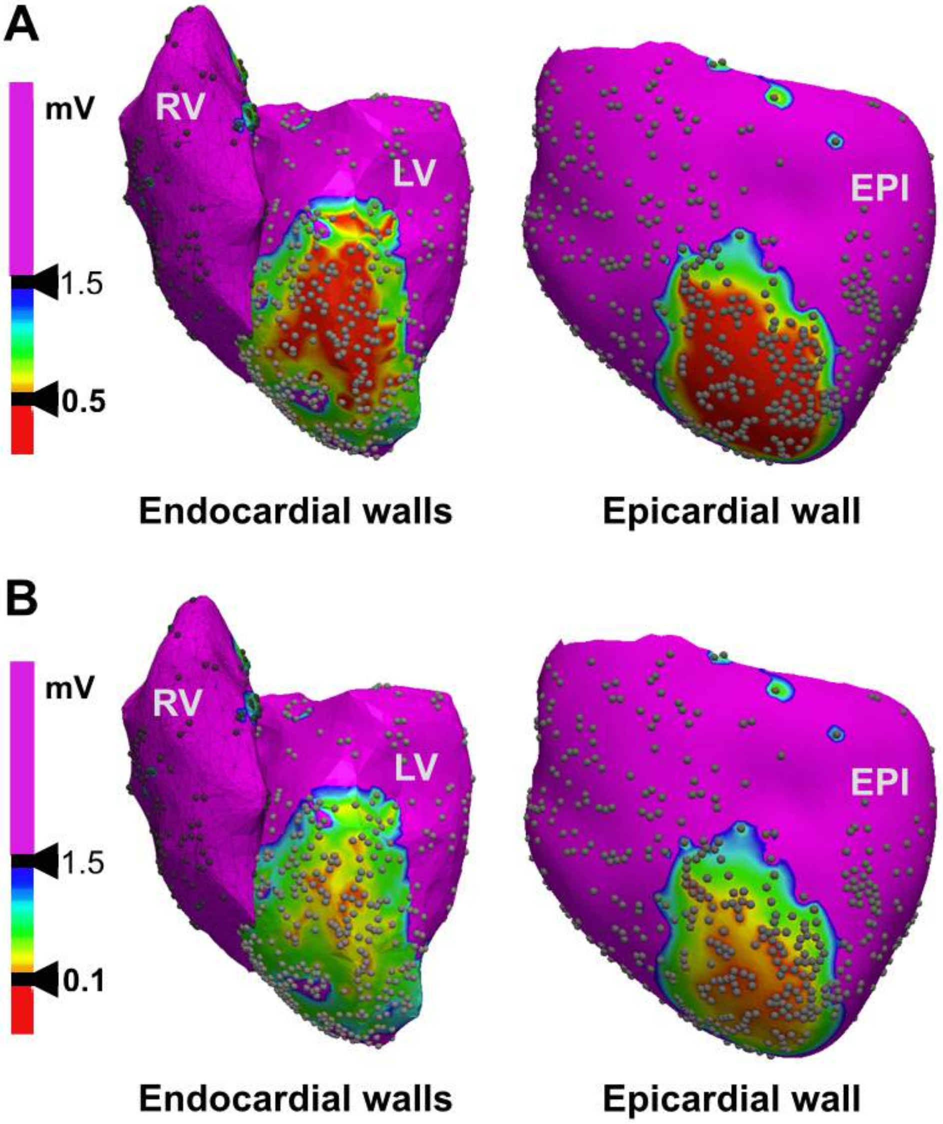

Figure 3.2: Electrophysiological data processing. Scar definition on surfaces from EAM. Low voltage criteria of ≤ 1.5 mV and ≤ 0.5mV (A) or ≤ 0.1 mV (B).

Scar definition by voltage criteria. The scar on the electroanatomic maps was defined using voltage thresholds criteria. A linear interpolation method was employed to define pathological and healthy regions based on conventional bipolar thresholds [76]. The low voltage criteria under 1.5 mV defined the scar tissue and split it from healthy tissue (Figure 3.2).

The scar region is not homogeneous, the dense and heterogeneous scar can be defined also by voltage thresholds. But, there is not an agreement about which is the adequate threshold to classify the scar into the two types. Some authors have proposed that dense scar is defined by voltage values lower than 0.5 mV [76]. In the other hand, other authors consider that 0.1 mV is the adequate threshold to differentiate dense on voltage maps obtained mapping with standard linear catheters [95].

Changing the threshold criteria for dense scar can give huge changes that will affect to the scar dense and heterogeneous characterization (Figure 3.2). For the moment, we will not establish a correct threshold. We a detailed analysis will be performed in Chapter 4.

3.2 Segmentation of post-contrast CMR

The post-contrast CMR sequences can describe the structural changes of hearts after MI. Segmentation is the first and fundamental step to extract information from *in vivo* T1 and *ex vivo* R1 sequences. The R1 images were calculated from the 36-inversion times of T1 *ex vivo* sequences as explained in Chapter 2.

Through segmentation, pathological and healthy tissue will be defined on CMR sequences. Tissue characterization will be done in three steps: first an accurate segmentation of both ventricles, second a scar segmentation on the previous defined ventricles and finally the scar classification into dense and heterogeneous scar. For controls, only the first step was necessary.

Manual refinement of ventricle segmentations and automatic scar segmentation were performed using the software Amira (Amira 6.0.1, Thermo Scientific^{TM}).

3.2.1 Ventricle segmentation

The ventricle segmentation was done following the same methodology on R1 *ex vivo* sequences and T1 *in vivo* sequences.

An initial automatic segmentation based on voxel intensity value thresholding of the images to defined both ventricles geometry was applied, followed by an island filter to eliminate isolated volumes. The result was a very coarse segmentation (Figure 3.3). Threshold-based segmentation is a simple automatic method that is not able to differentiate the fat attached to the epicardical walls or get a good definition of endocardical wall irregularities, i. e. papillary muscles. An accurate definition of both ventricles was obtained by a detailed and time-consuming manual segmentation supervised by a medical expert (Figure 3.3).

In literature, other methods that improve the automatic segmentation can be found [51, 69], but the gold standard remains manual segmentation.

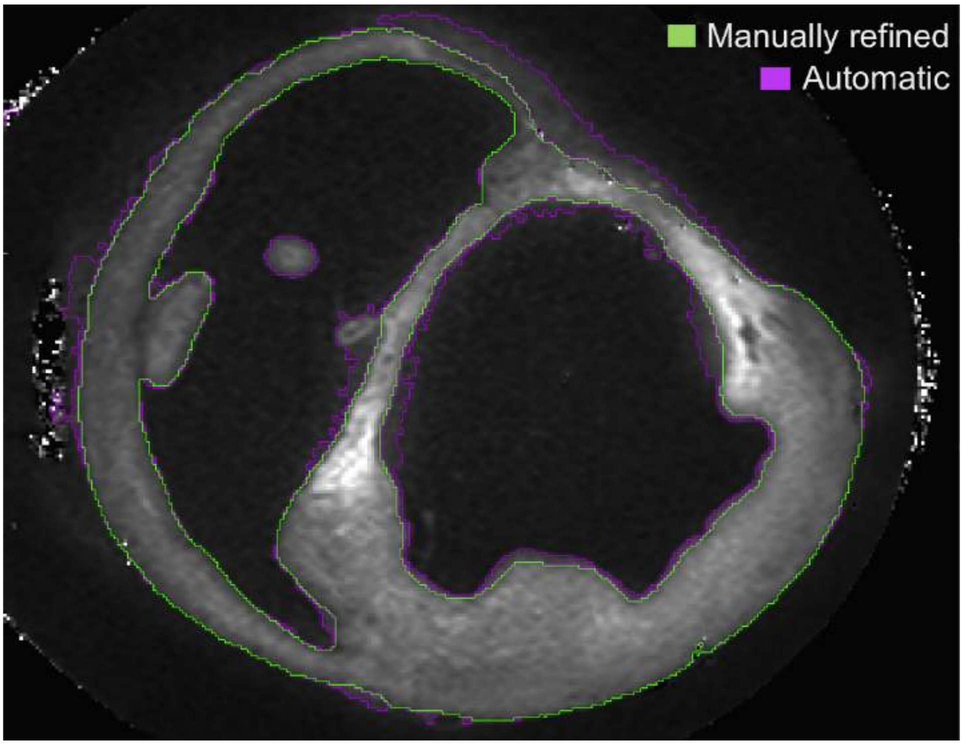

Figure 3.3: Segmentation of post-contrast CMR. Both ventricles R1 *ex vivo* segmentations by automatic method (threshold-based) and after a manual refinement.

Volume preservation on *in vivo* and *ex vivo* CMR The volume of the ventricle segmented form *in vivo* CMR was 173.9 cm^3 in median with a interquartile range (IQR) of 153.6-184.0 cm^3 and 201.3 cm^3 with IQR 191.9-224.2 cm^3 in the case of segmentation from *ex vivo* CMR.

The preservation of the LV cavity volumes between *in vivo* and *ex vivo* CMR was presented in [31]. The median cavity volumes were almost identical in both cases. This assures that the experimental procedure performed on the explanted hearts to avoid the wall collapse during the *ex vivo* CMR procedure, explained in Chapter 2, was correct.

3.2.2 Scar segmentation

The characterization of the post-infarct substrate was done through an automatic scar segmentation on the *in vivo* T1 and *ex vivo* sequences. The automatic differentiation between healthy and pathological tissue was based on previous ventricle segmentations.

In the literature, a large number of methods can be found for scar segmentation of T1 delayed contrast enhancement sequences from *in vivo* data [40], but there is not a standard technique. The Task Force for Post Processing of the Society for Cardiovascular Magnetic Resonance (SCMR) has published recommendations to narrow the large amount of methods proposed for scar segmentation on T1 *in vivo* delayed contrast enhancement data [81]. Two semi-automatic methods based on thresholds are recommended:

- "n"-SD technique: based on standard deviations of the intensity value on healthy tissue [42, 78, 106].
- Full-width at half-maximum (FWHM) method: based on threshold by half of the maximum voxel intensity value on ventricles [4, 28, 90].

The Task Force [81] and other authors [4, 28, 90] found that the FWHM method was the most reproducible, comparing to methods based on standard deviation or manual segmentation. But it was also stated that FWHM has some limitations in terms of scar delineation accuracy, mostly on isolated scars where it assumes a core enhancement and extrude artefacts.

Modifications of the FWHM method have been suggested. Those studies proposed to select percentages that do not coincide with the half-maximum (50%). Nowadays, there is not an agreement for what is the optimum value yet. Soto-Iglesias et al. propose 40% of the maximum intensity value [84] or Wijnmaalen et al., 35% [103]. In view of the different threshold values found on literature, we propose to evaluate a range of thresholds for scar segmentation of T1 *in vivo* images and, after quantification, find the optimum one.

Looking at the state of the art on scar segmentation of T1 *ex vivo* sequences, some punctual studies can be found [42]. But, there is not a clear preference method for scar segmentation on R1 *ex vivo*. We propose to adapt the *in vivo* scar segmentation methodology to R1 *ex vivo*. However, an extra step will be introduced to R1 *ex vivo* segmentation due to the big amount of artefacts that appear.

The scar segmentation was done with a new methodology based on FWHM. The modifications proposed aim to increase the accuracy of thresholded segmentations for *in vivo* data and adapt the method to *ex vivo* R1 images.

3.2.2.1 Scar segmentation: *Ex vivo* CMR

Taking into account the FWHM method and the published for *in vivo* data, propose to adapt the methodology to R1 *ex vivo* sequences. We evaluated the percentages of maximum signal intensity values within the range of 40-80% with 1% step increase. After a de-noise procedure based on the ventricles thickness, we quantified the remaining artefacts and the scar on a pre-defined region of interest (ROI) and find which was the optimum threshold.

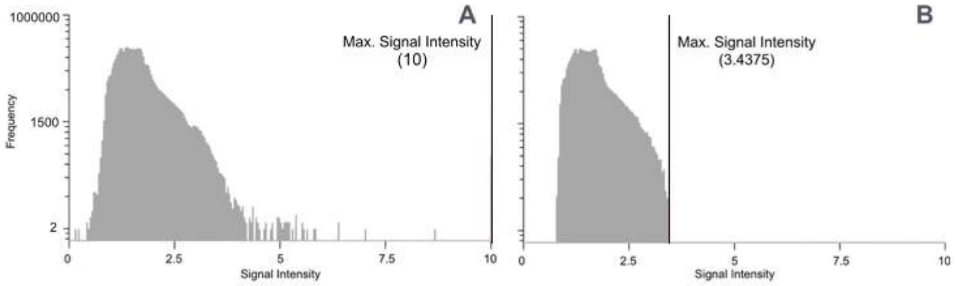

Figure 3.4: Segmentation of post-contrast CMR. Signal intensity histograms of a sample segmented ventricles case: (A) R1 histogram, (B) R1-filtered by a median filter histogram.

First of all, we had to find the maximum intensity value of the ventricles that posteriorly defined the threshold for scar segmentation, as in the FWHM method. For each case, a signal intensity histogram of the R1 image on the segmented ventricle was computed but, due to the noise, it was not clear the maximum intensity value (Figure 3.4 A). A median filter of 26 neighbours was applied for image de-noising. The signal intensity histogram was re-computed, this time with the filtered image. Then, the maximum value of intensity was localised easily, artefacts had disappeared (Figure 3.4 B).

Furthermore, the maximum value of intensity taken on the segmented ventricle must correspond to scar tissue. To assure this, a ROI around the scar was manually defined. The maximal signal intensity of the ROI must be higher than the one from the rest of the heart, where we differentiated a basal region around the aorta. For each of these regions, signal intensity histograms were computed and compared (Figure 3.5).

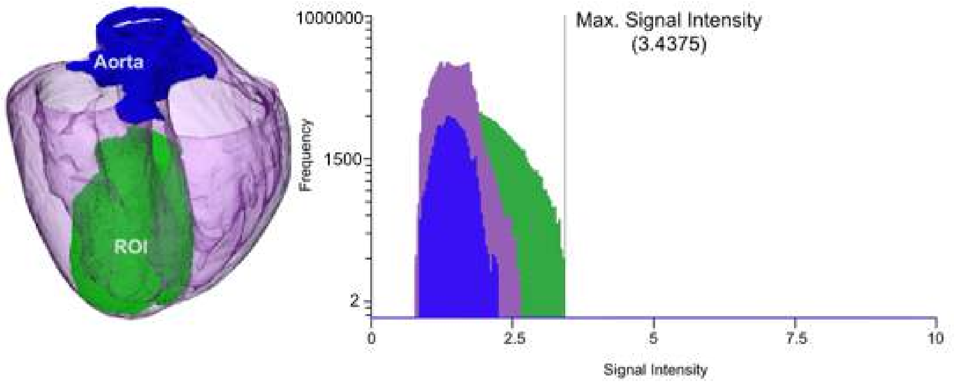

Figure 3.5: Segmentation of post-contrast CMR. In the left, ventricle reconstruction including the definitions of scar ROI (green, basal tissue around aorta (blue) and the rest of healthy myocardium (purple). In the right, signal intensity histograms overlapped: ROI, basal area and healthy tissue (same colour code).

In all cases, the maximum intensity values corresponded to the scar ROI volume and were denoted as x_{max}. For each x_{max} a range for thresholds for segmentation were defined as:

$$thr_p = x_{max} * \frac{p}{100} \tag{3.1}$$

where p is an integer number between 40 and 80 that vary to compute a different scar segmentations of the same image. For $p = 50$, it is equivalent to the FWHM.

The scar segmentations were performed applying thr_p thresholds that correspond to percentages $40 \leq p \leq 80\%$ on filtered R1 images (median filter for 6 neighbours). Isolated artefacts smaller than 15 voxels connected were eliminated; that is, if they had a volume smaller that 1.37 mm^3.

Notice that the scar segmentation procedure for *ex vivo* R1 sequences and *in vivo* T1 sequences was the same until this step. For *ex vivo* heterogeneous scar segmentation, thresholding was not enough to obtain accurate scar segmentation. False positives were detected on all segmentations of the range 40-80%. So, based on the fact that infarction provokes a thinning of the ventricle wall, we imposed that no segmented scar can be on ventricle volume with a local wall thickness is bigger that the median ventricle thickness. To finish the de-noising the basal segmented scar was manually eliminated.

The local thickness was computed using distance maps based on the ventricle segmentation mask. On each *ex vivo* case, the LV and RV endocardial cavities were segmented, as well as the epicardial areas out of the heart (Figure 3.6).

Distance map image was computed as the distance to each defined boundary. The distance zero always corresponded to the boundary itself and the rest of the voxels value give the distance to the boundary selected. A sample example of each distance map image is given in Figure 3.6.

Four distance maps were computed:

- d_{LV}: Distance to the LV endocardium
- d_{RV}: Distance to the RV endocardium
- d_{EpiLV}: Minimum distance to the epicardium or LV
- d_{EpiRV}: Minimum distance to the epicardium or RV

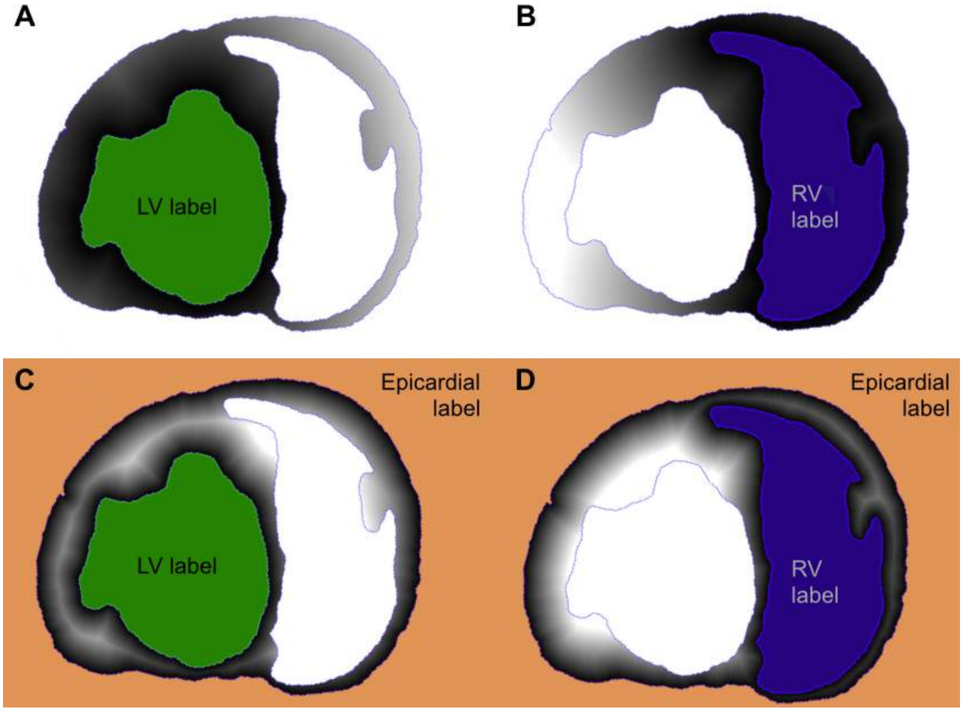

Figure 3.6: Segmentation of post-contrast CMR. Distance maps (A: d_{LV}, B: d_{RV}, C: d_{EpiLV},D: d_{EpiRV}) computed from the segmented cavities: LV cavity in green, RV cavity in blue and epicardial cavity outside the heart in orange.

The local thickness (h_{local}) was defined by the addition of voxel information of epicardic distance map and endocardic distance maps:

$$h_{local} = \begin{cases} d_{EpiRV} + d_{LV} & \text{on LV voxels} \\ d_{EpiLV} + d_{RV} & \text{on RV voxels} \end{cases}$$

The septum was also computed to calculate the wall thickness of ventricles.

A manual differentiation of right and left myocardium was made, including septum on the left myocardium (Figure 3.7 A). The median of myocardium local thickness was calculated for each case from the segmented ventricle of the h_{local} map. Voxels of h_{local} map with a value lower than that median defined a mask (Figure 3.7 B). All the segmented scar located outside the mask was eliminated, since remodelling due to infarction generally causes a thinning of the wall.

Finally, the scar locate in the base of the heart was manually erased due to the fact that none of infarcts were expected to occur on the base. The final step also only for *ex vivo* scar segmentation is to avoid artefacts that are not describing scar.

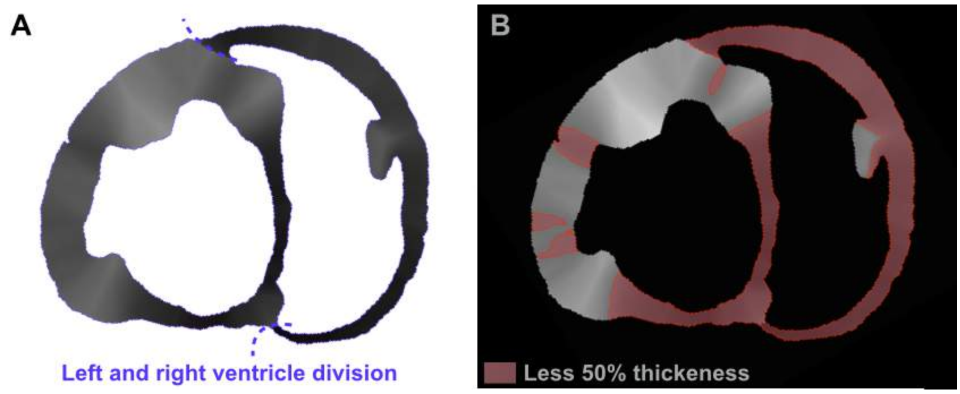

Figure 3.7: Segmentation of post-contrast CMR. A: Local thickens image including LV-RV division for septum computations. B: Local thickness image with less than 50% mask overlapped.

Quantifications. The improvement of the scar segmentation method for R1 *ex vivo* data once applied the thickness criteria has to be quantified. Also quantifications are needed to find an optimal threshold of the proposed range for scar segmentation in *ex vivo* data.

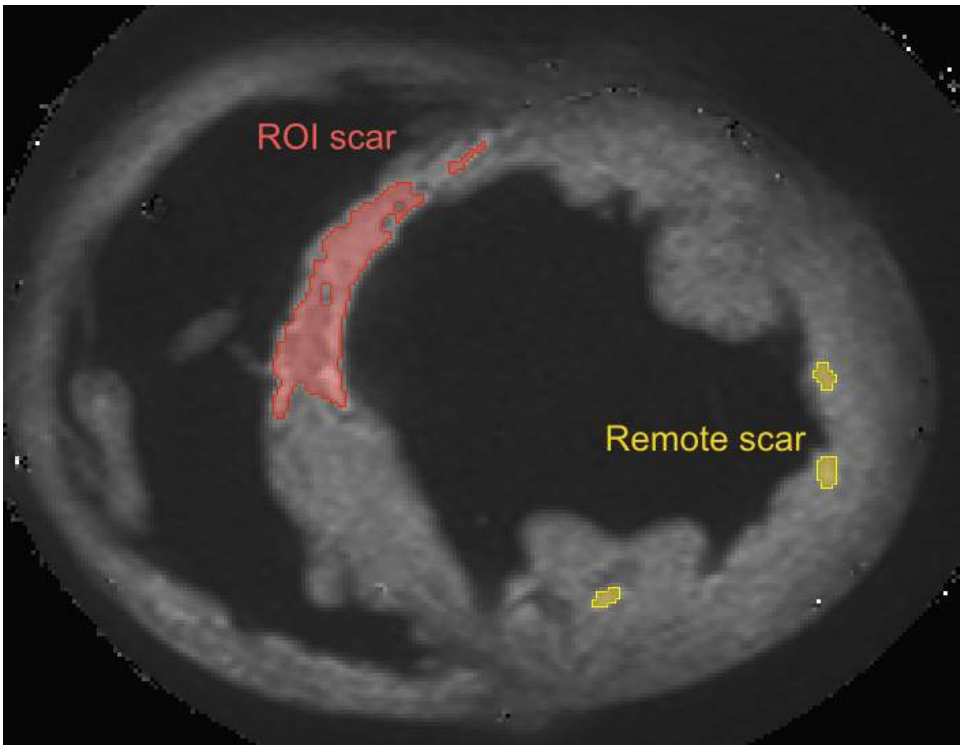

Figure 3.8: Segmentation of post-contrast CMR. Post-contrast *ex vivo* R1 including scar segmentation. The scar was classified into: ROI scar (red) and Remote scar (yellow).

Both examples required the quantification of artefacts and false positives. The best scar segmentation was defined as the one that after all the described steps has the optimum equilibrium between minimum false positives and maximum accuracy for capturing the scar. It is difficult to select by eye the best threshold, so to evaluate this equilibrium, we have quantified it.

For quantification purposes, the segmented scar was distinguished into two: scar on the ROI, previously defined to find the maximum signal intensity value; and remote scar, outside of that ROI (Figure 3.8). On each case, all the scar areas by slice were added and normalized to the sum of the full ventricle area, distinguishing also here between remote and ROI scar. Based on these scar by slice areas measurements on *ex vivo* data, we can:

- Quantify the impact of thickness criteria to eliminate false positives.
- Find the optimal thresholds for heterogeneous and dense scar segmentation of R1 data.

This scar quantification method was also employed to quantify *in vivo* segmentations.

The *ex vivo* R1 scar segmentation methods were quantified and compared.

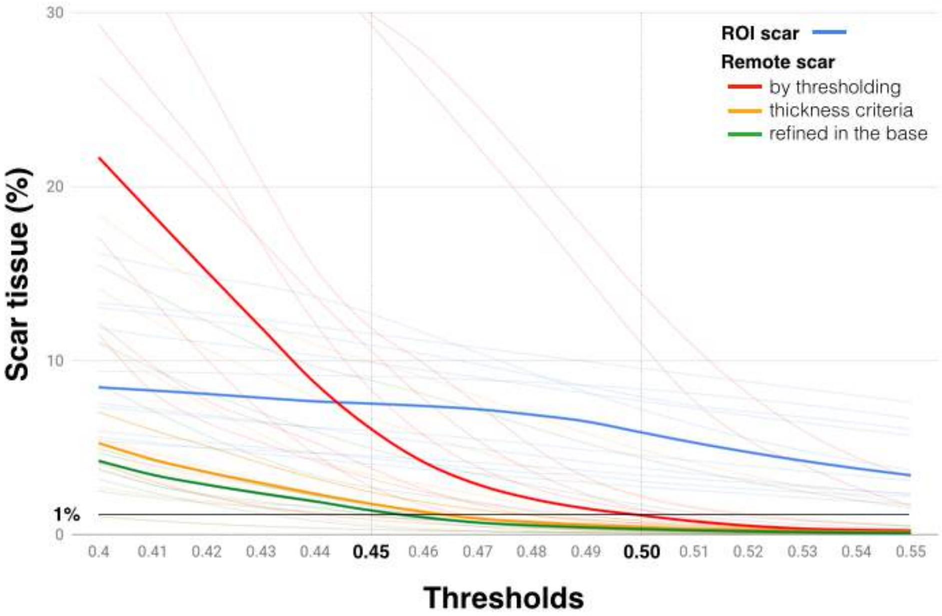

Figure 3.9: Segmentation of post-contrast CMR. Comparison between scar thresholding by threshold without refinement (red), with a thickness criteria refinement (yellow) and with both thickness criteria an manual elimination of basal scar (green). In blue is represented the ROI scar obtained by threholding without refinement. Curves in bold represent the mean of 10 cases plotted in light lines.

In Figure 3.9, we can see that the slope of remote scar radically decrease applying the thickness criteria. And the basal scar elimination also helps to get lower values of remote scar without augmenting the percentage defining the scar segmentation threshold. This means that reduce the false positive voxels in scar segmentations.

We can state that, for *ex vivo* scar segmentations, the threshold segmentation combined with thickness criteria, that eliminates artefacts and increases the accuracy without adding false positives. It is useful to perform scar segmentation in *ex vivo* data, a type of images where few methods has been proposed and none of them is considered a gold standard.

The optimum threshold for *ex vivo* scar segmentations was found based on remote and ROI scar quantifications after the de-noising procedures.

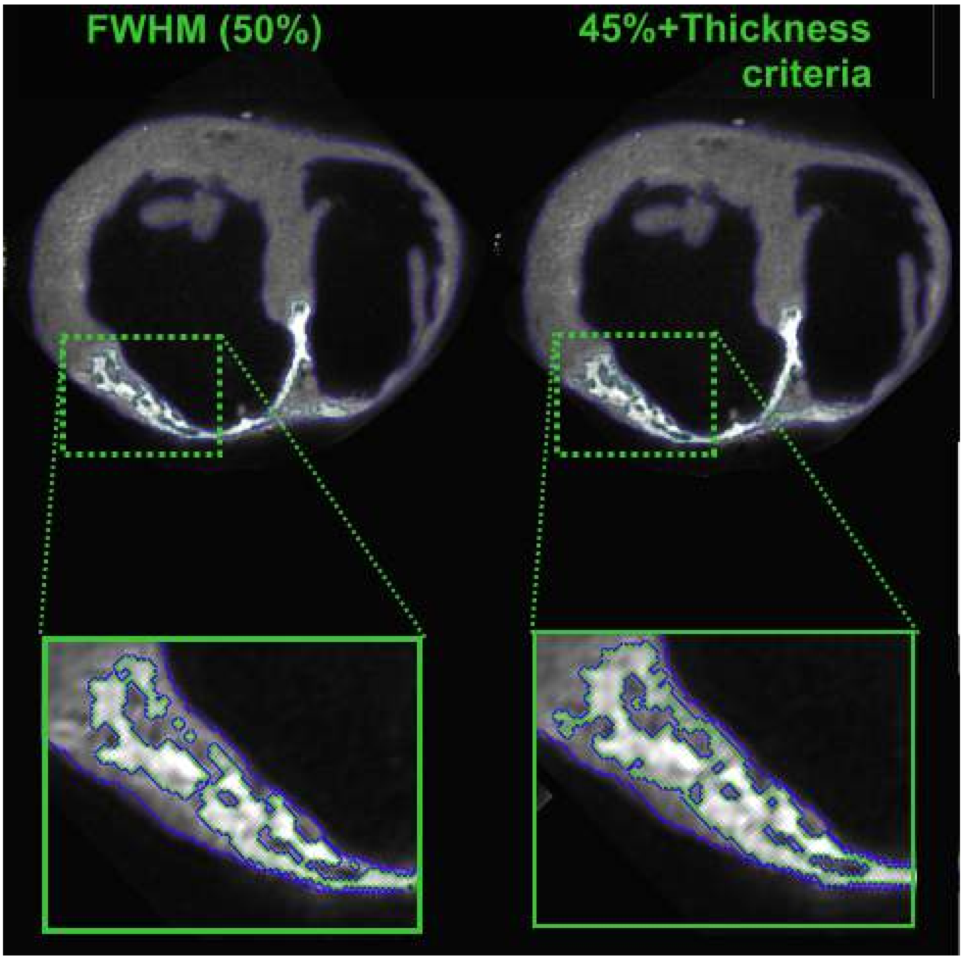

Figure 3.10: Segmentation of post-contrast CMR. Segmentation on *ex vivo* R1 by FWHM and 45% threshold after thickness criteria

As shown on Figure 3.9, for thresholds higher that 47% the ROI scar curve (in blue) starts decreasing, thus lowering the accuracy of scar segmentation. Moreover for thresholds lower than 47% the level of noise clearly decreases, that is remote scar curve (in green) has a negative slope. So, segmentations corresponding to 45-47% were selected as the ones with the best scar on ROI and the lower amount of remote scar to be analysed by an expert, therefore the 45% was selected as the optimum threshold.

It is interesting to remark that for *ex vivo* segmentation by 50% threshold without extra de-noising, FWHM, the remote scar value (red curve, Figure 3.9) was 1.12% of the total ventricle. This value was between to 1.40% and 1.01%, that corresponded to 0.45 and 0.46 thresholds once applied our proposed method applied (in green curve, Figure 3.9). This means that we have a similar amount of remote scar using the FWHM or 45% threshold with the proposed thickness criteria. However, choosing the 45% after thickness criteria improves the accuracy on the ROI without adding false positive voxels, comparing to the FWHM method (Figure 3.10).

We have proposed a scar segmentation method adequate for R1 *ex vivo* sequences based on signal intensity threshold combined with a thickness criteria for de-noising. Also, we have proposed a tool for scar quantification useful to find the adequate percentage threshold for a set of images taken with the same conditions and protocol. In addition, for our set of images the threshold to characterized scar tissue was 45%, after thickness criteria. The final segmentation showed a median of <1% of remote heterogeneous scar, which is compatible with fibrotic remodelling in remote areas.

3.2.2.2 Scar segmentation: *In vivo* CMR

When we introduced the scar segmentation at beginning this Section 3.2.2, we saw that there were a large amount of works published on this field [4, 28, 90, 84, 103, 106], especially comparing few references to scar segmentation of *ex vivo* data in literature. Most of the works were based on the FWHM method, or modifications of it.

We propose to perform automatical scar segmentation of *in vivo* T1 images by signal intensity thresholds. This thresholds will depend on the maximum intensity value, the same that occurs for FWHM method. The difference will be that we will evaluate a range of thresholds, quantify the resulting segmentations and select the optimum one for our set of images, as we have done for *ex vivo* data.

The steps followed for scar segmentation of *in vivo* T1 were the same as the ones presented scar segmentation on *ex vivo* R1 sequences, but without segmentation refinements:

1. Maximum intensity value on segmented ventricle was found. This value must coincide with the maximum value on the ROI to be defined as

the **maximum signal intensity value** of a particular case, x_{max}.

2. Automatic scar segmentation by thresholds defined following the equation:

$$thr_p = x_{max} * \frac{p}{100}$$

where p is an integer between 40 an 70. For each case all the segmentations corresponding to the range of values $p = 40 - 70$ were performed on the T1 sequences filtered.

3. Isolated artefacts smaller that 15 voxels connected were eliminated.

No more de-noising procedures were applied to evaluate the optimum threshold on similar condition as the recommended by the Task force [81].

The optimum threshold for *in vivo* scar segmentations was found based on scar quantifications. The segmented scar was classified into remote and ROI scar and quantified by the computation of the normalized slice areas of both scars defined, as it was done before for *ex vivo* scar quantifications.

The resulting quantifications can be shown on Figure 3.11. Where we can appreciate that the ROI scar curve has a approximately constant slope in all threshold values. If we compare the *in vivo* and *ex vivo* ROI scar area, we find the scar area differences are smaller between 45-49%, with a 1.5% of variation.

On the same figure, we can observe that the percentage of remote scar was smaller than a one per cent for all segmentations done at 45-49% thresholds. Segmentations corresponding to that range of threshold were evaluated by and expert that established 45% as the optimum threhold for scar segmentation of our T1 sequences.

The method for scar segmentation employed was similar to the ones found on the literature based on FWHM method. In this field, we have proposed that there is not a general optimum percentage for scar segmentation of *in vivo* CE-CMR. We recommend to quantify the scar given by a range on thresholds, an establish the optimum segmentation thresholds for a particular set of images taken on similar condition and using the same protocol. This idea comes from the fact that different resonance machines, times of acquisition, the quantity of gladolinium contrast used, etc. can vary the images. We think that the percentage between healthy tissue and the maximum intensity pixel of scar tissue is not always a fixed percentage. It is true that difference is needed, this quantification can help to get more accurate scar segmentations.

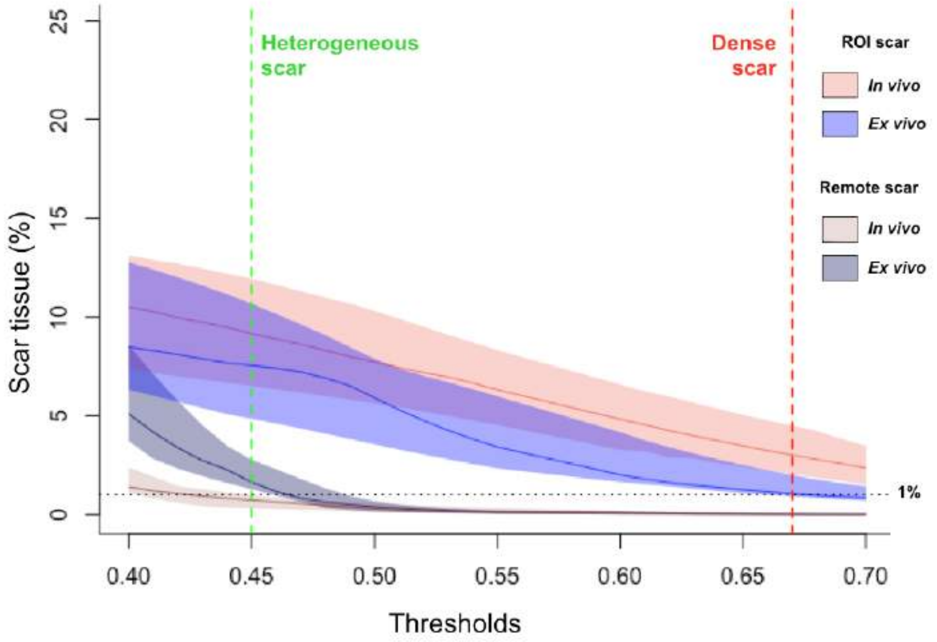

Figure 3.11: Segmentation of post-contrast CMR. Quantifications of ROI and remote scar from *ex vivo* (after de-noising) and *in vivo*, changing with the threshold chosen [49].

To conclude, it is important to remark that 45% was found the optimum percentage chosen to segment the complete scar on both sets of images from *ex vivo* and *in vivo* data, despite performing independent analysis of the data (Figure 3.12).

3.2.3 Dense scar characterization

Once established the optimum threshold for complete scar segmentation, the healthy tissue and the scar are well defined. It is time to differentiate between dense and heterogeneous scar, to do so we have to find a threshold value able to distinguish them.

The FWHM method is not able to differentiate the two types of scar, but in the literature we can find some studies that propose pairs of thresholds, the first one to distinguish healthy and pathological tissue and another one to distinguish dense and heterogeneous scar. Soto-Iglesias et al. propose 60% for dense scar and 40% for total scar [84], Wijnmaalen et al. 50% and 35% [103], or Tanaka et al. 80% and 50% [90], equivalent to FWHM for total scar segmentation. Those pairs of thresholds are related approximately by threshold for heterogeneous scar is around 2/3 of the dense scar threshold, as proposed in [5].

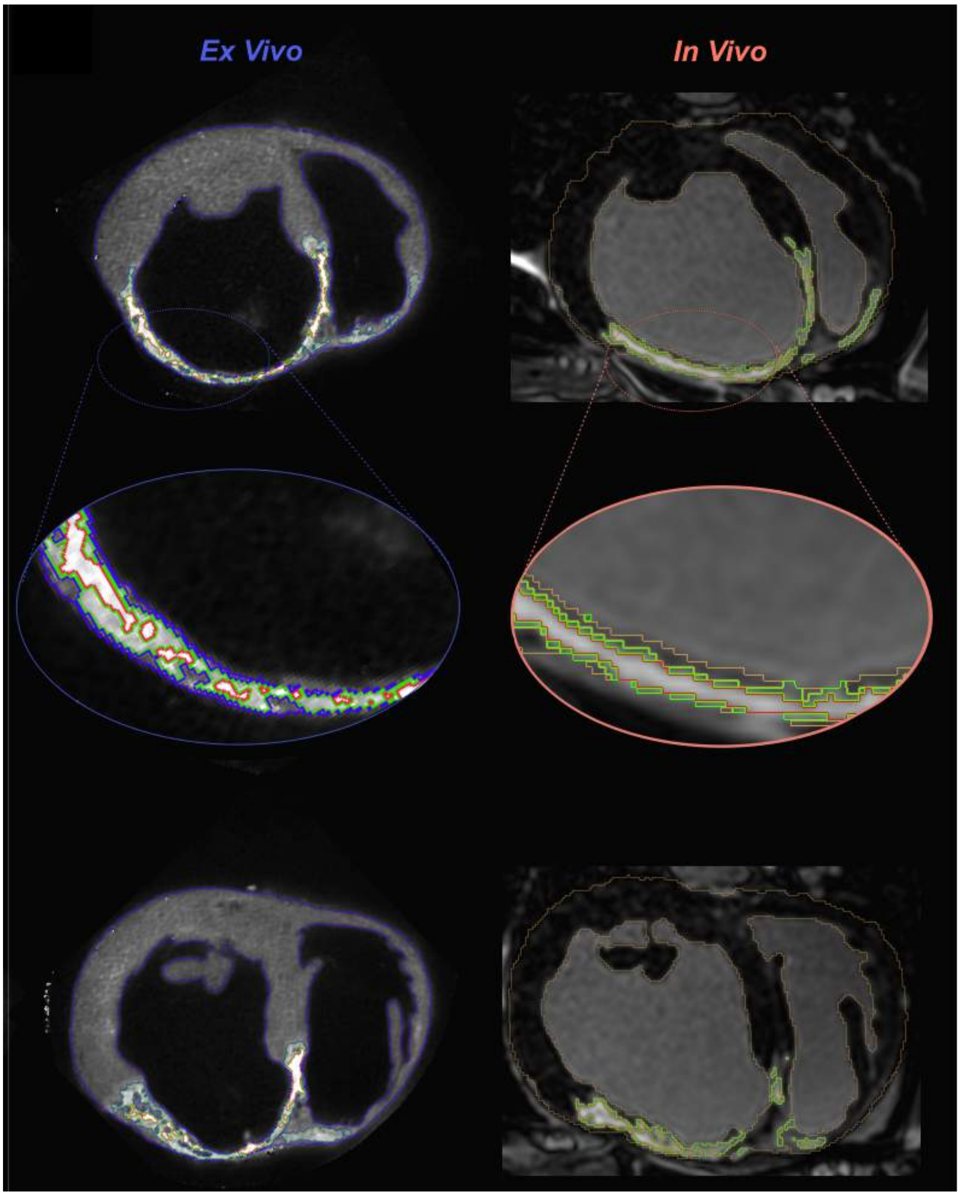

Figure 3.12: Segmentation of post-contrast CMR. Sample slices of the CMR images same case from *ex vivo* and from *in vivo* data. Dense (red) and heterogeneous (green) scars were segmented by 67% and 45%, respectively. Extra de-noising was done on *ex vivo* data.

Based on the quantifications made on the last sections for scar segmentations, we will define an optimum threshold value to distinguish between dense and heterogeneous scar for *ex vivo* and *in vivo* segmentation. The curves of Figure 3.11 were analysed and we can see that *ex vivo* data has an exponential decay, which seems to reach an asymptote at thresholds bigger than 65%. Remote scar can be thresholded around those those values.

In consequence, segmentations of the range 65-70% were shown to the expert. After further analysis, it was established that 67% was the best threshold for dense scar segmentation on both *ex vivo* and *in vivo* data. This value is approximately coincident with the $\frac{2}{3}$ of the threshold value for complete scar (45%).

The thresholds selected were the optimum ones for both T1 *in vivo* data and R1 *ex vivo* data of porcine animals on our experimental protocol, these thresholds may not be directly applied to different protocols.

In this section, we have described methods for CMR segmentations. Based on a manual refined ventricles segmentation, we have proposed a methodology to quantity false positives and the accuracy of scar segmentations when thresholds change. We hypothesize that the optimum threshold for dense and complete scar segmentation can vary due to many causes difficult to control (the contrast in the image, MRI protocol, ...). This method helps to find an optimum value for scar segmentation. Finally, to define dense scar an adequate threshold will be $\frac{2}{3}$ of the threshold value defined for complete scar segmentations at selected threshold.

As the accuracy of the scar segmentation is extremely important for this work, therefore it was worthwhile to evaluate a threshold range instead of directly applying the 50% threshold that corresponds to FWHM.

Although the selected thresholds were adequate for *ex vivo* and *in vivo* scar segmentation of our set of data, we can appreciate differences between the resulting segmented scar. The dense scar seams to be bigger and more homogeneous in most of the *in vivo* segmentations, comparing with *ex vivo* ones (Figure 3.12). Further analysis and quantification will be done in Chapter 4 to discus this observed differences.

3.3 Integration of EAM and CMR scar on a surface

The comparison of electroanatomic scar definition with scar segmented on *ex vivo* or *in vivo* CMR is not straight forward. In the EAM, the scar information is found on a surface mesh with nodal voltage data. On the contrary, the segmentation from CMR yields 3D volumes. Due to the different characteristics of data obtained by this three techniques, it will be necessary a set of computations in order to translate all data to a reference geometry.

Electroanatomic maps provide valuable information about the electrical behaviour of the heart, but the geometry is not accurate. The EAM surfaces were not well scaled, in Figure 3.13 we can see how the epicardial wall intersected with the endocardic walls. Ventricle walls of the 3D reconstruction from CMR segmentation were more detailed that the ones from EAM surfaces. For this reason the endocardic and epicardic myocardial walls of both ventricles from *in vivo* or *ex vivo* CMR reconstructions were chosen as reference.

The references surfaces will be different in the EAM surfaces comparisons against *in vivo* CMR or with *ex vivo* CMR because, due to differences on image resolution, CMR ventricle walls they were not coincident. This differences between CMR *in vivo* and *ex vivo* will be evaluated directly in Chapter 4, as they were both volume data that can be directly compared.

Ventricle walls surfaces from CMR were chosen as reference geometries, but the segmented scar from CMR was a 3D volume mostly within the myocardial walls. It was necessary to project the volume scar from CMR onto the ventricle walls. Moreover, taking into account that bipolar voltage maps do not provide transmural information (only subendocardic and subepicardic data), we must project only the subendocardic and subepicardic CMR scar on walls surfaces.

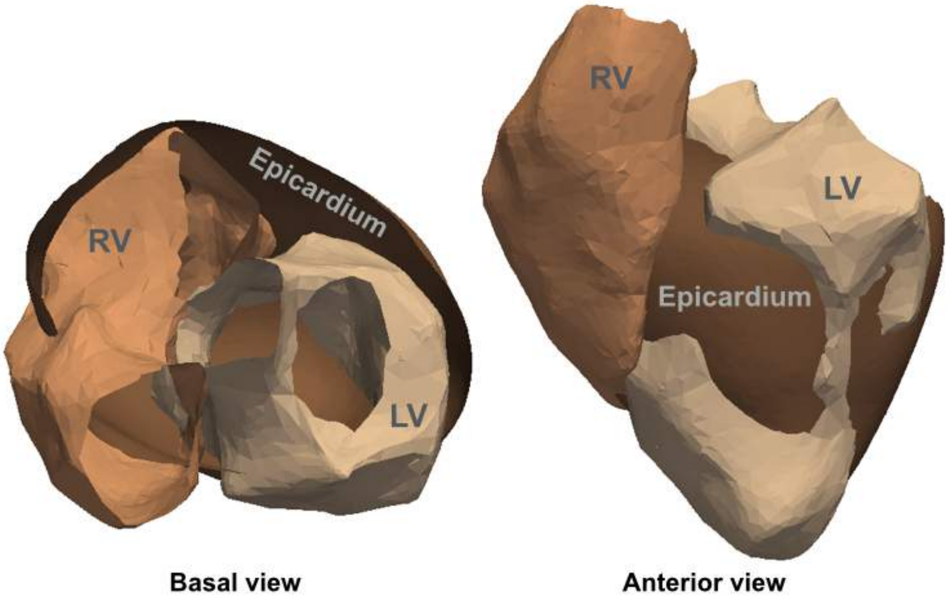

Figure 3.13: Integration of EAM and CMR. Epicardial and endocardial (LV, RV) EAM surface meshes from the electrophysiological study.

The state of the art for comparisons between scar defined by EAM data and by CMR includes many different methodologies. The simplest one is region comparisons to evaluate if there is a match between the scar defined by both techniques [56, 96]. A more detailed analysis, and the one we have chosen, is to take as reference ventricle walls from CMR reconstructions [90, 73]. More complex techniques has been proposed such as 2D bull's eyes analysis where a quasi-conformal map is applied to represents the data on a disk, the reference geometry [84]. We reject to use this last methodology because it will be really hard to implemented for right endocardium analysis.

Talking about right endocardium comparisons of EAM and CMR, few works have been found [16, 52] and both preformed just region analysis. This is due to the difficulties that RV incorporate, such as the EAM acquisition with a good level of accuracy or the right endocardium geometry.

In this section, we will explain how we integrate the EAM voltage mapping in the reference surface from CMR and how the volume scar from CMR was integrates as a surface scar, so that we can have all data on the same geometry. The integration of the experimental data (EAM-CMR) will be done the complete ventricles, including right and left endocardium and epicardium.

3.3.1 Surface Registration

The surface registration between EAM and CMR surfaces aims to integrate the electrical data from EAM on the ventricle surfaces from CMR. The alignment of EAM with CMR reference surface is typically done thought rigid registration based on anatomical landmarks. An improvement is given by the Iterative Closest Point (ICP) method [15]. More complex methods, such as conformal mapping [84] can also be find on the literature.

Due to the high density of acquisition points on the EAM and the resemblance of EAM geometries with the ones from *ex vivo* and *in vivo* CMR, we considered that rigid registration was enough to get accurate results for integration of the voltage information on CMR surfaces. The first step was landmark registration, after the ICP algorithm was applied (Figures 3.14, 3.15). Finally, when the surfaces were aligned the voltage from EAM surface was mapped on the CMR surface by the closest point mapping method.

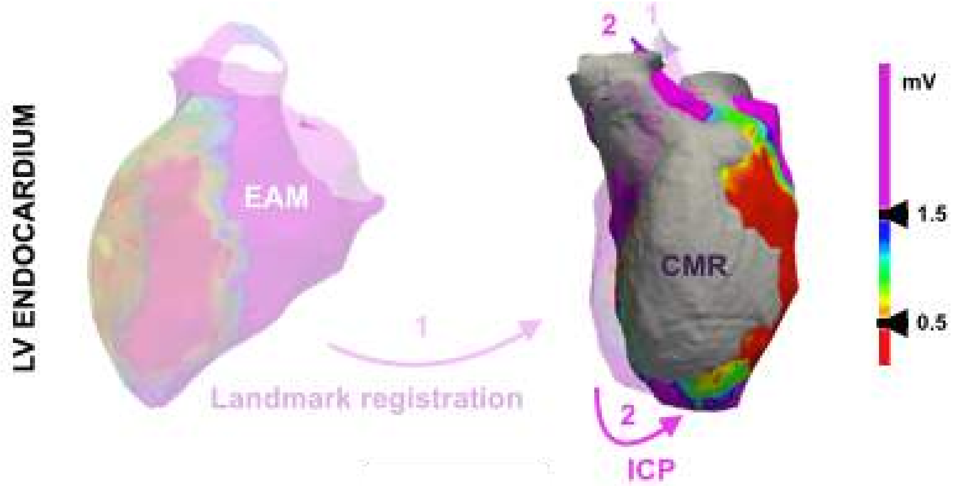

Figure 3.14: Integration of EAM and CMR. Rigid registration between LV endocardium of EAM and *ex vivo* CMR surfaces in two steps: 1) Landmark registration 2) ICP.

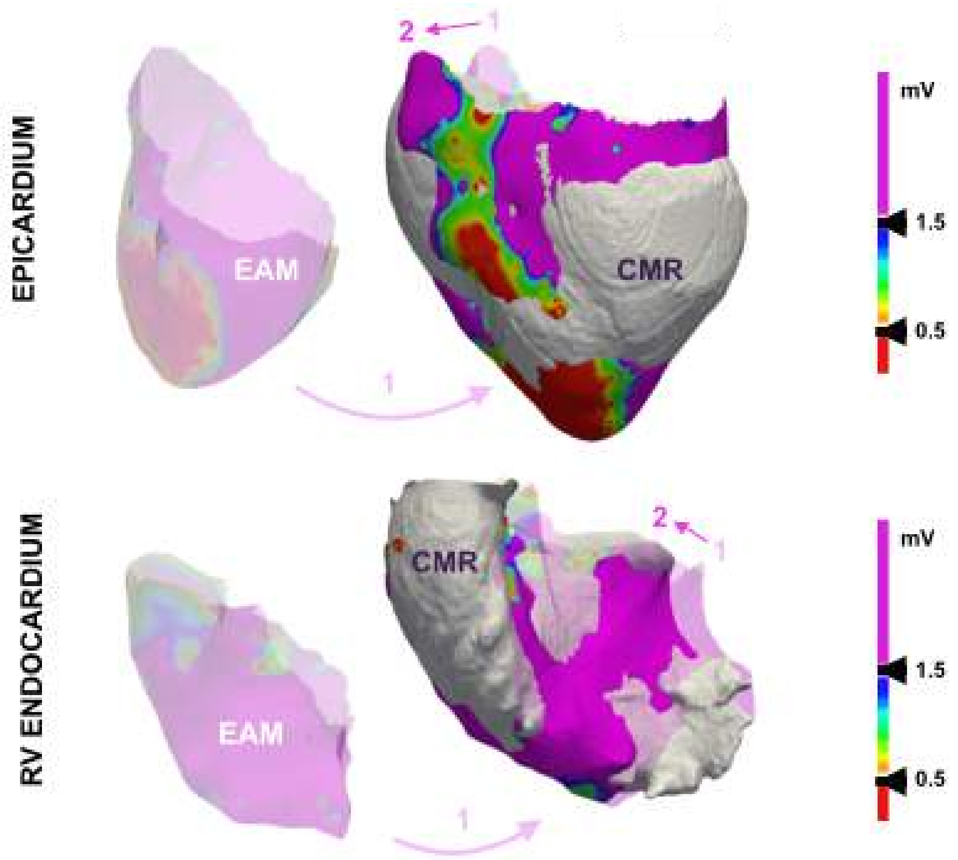

Figure 3.15: Integration of EAM and CMR. Rigid registration between epicardium and RV endocardium of EAM and *ex vivo* CMR surfaces in two steps: 1) Landmark registration 2) ICP.

Anatomical landmarks were selected on EAM, *in vivo* CMR and *ex vivo* CMR surfaces (Figure 3.16). For LV endocardium registration, five landmarks were employed: base of aorta, apex and mitral analus (MA), posterior, right lateral and left lateral. Also five landmarks were defined on RV endocardium: right ventricle outflow tract (RVOT), TriV, two apical points and a point between tricuspid valve and pulmonary RVOT (R-Tri). Finally, for epicardium six landmarks were selected: apex, the interventricular sulcus (one point apical and other one basal) and the base, defined by three points (one opposite to the interventricular furrow, another on middle LV and a point on middle RV).

After landmark registration the surfaces from EAM and CMR had similar orientations and scales. But, the resulting registration was too sensitive to the points chosen as landmarks. For this reason, the landmark registration was only employed as the first step of our rigid registrations (Figure 3.14).

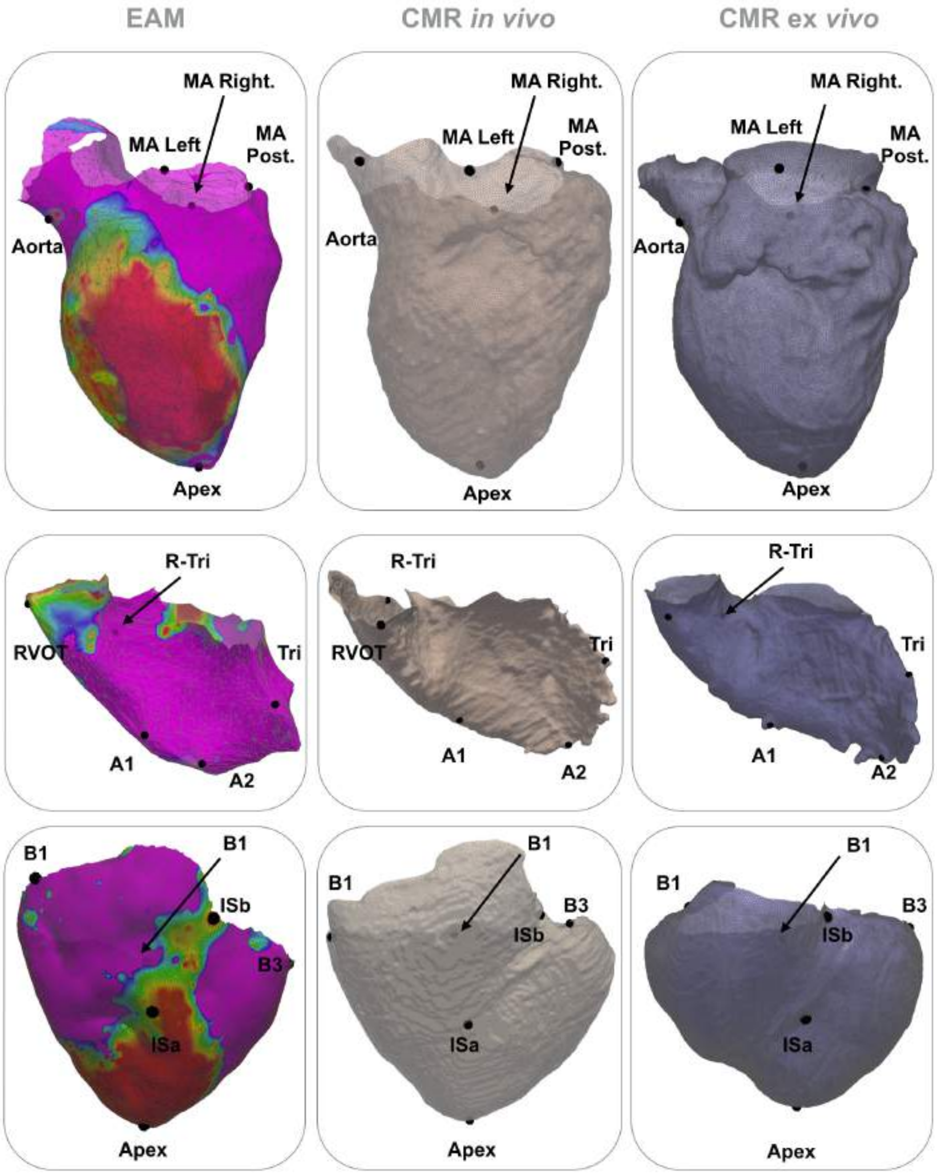

Figure 3.16: Integration of EAM and CMR. Endocardial and epicardial landmarks. A1,2, B1,2,3: RV apical and EPI basal points. ISa,b: apical, basal interventricular sulcus.

The second step was to the application of the ICP method on the resulting surfaces. The ICP is iterative method that reduces the error between two surface meshes using rigid transformations. After the ICP, EAM registered surfaces were closer to the CMR reference surface and less depended on the landmarks selected (Figure 3.14).

Finally, with the EAM surface and CMR surface aligned, a mapping was performed to integrate the EAM voltage information on the CMR surface mesh. The closet point algorithm was the approximation employed for this mapping. The results were CMR ventricle walls meshes with voltage nodal information from EAM, as in the example shown in Figure 3.17.

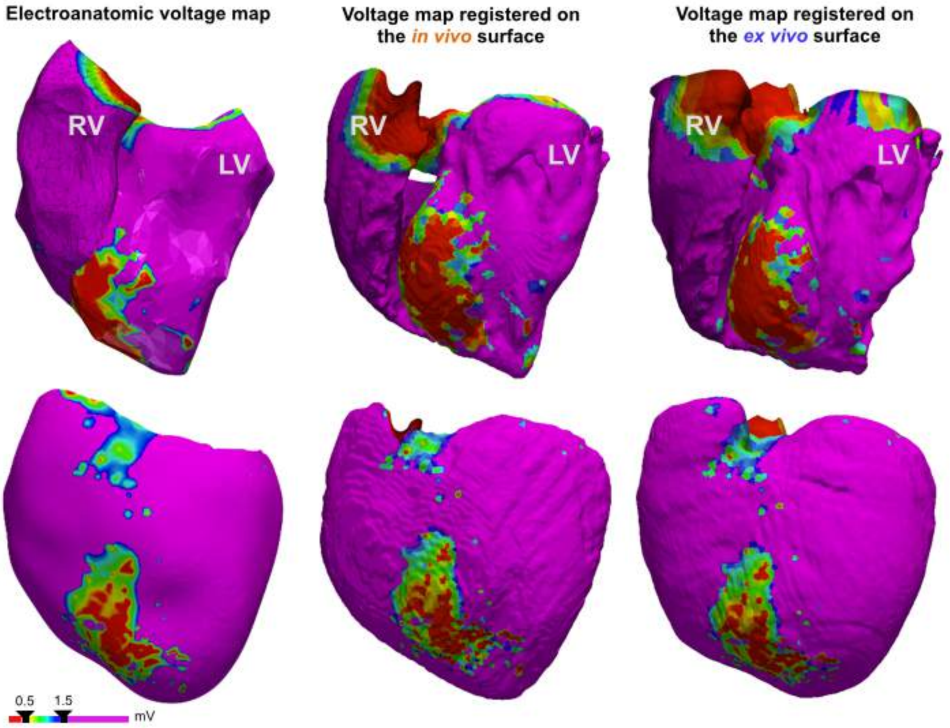

Figure 3.17: Integration of EAM and CMR. Voltage maps of endocardial (top) and epicardial surfaces (bottom) of the original EAM, the EAM registered onto *in vivo* CMR surface and onto *ex vivo* CMR surface, from left to right columns.

We have performed a rigid registration and a mapping of both ventricles walls from EAM onto *in vivo* and *ex vivo* CMR. As a result we have obtained the complete ventricle walls defined by CMR geometries with voltage information from EAM. It is important to remark that the surface registration and mapping was performed on the 3 surfaces of the ventricles: epicardium, LV endocardium and RV endocardium. We have not fount in the literature any study that perform the registration of the three surfaces of the ventricles, in particular we have not found any publication that describes right endocardium EAM registration onto the corresponding CMR surface.

Quantification of the scar areas were computed to assess if registration and mapping performed preserve the proportions of healthy tissue and scar. The nodes were consider scar if the voltage was < 1.5mV and the scar areas were computed and normalized to the corresponding surface mesh.

Total scar quantification after registrations strongly correlated with the original scar areas from EAM. After a Shapiro-Wilk normality test to assure the normality of data (EAM, registration onto *in vivo* CMR and onto *ex vivo* CMR), the Pearson correlations were computed between EAM and both registration. The R2 values obtained were 0.941 and 0.939 for in-vivo and ex-vivo registrations, respectively (Figure 3.18).

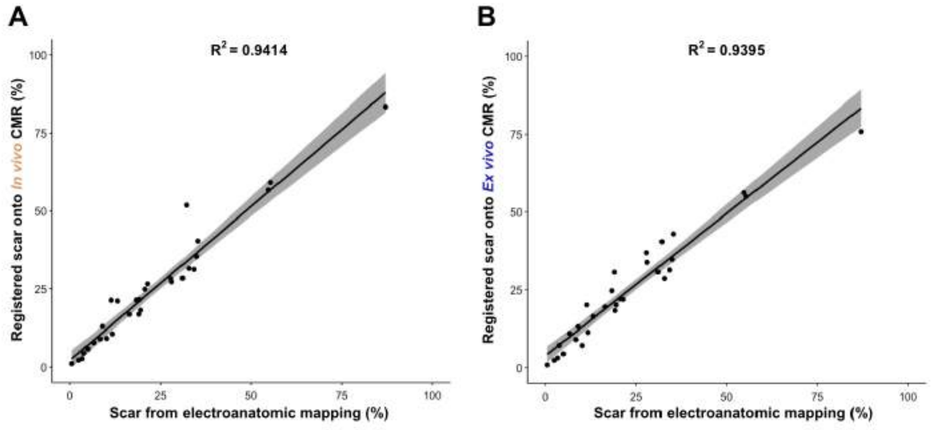

Figure 3.18: Integration of EAM and CMR. Pearson correlation analysis of voltage map from EAM and EAM registration onto *in vivo* CMR geometries (A) and *ex vivo* CMR geometries (B)

Quantification of registered and normalized voltage-derived scar tissue on the *in vivo* and *ex vivo* CMR geometries showed a median of 2.3% and 2.0% difference, respectively. In Table 3.1, the differences are shown for endocardial (LV, RV) and epicardial surfaces. Differences for right endocardium EAM registration onto *in vivo* or *ex vivo* CMR were around 3% which is good, especially because this kind of registration has not been reported in previous studies.

A Passing Bablok test was applied to confirm that those differences were not statistical significant (Figure 3.19). The slope in both cases was close to one. In particular for comparisons against registrations onto *in vivo* it was 1.005 with an confidence interval of (0.935, 1.136) and onto *ex vivo* it was 1.010 (0.900, 1.196).

We can confirm that the integration of the voltage data from EAM onto the ventricle wall did not change the percentage of scar areas. Through registration and mapping from EAM voltage was included as nodal informations on the CMR surface from *in vivo* and *ex vivo* reconstructions. It is remarkable that the procedure was performed for all ventricular walls, including right endocardium. Due to the difficulties on the EAM acquisition

Table 3.1: Normalized scar areas differences of EAM against registered EAM onto *in vivo* or *ex vivo* CMR surfaces.

	Registr. onto *in vivo*	Registr. onto *ex vivo*
LV endocardium	2.0%	2.1%
RV endocardium	2.6%	3.4%
Epicardium	1.2%	0.8%

and mismatch between CMR and EAM geometries, the integration of the voltage from electroanatomical mapping of RV endocardium on the corresponding CMR surface is difficult to find in the literature. In our case, the results for right endocardium were good and comparable to the rest of ventricle surfaces.

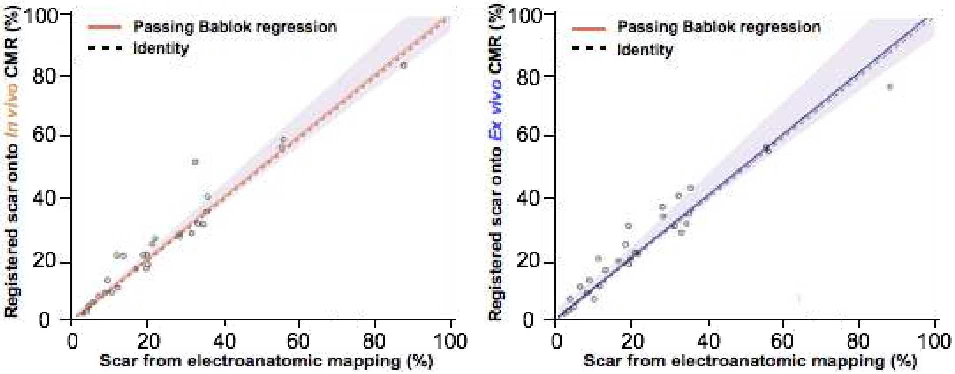

Figure 3.19: Integration of EAM and CMR. Passing Bablok test to assure that there was no significant difference between scar defined in EAM and defined in EAM registration onto *in vivo* CMR geometries(A) and *ex vivo* CMR geometries (B)

3.3.2 Scar projection

The segmented scar from CMR is always defined as a three dimensional volume. But, the reference geometry chosen was the CMR wall ventricle surfaces, that is two dimensional geometry. So, it is necessary to project the scar volume onto the ventricle surfaces.

To project the scar information in the CMR to the endocardic or epicardic surfaces most studies define a subendocardic and subepicardic layer of the segmented myocardium. Two main techniques have been reported in the literature for the scar projection. The first one the signal intensities of the voxels is averaged at a particular boundary layer after which they threshold the averaged signals to identify the scar information at the surface[90, 64, 9]. The second technique parts from the segmented volumetric scar; after which a set of layers are defined along the wall thickness. The presence or absence of scar in such layers is evaluated, quantified and then projected onto the corresponding closest boundary surface [84, 98]. In both techniques the thickness of the boundary layer was previously chosen an can be fixed (i.e. 2 mm from the encodardial wall) of proportional to the local thickness of the ventricle walls.

We propose to start from the accurate scar volume segmentations previously defined (Section 3.2), and calculate within the ventricle the distance to the scar using the Eikonal equations. Then, we will build six surface distance maps, three for dense scar description (EPI and LV,RV endocardium) and another three for the complete scar (EPI and LV,RV endocardium). If we then fixed a distance to the scar (i.e 2 mm), it will be equivalent to established a fixed subepicardic and subendoacardic layer as proposed on the literature. The advantage of this method was that we did not have to pre-defined a distance threshold for the layer.

As we want to compare the scar from CMR against the one from electroanatomic mapping, it is important to understand that catheters used for electroanatomic mapping measured a particular amount of subendocardic or subepicardic information independent of the local thickness of myocardium. We will assume that the distance of projection has to be that same for both ventricles. But as we work with distance-to-scar maps, we will not prefix a thickness layer. With this method, we will be able to compute the distance-to-scar maps and analyse the effects of changing the thickness layer employed for scar projections without extra computation when analysing the best layer thickness. We do not assume a priori a fixed thickness or wall thickness percentage.

The three myocardium surfaces (LV, RV and epicardium) will have associated two distance maps, for dense and total scar. To combine both, we have determine the optimum distance for projection and overlap the maps. Overlapped areas will define dense scar on CMR surface and areas where only total scar map is present will define heterogeneous scar on CMR surface. .

From the accurate dense and complete scar volumes defined bt the CMR segmentations, distance-to-scar maps were computed with a mathematical tool based on the Eikonal equations. A family of non linear partial differential equation (PDE) equations that are usually used for wave propagation problems and they are formally described as:

$$\begin{cases} |\nabla u| = F(x), & x \in \Omega \\ u = 0 & \text{on } \partial\Omega \end{cases} \tag{3.2}$$

where $\Omega \subset \mathbb{R}^n$, ∇ is the gradient and $|\cdot|$ the euclidean norm. The solution $u(x)$ is the shortest time to travel from the topological border $\partial\Omega$ to $x \in \Omega$.

The Eikonal equation has been previously used to calculate distance to a given surface [74, 83]. In their work, they set the time cost function F on each point x to one, $F(x) = 1$, so the solution of this particular Eikonal equation $u(x)$ describes the distance between the point x and the surface

$\partial\Omega$. We employed this particular Eikonal equation as a tool to compute the local distance to a given surface.

The distance of all ventricle points to the scar can be calculate if we consider the scar as a 3D surface, Γ_{scar}. We denoted Γ_{epi} to the epicardium surface and Γ_{LV} and Γ_{RV} to the left and right endocardium surfaces, respectively. The previous system (3.2) can be rewritten for our particular problem:

$$\begin{cases} |\nabla u| = 1 & \\ u = 0 & \text{on } \Gamma_{scar} \end{cases} \tag{3.3}$$

The solution to the previous system, equation (3.3) was computed in the whole ventricle. As show in the scheme presented on Figure 3.20, the given surface Γ_{scar} was set to 0 and on the rest of myocardium including the walls were set to infinity. Then distance was calculated as if it was a propagating wave front of distances along the myocardium. The solution was saved on the ventricle walls.

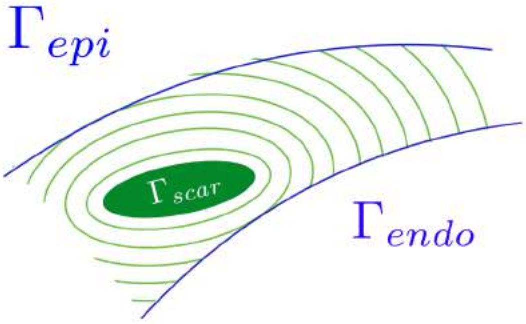

Figure 3.20: Integration of EAM and CMR. Eikonal equation scheme for distance-to-scar computations.

At the end, we obtained three distance maps for each type of scar. The solution $u(x)$ when points x are in the surface Γ_{epi} describes local distance-to-scar on the epicardic wall. Similarly, the solution $u(x)$ describes the distance-to-scar on left or right endocardic walls when $\forall x \in \Gamma_{LV}$ or $\forall x \in \Gamma_{RV}$, respectively.

For each of the ten animal cases, the equation (3.3) was solved twice. The first time with a Γ_{scar} that describes the dense scar segmented on CMR and a second time where Γ_{scar} was the complete scar boundary.

The distance-to-scar maps computed for dense and complete scar describe each type of scar once we choose a distance threshold. Different values will be analysed and compare against EAM information on the next Chapter to establish their clinical implications.

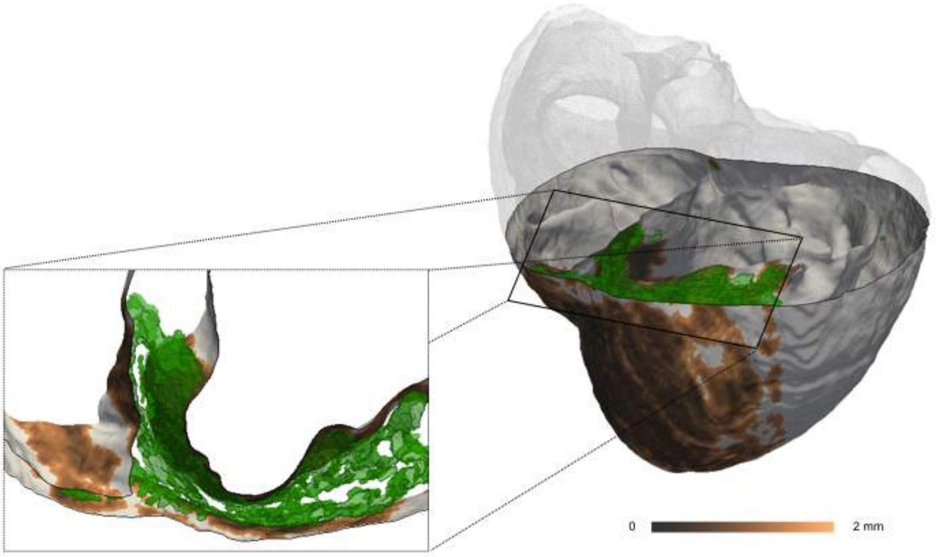

Figure 3.21: Integration of EAM and CMR. Total scar distance-to-scar maps of both ventricles and the complete scar volume reconstruction from *ex vivo* CMR.

Once a thickness layer is chosen, the distance maps will define a surface of dense scar and another one for complete scar, in overlapping areas the scar is defined as dense. Heterogeneous scar will be described by the complete scar definition with no overlapping. An example for 1 mm thickness layer, that is 1 mm threshold on the distance-to-scar maps, is show on Figure 3.22.

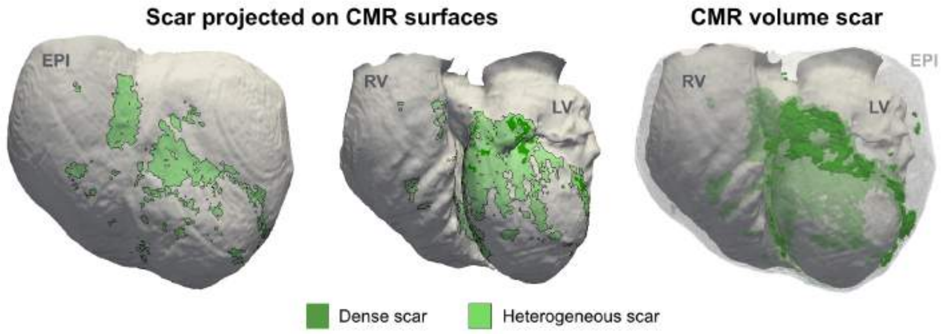

Figure 3.22: Integration of EAM and CMR. Surface scar (dense and heterogeneous) defined by 1 mm threshold on the encodardial and epicardial distance-to-scar maps, in right. In the left, the volume data from *ex vivo* CMR employed as input for the scar projection.

This method helps to scrutinise different values of subendocardial and subepicardial layer thickness with only solving once the Eikonal equation. Areas could be computed for each distance threshold, that corresponds to assume different thickness for the layer.

3.4 Fibre orientation from DTI

The DTI is a magnetic resonance sequence based on water diffusion properties employed to reconstruct the myocardial fibres [36]. The DTI sequences were obtained during *ex vivo* CMR procedure. Some DTI parameter were obtained, such as the main eigenvector and finally the cardiac tractography was computed to get the 3 dimensional reconstruction of the myocardial fibres.

$$\mathbf{D} = \begin{bmatrix} D_{xx} & D_{xy} & D_{xz} \\ D_{xy} & D_{yy} & D_{yz} \\ D_{xz} & D_{yz} & D_{zz} \end{bmatrix}$$

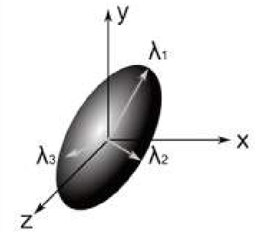

Figure 3.23: Fibre orientation from DTI. Diffusion tensor (**D**) and it ellipsoid representation. Image modified from [104]

The DTI parameters were obtained for all voxels within ventricles, previously labelled as healthy, dense scar or heterogeneous scar. Since every voxel has an associated diffusion tensor, each voxel can be represented by an ellipsoid.

The major axes of this ellipsoid are given by the eigenvectors with a magnitude given by the eigenvalues. Several tensor shape-derived parameters were obtained from DSIstudio [39]: main, second and third eigenvalues ($\lambda_1, \lambda_2, \lambda_3$), and eigenvectors ($v_1, v_2$ and v_3, respectively).

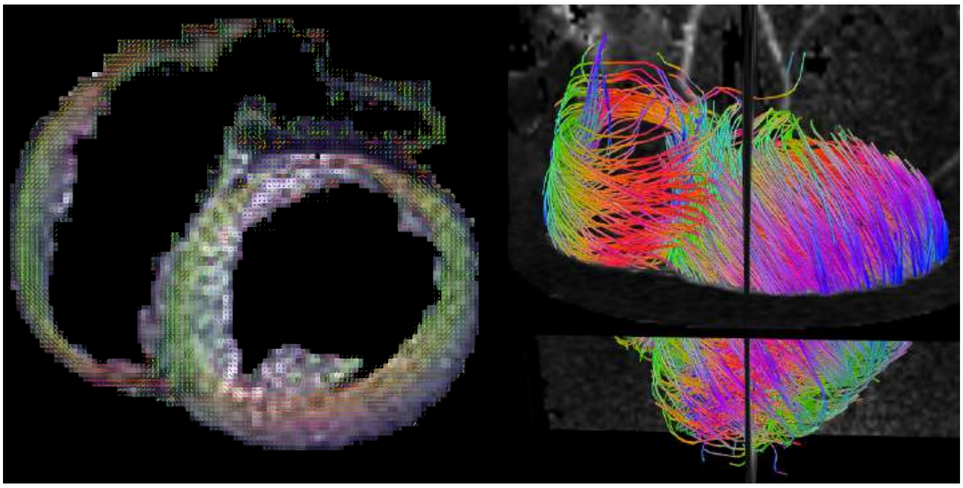

Figure 3.24: Fibre orientation from DTI. Slice plotting the main eigenvector on each voxel and the corresponding tractrography of a control case.

The cardiac tractography is post-processing technique able to create a 3D description of cardiac fibres from DTI voxel tensors. A sample tractography is shown in Figure 3.24, including the a slice of the DTI image with the main eigenvector plotted.

The fibre reconstructions based on DTI will be key for the computational models described in the second part of this thesis.

Chapter 4

Implications of infarct-related scar characterization

In this chapter, we will present the main results obtained from the post-infarction experimental study. Animal data was obtained as described in Chapter 2 and post-processed as presented in Chapter 3.

Post-infarct substrate characterization based on imaging tools is a common approach to evaluate the risk of arrhythmia and identify potential target areas for ablation procedures [6, 90]. Post-contrast CMR is a well accepted technique to describe structural changes on the heart [4]. On the other hand, low voltage areas of EAM are also related with post-infarction substrate and they have been related to the presence of arrhythmias [4, 60]. Both techniques have limitations that may affect the substrate characterization. In the case of CMR images limitations are due to partial volumes effects [79], and in the case of EAM data they due to characteristics of the catheter employed or the presence of attached fat in the epicardial ventricle walls. Experimental CMR *ex vivo* sequences provide a high-resolution reference to study the optimal interpretation of lower resolution techniques employed in the clinics.

The volumetric scar from post-contrast CMR has been proposed as predictive marker for VT after MI, but remains controversial [78, 44]. However, the LVEF is still the main marker for stratification risk [2].

In this chapter, we will first characterize the post-infarction substrate (Section 4.1) using different imaging and invasive techniques: EAM, *in vivo* and *ex vivo* post-contrast CMR. We will compare the scar description given by each technique. Once the scar is characterized, we will study if the scar volume from *ex vivo* or from *in vivo* post-contrast CMR segmentation are potential predictor for VT (Section 4.2). Animals will be divided into two groups, those where VT was induced and those where only VF was induced. We will analyse if the scar volume is able to distinguish between groups. Finally, the main conclusions and limitations of the full experimental study will be summarized (Section 4.3), including implications of the experimental study for cardiology and for computational models.

The results presented on this chapter are based on the experimental study that was performed between September 2015 and January 2017. Two publications derived from this work [31, 49].

4.1 Multi-modal scar characterization

Electroanatomic mapping, post-contrast CMR *in vivo* sequences and post-contrast CMR *ex vivo* sequences had intrinsic differences in the level of acquisition resolution. This resolution differences can affect the definition of the scar obtained from each technique, especially in small thickness walls of ventricles (Figure 4.1).

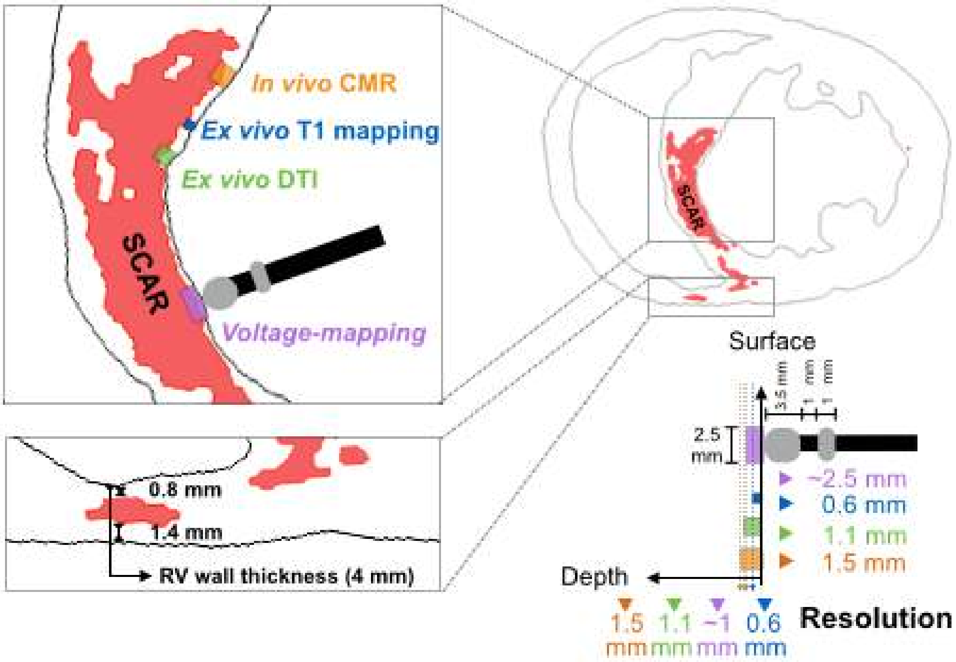

Figure 4.1: Multi-modal scar characterization. Scheme of the three techinque acquisition resolution and how they can afect when localizing scar.

Some of the differences on the descriptions of the ventricles geometries are related with the difficulties to define the same basal limits of ventricles among techniques. It is not straightforward to define the basal limit up to exactly the same point on all experimental measures. Also, we must remark that the electroanatomic mapping is not well scaled. As we have shown in Chapter 3, the endocardial walls intersect with epicardial walls on EAM data. In Table 4.1, we summarize the resolution accuracy, the ventricle wall areas, the voltage information points acquired in the EAM and the acquisition times of imaging tools.

Table 4.1: Characteristics of EAM and CMR data acquired from 12 pig but the median and interquartile range values

	Electroanatomic voltage mapping	**Post-contrast CMR**	
		in vivo	***ex vivo***
Resolution [mm]	Catheter tip-ring:		
Acquisition	3.5-1	$1.5 \times 1.5 \times 1.5$	$0.6 \times 0.6 \times 0.6$
Reconstruction		$0.57 \times 0.57 \times 0.57$	$0.45 \times 0.45 \times 0.451$
Acquisition time [min]	**167** (149,191)	**15**	**45**
Surface areas [cm^2]			
LV endocardium	**169.50** (163.00, 182.80)	**157.00** (143.00, 166.20)	**149.50** (130.20, 176.00)
RV endocardium	**141.50** (137.80, 153.00)	**139.00** (124.20, 147.80)	**167.50** (144.20, 187.50)
Epicardium	**203.00** (186.00, 213.20)	**253.50** (232.00, 274.50)	**258.00** (137.00, 292.50)

In this section, we will first discuss about how the scar is defined by different voltage threshold on EAM data. Then, volume scar defined using *in vivo* and *ex vivo* post-contrast CMR will be compared to analyse how the downgrade of accuracy affects the scar definition. The next step will be to compare the three mentioned techniques and find the better interpretation of clinical tools (EAM and *in vivo* CMR) taking as reference the *ex vivo* post-contrast CMR scar definition.

Results presented in this section are based on a small population (n=10) and imaging data from the specific experimental protocol described in Chapter 2. It is not possible to extrapolate our results as general findings, but they are valuable results to design more general study with a specific acquisition and analysis methodology.

4.1.1 Electrophysiological scar characterization

The electroanatomic maps were built based on geometry description and voltage information points acquired during the electrophysiological study (Chapter 2) and post-processed as described in Chapter 3. The scar was described on both ventricles on the basal electroanatomical maps by voltage threshold criteria.

Conventional cutoff criterion (< 1.5 mV) was applied to define the complete scar. The areas below this low voltage threshold were calculated and normalized to the corresponding surface area (LV endocardium, RV endocardium or epicardium).

The normalized scar median was the 32.57% of the LV endocardium, with an IQR of 27.93-49.79%. On the case of the RV endocardium, the

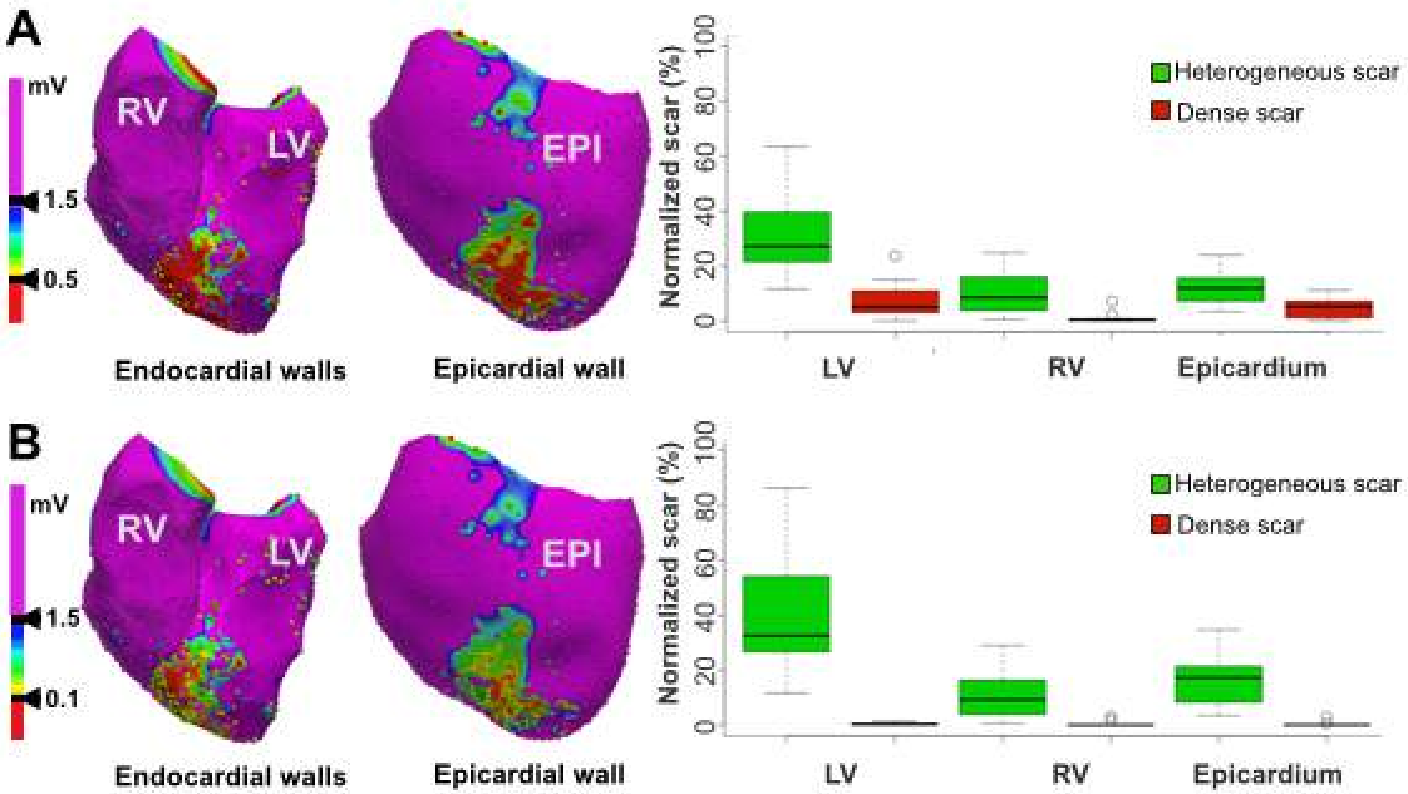

Figure 4.2: Electrophysiological scar characterization. Sample case of electroanatomic mapping unig two thrshold criteria: <0.5mV (A) and <0.1 mV (B). In the left of each panel, boxplot of normalized areas by both criteria.

normalized scar area was 10.06% with IQR 4.47-15.53% and 18.69% with IQR 8.70-20.93% on the case of epicardial scar area. For dense scar, there is not a standard criteria, so two very low voltage criteria, < 0.5 mV and < 0.1 mV, were assessed. It was observed that the dense scar description was sensitive to the voltage criteria.

Dense scar voltage criterion affects substrate characterization The dense scar normalized defined from conventional very low voltage criterion (<0.5 mV) led to 5.09% with IQR 2.97-9.86% of the LV endocardium. For epicardium the dense scar under 0.5 mV was similar, a normalized surface of 5.27% with IQR 1.34-6.98%. In the case of RV endocardium, the dense scar using the same voltage criteria was lower 0.36% with IQR 0.07-0.74%.

Decreasing the dense scar very low voltage cutoff to <0.1 mV has been suggested to be more specific to detect unexcitable areas. A strong decrease was found in the amount of dense scar using 0.1 mV as criterion of both LV endocardium (0.17%, IQR 0.00002-0.65%) and epicardium (0.025%, IQR 0.0002-0.08%) ventricle walls. Dense scar in RV endocardial wall was negligible using 0.1 mV as threshold criterion (Figure 4.2B).

4.1.2 Volume scar characterization from post-contrast CMR

Segmentations of CE-CMR from *in vivo* and *ex vivo* data show geometrical differences (Figure 4.3), as we have described in Chapter 3. The level of accuracy due to acquisition resolution, motion artefacts and partial volume effects could explain them. Moreover, *ex vivo* post-contrast CMR is not available in clinics, so it will be important to compare it against *in vivo* post-contrast CMR to identify the limitations of this clinical tool.

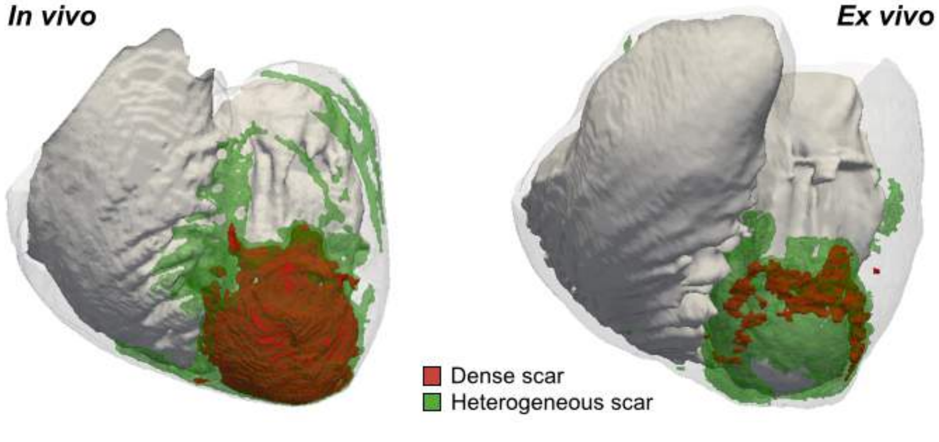

Figure 4.3: Volume scar characterization from post-contrast CMR. 3D reconstruction of the same sample case based on segmented post-contrast *in vivo* and *ex vivo* CMR.

The volumetric scar from the scar segmentations performed on the *in vivo* and *ex vivo* post-contrast CMR was quantified and compared. An analysis was performed to compare the definition of both types of scar obtained using both techniques.

Post-contrast *in vivo* CMR defines a lager dense scar compared with *ex vivo* CMR. The three dimensional reconstruction of dense scar segmentations done on the *in vivo* post-contrast sequences had a median volume of 5.431 cm^3, with IQR 3.976-7.851 cm^3. It was higher than one based on *ex vivo* post-contrast CMR segmentations that define a median volume of 2.121 cm^3, with IQR 1.908-4.480 cm^3.

The complete scar volume was the sum of dense and heterogeneous scar volumes. Total scar volumes were more similar between both imaging techniques segmentations. The scar volume from *in vivo* post-contrast CMR was 17.800 cm^3, IQR 13.440-28.790 cm^3, and in the case of *ex vivo* the scar volume was 21.870 cm^3, IQR 14.960-23.460 cm^3. After the normalization of scar volumes to biventricular volume, it is clearly shown that complete scar volumes can be consider similar for both datasets, but dense scar segmented from *in vivo* is larger than dense scar from *ex vivo* data (Figure 4.4).

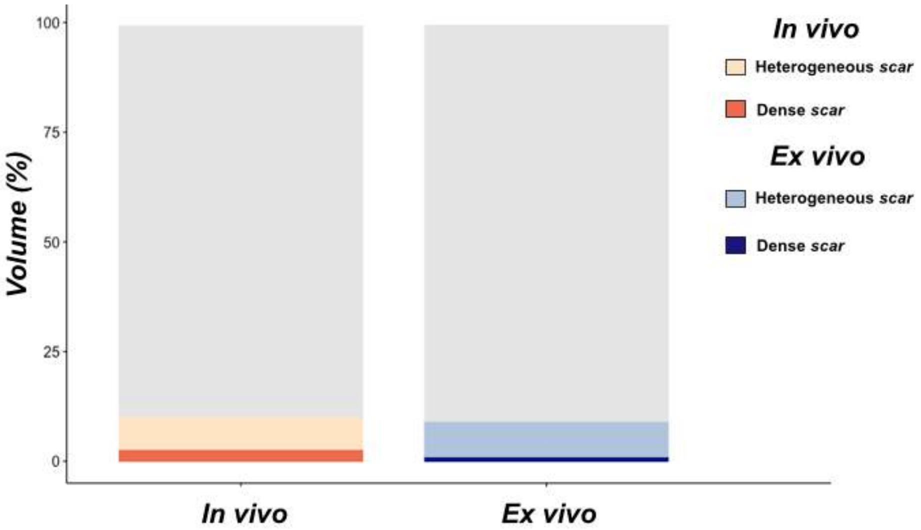

Figure 4.4: Volume scar characterization from post-contrast CMR. Normalized volumes of healthy tissue and dense and heterogeneous scar from post-contrast CMR 3D reconstructions.

We can conclude that *in vivo* post-contrast CMR sequences are useful to identify scar tissue, but are not able to classify the scar into dense and heterogeneous in an accurate way. For studies on re-entrant circuit localization, this can be a big limitation.

4.1.3 Comparisons of voltage-based substrates with surface scar projections from CMR

The comparisons between EAM and CMR scar definitions were done on the ventricle surface walls from CMR segmentation. Three surfaces were defined: LV endocardium, RV endocardium and epicardium. After a rigid registration, low intensity regions located at the base of the ventricle were eliminated from the EAM registered maps, so just the scar information remains. Voltage-based maps were integrated onto those CMR surfaces through registration, as explained in Chapter 3. On the other hand, the volumetric scar from post-contrast CMR was projected onto the wall (Chapter 3), so that all the data was in the same geometry and comparisons can be directly done.

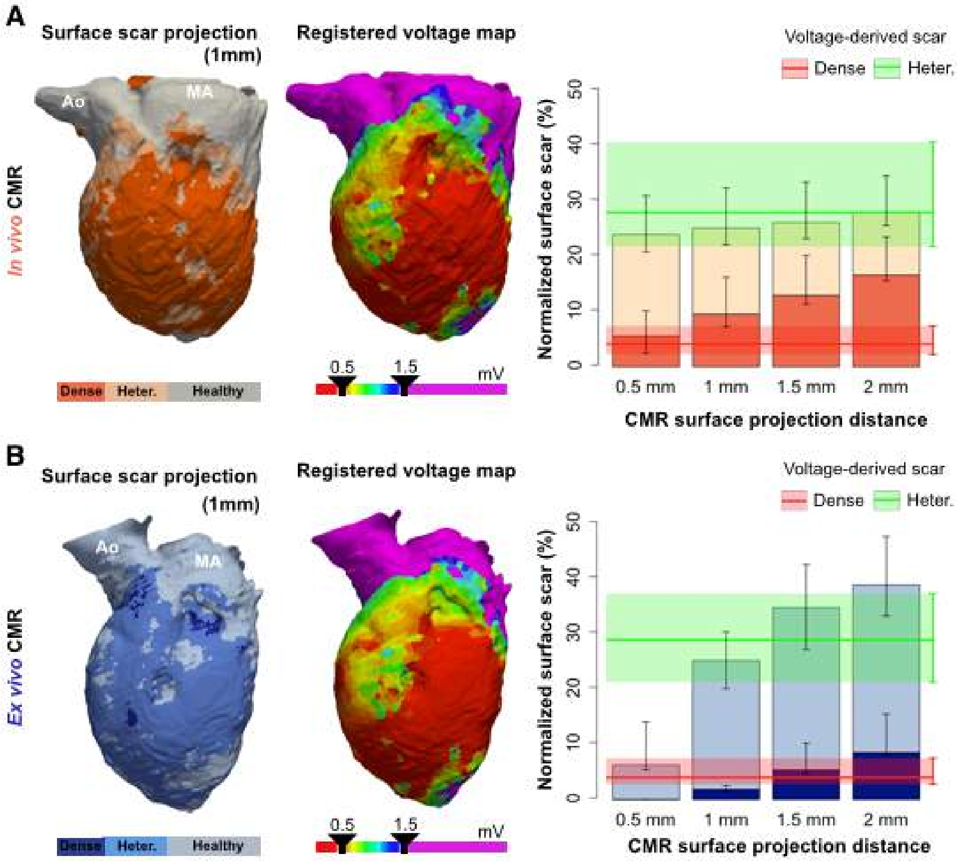

Figure 4.5: Comparisons of voltage-based substrates with surface scar projections from CMR. Analysis of LV endocardium scar on *in vivo* (A) and *ex vivo* (B) data: Registered voltage map, CMR scar projected at 1 mm and graphic of how projected scar area changes with the thickness layer.

High-resolution post-contrast CMR may distinguish thin surviving endocardial layers. The scar was defined on the voltage maps by conventional thresholds (0.5 – 1.5 mV). The projected scar from CMR was defined using a range of projection distance from 0.5 mm until 2.0 mm, on both *in vivo* and *ex vivo* data derived from post-contrast CMR. The LV endocardium voltage maps started to resemble dense and heterogeneous scar projection of data from *in vivo* post-contrast CMR at a minimum projection distance (0.1 mm). However, scar regions from *ex vivo* post-contrast CMR required deeper distance projection ($\sim$ 1.0 mm) to provide similar area results (Figure 4.5A, C). This may indicate that high-resolution *ex vivo* post-contrast CMR is able to distinguish surviving tissue in endocardial layer, just a few hundred micron thick [96], that cannot be detected using lower resolution techniques..

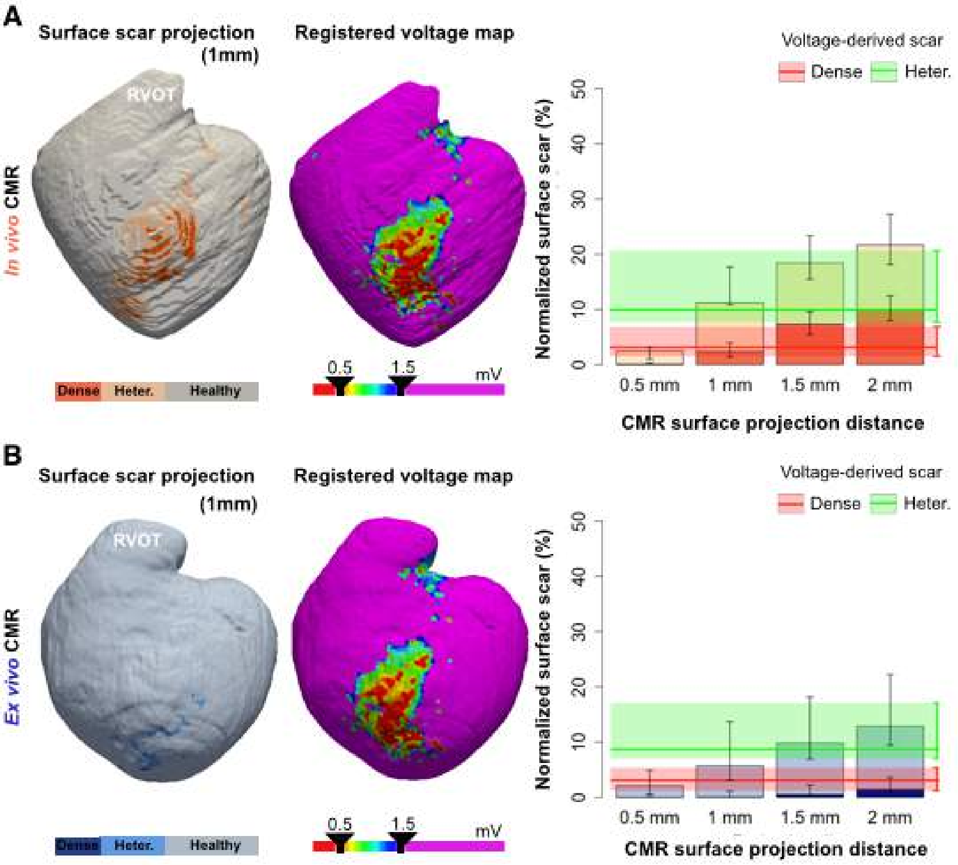

Figure 4.6: Comparisons of voltage-based substrates with surface scar projections from CMR. Epicardium analysis of *in vivo* (A) and *ex vivo* (B) data: Registered voltage map, CMR scar projected at 1 mm and graphic of how projected scar changes with the thickness layer.

Epicardial substrate quantification is not highly sensitive to CMR resolution. A similar pattern was observed on the epicardium. The heterogeneous and dense scar areas were progressively larger as the surface projection distance increased (Figure 4.6).At 0.5 mm distance for projection, the normalized scar area from CMR was smaller for *in vivo* (2.53%, IQR 1.04-3.11%) and for *ex vivo* (2.12, IQR 0.48-4.89%) in comparison to the voltage-derived scars registered onto the *in vivo* surface (9.93%, IQR 7.70-20.63%) and registered onto the *ex vivo* surface (8.70%, IQR 7.01-17.11%). This differences can be due to the potential effects of the attached fat on the epicardial voltage maps, that were minimized with fine epicardial CMR segmentations, especially from *ex vivo* high-resolution sequences.

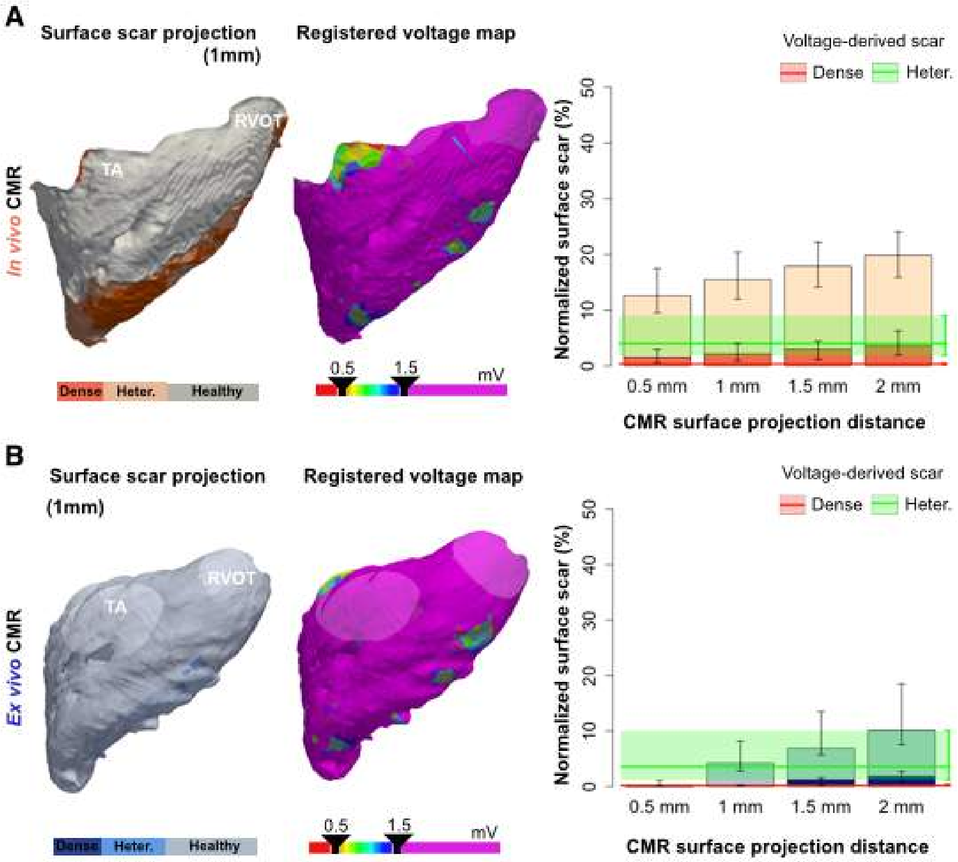

Figure 4.7: Comparisons of voltage-based substrates with surface scar projections from CMR. Analysis of RV endocardium scar on *in vivo* (A) and *ex vivo* (B) data: Registered voltage map, CMR scar projected at 1 mm and graphic of how projected scar changes with the thickness layer.

Scar-related information within thin walls seems to be very sensitive to CMR resolution. Thinner ventricular walls, such as RV free wall, can be affected by the CMR resolution. The RV endocardium voltage-derived scars were consistently smaller than the ones defined on the post-contrast *in vivo* sequences at all of projection distances evaluated. Scar comparisons using *ex vivo* high-resolution post-contrast images showed that RV voltage-maps resembled CMR scar tissue at 1 mm of the projection distance from the RV endocardium (Figure 4.7).

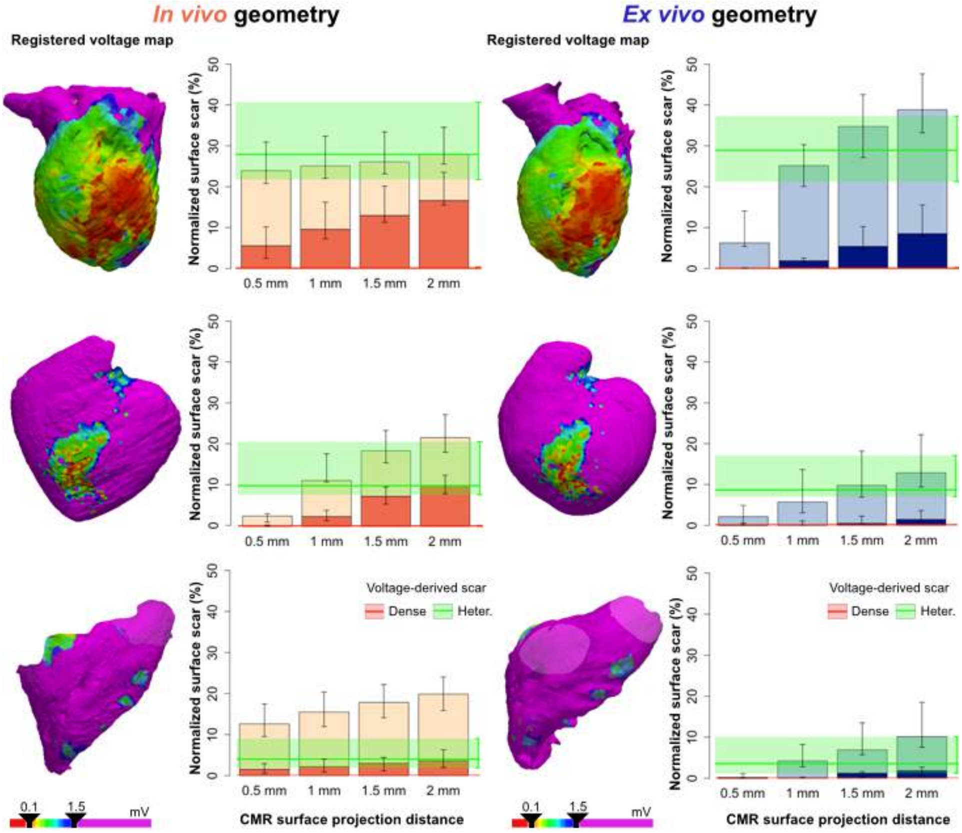

Figure 4.8: Comparisons of voltage-based substrates with surface scar projections from CMR. Analysis of *in vivo* and *ex vivo* data: Registered voltage map using 0.1 mV voltage criteria and graphic of how projected scar changes with the thickness layer.

Very low voltage criteria (0.1 mV) almost eliminate epicardial and endocardial dense scar. Adjusting voltage criteria for dense scar tissue to <0.1 mV dramatically decreased voltage derived-dense scar tissue on LV endocardium. As a result, both *in vivo* and *ex vivo* surface scar regions at different projection distances did not resemble such a small voltage-derived dense scar tissue, although the voltage-derived heterogeneous scar are similar.

This voltage threshold (0.1 mV) affected also the epicardial surfaces in the same. The dense scar dramatically decreased on voltage-derived scar tissue and it produced not good resemblance with CMR scar.

Finally, the RV dense scar was not affected by the voltage threshold chosen, under 0.5 or 0.1 mV, since in both cases the dense scar was very close to zero.

4.1.4 Interpretation of voltage maps based on post-contrast CMR scar descriptions.

The normalized complete scar tissue from CMR projected at 1 mm distance showed small differences compared to voltage-derived scar for LV endocardium and epicardium (Figure 4.10A,B). On LV endocardium, the differences were a 4.01% with IQR 1.78-9.14% for *in vivo* and a 5.00% with IQR 2.55-10.76% for *ex vivo* comparisons. For epicardium, we had similar differences: 4.941% with IQR 2.211-8.215% for *in vivo* and 5.1160% with IQR 2.996-9.312% for *ex vivo* CMR.

The RV voltage-derived scar (Figure 4.10) was also consistent with the 1 mm surface projection distance from *ex vivo* CMR, the normalized difference was 3.10%, IQR 1.65-6.24%. However, the optimal correlation of voltage-derived RV scar using lower-resolution images from *in vivo* CE-CMR occurred at the minimum (0.5 mm) evaluated surface projection distance, where the normalized difference was 8.84%, IQR 3.58, 12.70%.

A similar interpretation can be done for dense scar tissue using 0.5 mV as voltage threshold. Distance projection cutoff done at 1 mm, defined a normalized dense scar that had a 9.23%, IQR 6.14-9.82%, of difference compared with the dense scar voltage defined (<0.5 mV). For dense scar (Figure 4.9), the difference on the scar areas if we set the threshold for CMR scar projection to 0.5 mm. In this case, the difference on dense scar area was 4.25%, with IQR 1.32-4.63%.

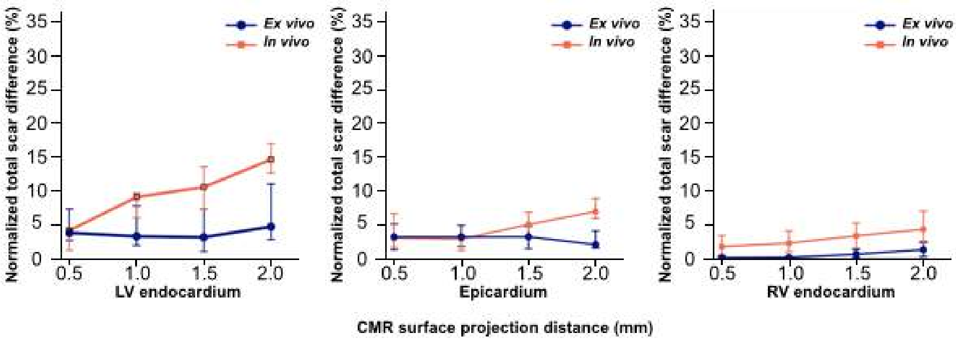

Figure 4.9: Interpretation of voltage maps based on post-contrast CMR scar descriptions. Difference between voltage derived dense scar and projected from CMR, changing with the projection distance.

The voltage-derived scar and the surface scar projected from *in vivo* post-contrast CMR showed larger normalized scar than surface scar projected from experimental high-resolution *ex vivo* post-contrast CMR.

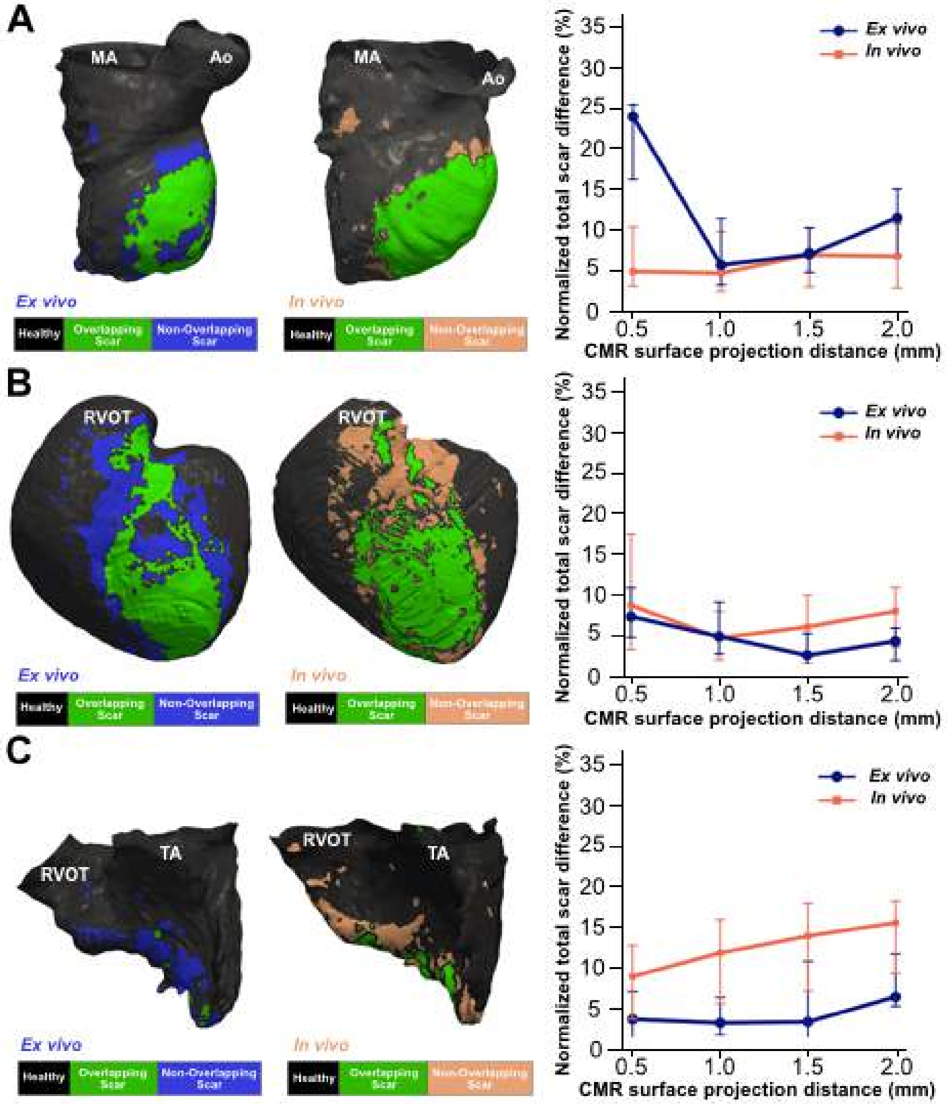

Figure 4.10: Interpretation of voltage maps based on post-contrast CMR scar descriptions. LV endocardial (A), epicardial (B) and RV endocardial (C) maps of scar differences between voltage derived and CMR projected at 1 mm scar; and how this differences vary with the projection distance for all cases, on the right column.

Clinical EAM and *in vivo* CMR define a larger scar than high-resolution *ex vivo* CMR. Whole heart voltage-derived scar (12.87% with IQR 4.59-27.15%) and surface scar projections from *in vivo* post-contrast CMR sequences (18.51% with IQR 11.25-24.61%) showed larger normalized scar tissue than high-resolution *ex vivo* CMR images (9.30% with IQR 3.84-19.59%).

4.2 Ventricular arrhythmia inducibility

Ventricular tachycardia (VT) associated to post-infarction episodes is still not well understood. Predictors for sudden death and VT inducibility are not established yet. On the clinical practice, the LVEF is the main marker employed to evaluate the risk of sudden cardiac death after MI [2]. Some studies propose that scar volumetric quantification from CE-CMR could be a predictor for inducible and spontaneous ventricular arrhythmia after MI [78, 44], although there is an overlap in the scar size on patients with and without ventricular arrhythmia [22, 3].

The objective of this section is to verify or reject the volumetric scar from*in vivo* and *ex vivo* post-contrast CMR segmentations is a marker determining VT inducibility, as described on the literature. The study was done based on experimental medical data from 15 animals (12 with MI and 3 controls).

During the electrophysiological study, animals underwent a stimulation protocol. In all cases VT or VF was induced. We classified animals into three groups: controls, VT inducible and only VF inducible.

Table 4.2: Animal description by groups: controls, VT inducible or only VF inducible.

	Control	**VT**	**Only VF**
Animals	**3**	**8**	**4**
Weight [kg]	**55** (52.75, 56.5)	**58** (53, 62.25)	**61.25** (52, 70.38)

4.2.1 Left ventricle ejection fraction analysis

The LVEF is a volumetric percentage that describes the blood ejected by the heart on a beat. The LVEF was computed from our cine *in vivo* CMR sequences as described in [31]. In the mentioned publication, a statistical study was performed to quantify if LVEF is able to distinguish between the three groups (controls, VT inducible and only VF inducible). The following conclusions are described in [31].

LVEF did not associate with VT inducibility. A statistical significant differences were observed for LVEF in comparison to only VF inducible animals and VT inducible pigs. Neither it was between controls and pigs with MI where only VF was inducible.

4.2.2 Scar volumes from *ex vivo* post-contrast CMR

Segmented R1 from post-contrast *ex vivo* CMR provided dense and heterogeneous volumetric scars. A statistical analysis was done to evaluate the power of CMR scar volumes as predictors of VT in 12 animals that underwent MI.

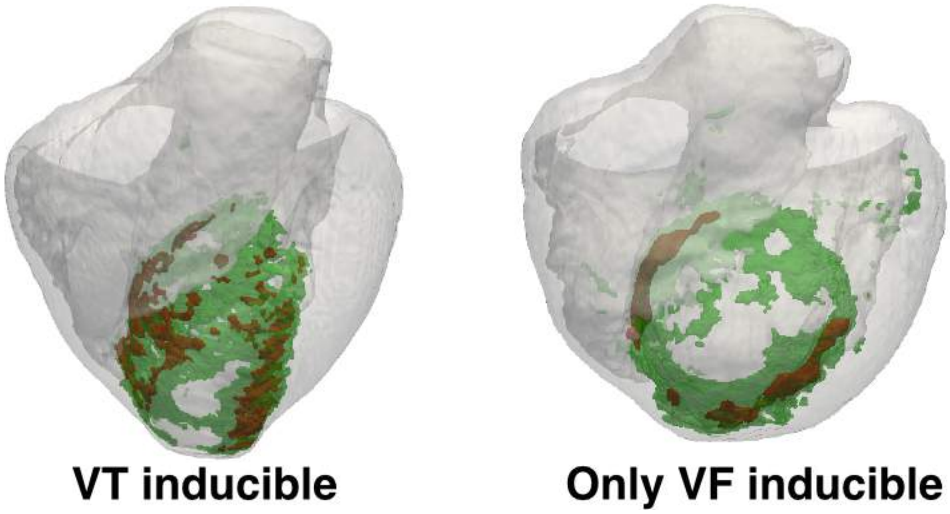

Figure 4.11: Scar volumes from *ex vivo* post-contrast CMR. Volume reconstruction from same cases of VT inducible and only VF inducible groups.

The scar volumes were calculated from CMR segmentations (Chapter 3) and compared by groups: VT inducible and only VF inducible (Table 4.3).

Table 4.3: Volumetric scar by animal groups; median and IQR.

	VT inducible	**Only VF inducible**
Heterogeneous scar [cm^3]	**30.63** (24.73, 49.03)	**25.77** (20.57, 30.9)
Dense scar [cm^3]	**4.53** (3.45, 6.39)	**6.08** (3.38, 9.26)
Total scar [cm^3]	**39.03** (29.52, 52.86)	**31.15** (23.25, 40.16)

The Mann-Whitney U test indicated that none of the scar volumes was able to differentiate between VT inducible and only VF inducible groups of animals. Two-by-two groups comparisons were considered statistically significant if $p < 0.05$. As presented on Figure 4.12, none of the scar volumes (dense, heterogeneous or total scar) was able to differentiate between animals who induced VT and those who did not.

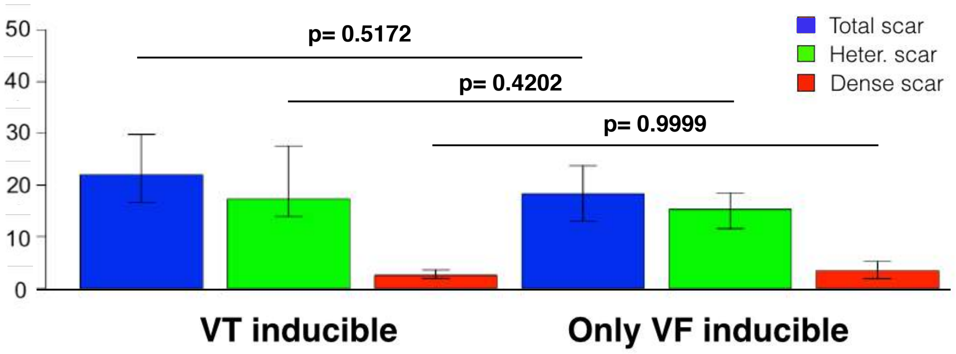

Figure 4.12: Scar volumes from *ex vivo* post-contrast CMR. It was not able to differentiate between cases where VT inducible and cases where only VF inducible

Scar volumes from *ex vivo* CMR did not associate with VT inducibility. Scar volumes were not able to classify animals into VT inducible and only VF inducible. This might contradict some studies that show scar volume as a predictor [78], but it is in accordance with the fact that CMR scar volumes has not yet been incorporated to the clinical protocols [38]. This field remains controversial, one of the reasons of the contradictory results that appear on the literature could be the differences on the acquisition resolution, acquisition times or the lack of standard protocol for scar segmentations.

4.2.3 Scar volumes from *in vivo* post-contrast CMR

We have just concluded that scar volumes from *ex vivo* CMR were not able to differentiate animals where VT was induced to those where only VF was induced. Despite that *ex vivo* resolution is better, the available data in clinics is *in vivo* CMR.

To ensure the results showed for *ex vivo* scar segmentations are still true on *in vivo* scar segmentations, we will perform the same statistical study but this time based on the scar volumes from *in vivo* CMR segmentations. Results are expected to be similar but this is not straight forward due to the differences between *ex vivo* and *in vivo* scar volumes shown in Section 4.1.2 of this chapter.

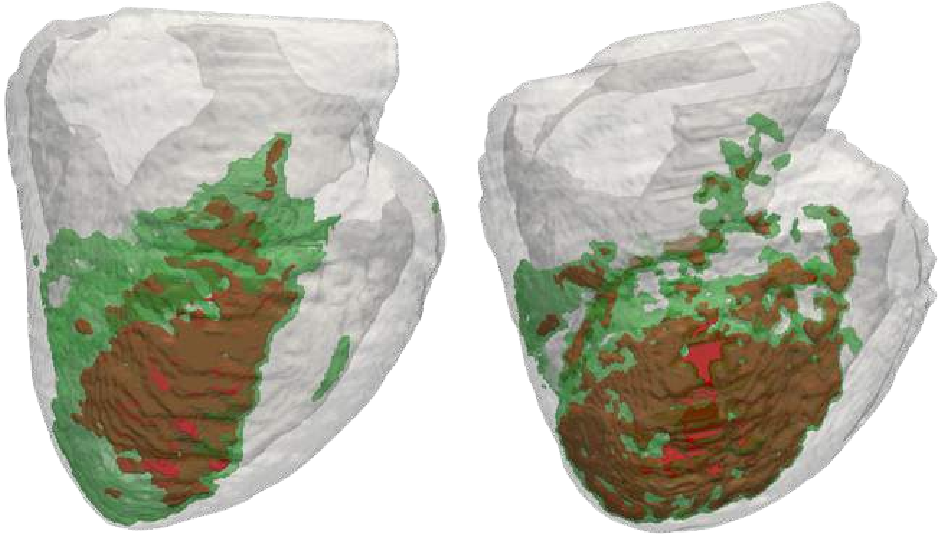

VT inducible **Only VF inducible**

Figure 4.13: Scar volumes from *in vivo* post-contrast CMR. Volume reconstruction from same cases of VT inducible and only VF inducible groups.

The Mann-Whitney U test was applied to evaluate if the *in vivo* scar volumes (Table 4.4) are able to differentiate between the groups of animals VT inducible and only VF inducible. In this case 10 animals were available for the study, 7 on VT inducible group and 3 on only VF inducible group.

Table 4.4: Volumetric scar by animal groups; median and IQR.

	VT inducible	**Only VF inducible**
Heterogeneous scar [cm^3]	**13.56** (11.76, 17.74)	**10.24** (8.13, 11.18)
Dense scar [cm^3]	4.82 (4.19, 8.75)	6.04 (3.82, 6.34)
Total scar [cm^3]	**22.83** (15.6, 24.28)	**16.28** (11.95, 17.53)

CMR *in vivo* scar volumes did not associate VT inducibility. Scar volumes from *in vivo* segmentations were not able to differentiate between groups of animals (Figure 4.14) for complete, dense or heterogeneous scar.

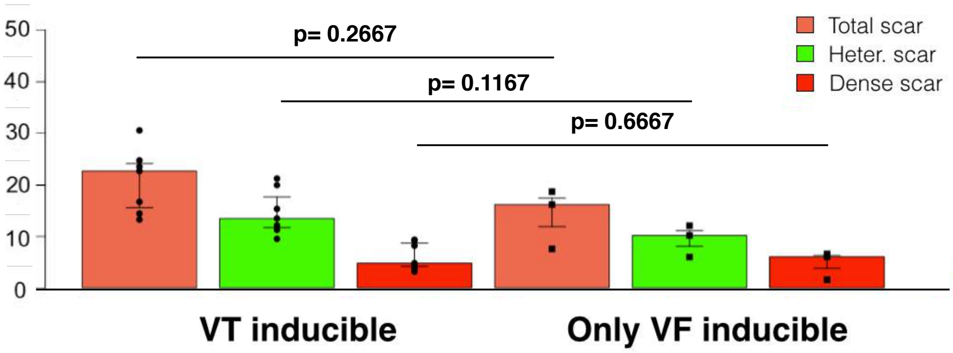

Figure 4.14: Scar volumes from *in vivo* post-contrast CMR. It was not able to differentiate between cases where VT inducible and cases where only VF inducible.

Despite the low number of cases, we can say that none *in vivo* or *ex vivo* scar volumes were found to be possible predictors for VT on this study based on experimental pig data.

4.3 Main conclusions of experimental study

Some conclusions were extracted from the set of experimental procedure through data post-processing and analysing. However, any change on the experimental protocol for data acquisition could vary the results, they cannot be directly extrapolated to other data from experimental protocols. Despite this, they can help to open research lines and help on clinical practices. The main objective of this part of the thesis was to discus the problems related with the scar definition based on experimental data and study its relationship with ventricular tachycardia. The major finding of the this study (Part I of the thesis) were:

Scar characterization:

1. **Dense scar voltage criterion affects substrate characterization.**
2. **Dense scar is sensitive to post-contrast CMR resolution.**
3. **High-resolution *ex vivo* post-contrast CMR may distinguish thin surviving endocardial layers.**
4. **Epicardial substrate definition was not sensitive to the CMR resolution.**
5. **Thin walls are affected by CMR resolution.**
6. **Very low voltage criteria (0.1 mV) almost eliminated epicardial and endocardial dense scar.**

7. **Clinical tools (*in vivo*) define larger scar than high-resolution *ex vivo* CMR.**

Ventricular arrhythmia inducibility:

10. **LVEF is not associated to VT induction.**
11. **Scar volumes from *ex vivo* CMR do not associate to VT induction.**
12. **Scar volumes from *in vivo* CMR do not associate to VT induction.**

Part II

Electrophysiological simulations

Chapter 5

Computational electrophysiology model

Continuous waves of depolarization and repolarization can be modelled under the continuum mechanics hypothesis. In the tissue scale the electrophysiology model can be seen as a transient diffusion PDEs which includes a term that describes the ion cell kinetics, modelled by an ordinary differential equation (ODE) system. Cardiac electrophysiology simulations employ the finite element method (FEM) to obtain three dimensional accurate description of the electric wave propagation in the heart.

In this chapter, we will introduce the governing equations of the electrophysiology model in Section 5.1. The computational implementation of the monodomain model will be described in Section 5.2. Finally, a description of the multiphysics code Alya, employed on the simulations of this Thesis is done in Section 5.3.

5.1 Governing equations

Different approximations have been proposed for cardiac electrophysiology models, such as monodomain or bidomain equations. But, the simplification into monodomain formulation is perhaps the most common one [58, 67, 72, 30].

To better understand the monodomain model, first we will present the mathematical development for bidomain formulation and subsequently present the monodomain simplification. Both models describe the electrical propagation on the heart form a tissue scale.

At a cellular scale, the action potential propagation is a discrete process [43]. The propagation occurs form one myocyte to the neighbouring one through gap junctions (see Chapter 1). For larger scales, such as tissue scale, the propagation seems to be smooth [25]. For cardiac electrophysiology models, the action potential propagation is considered as continuous. This is a first and general assumption for modelling cardiac electrophysiology [21]. Bidomain model describing the propagation in the myocardium can be derived from the classical cable theory for electricity current along the neurones [89].

The continuous propagation is considered *quasi-static* electric field [66]. Considering a *quasi-static* electric field $\mathbf{E}$, the Maxwell-Faraday's equation ($\nabla \times \mathbf{E} = -\frac{\partial \mathbf{B}}{\partial t}$) becomes

$$\nabla \times \mathbf{E} = 0. \tag{5.1}$$

The electric field defined by $\mathbf{E} = -\nabla \phi - \frac{\partial \mathbf{A}}{\partial t}$, where u is the electric potential and $\mathbf{A}$ is the magnetic vector defined that determines the magnetic field $\mathbf{B} = \nabla \times \mathbf{A}$. So, the electric field $\mathbf{E}$ can be rewritten as the gradient of the potential u:

$$\mathbf{E} = -\nabla u \tag{5.2}$$

An extended version of Ohm's law related the current density $\mathbf{J}$ with electric field $\mathbf{E}$ and the conductivity tensor $\mathbf{G}$:

$$\mathbf{J} = \mathbf{G}\mathbf{E} = -\mathbf{G}\nabla u. \tag{5.3}$$

Bidomain model The intracellular and extracellular spaces defined two different domains, divided by the transmembrane, and characterized by its conductivities: $\mathbf{G}_i$ and $\mathbf{G}_e$, respectively. The first formulation of bidomain model was proposed by Tung in 1978 [97].

The bidomain equations are derived by applying conservation of charge between the intra- and extracellular domains. Considering equation (5.3), we have:

$$\begin{aligned} \mathbf{J}_i &= -\mathbf{G}_i \nabla u_i, \\ \mathbf{J}_e &= -\mathbf{G}_e \nabla u_e, \end{aligned} \tag{5.4}$$

where $\mathbf{J}_i$ and $\mathbf{J}_e$ are the intra- and extracellular current densities and u_i and u_e are the electrical potential for intra- and extracellular domains. It is assumed that exists a conservation of current and charge, so we can say:

$$\begin{aligned} &\nabla \cdot \mathbf{J}_i + \nabla \cdot \mathbf{J}_e = 0 \\ &\nabla \cdot \mathbf{J}_i = -I_m \\ &\nabla \cdot \mathbf{J}_e = +I_m \end{aligned} \tag{5.5}$$

where I_m is the transmembrane current per unit volume.

The transmembrane potential is defined as the difference between intra- and extracellular potentials: $\phi = u_i - u_e$. The amount of charge q separated by the cell membrane is related with the trasmembrane potential and the membrane capacitance (C_m):

$$\phi = \frac{q}{S_v C_m}, \tag{5.6}$$

where the charge $q = \frac{q_i - q_e}{2}$ depends on the intra- and extracellular charges, q_i and q_e, and S_v is the surface to volume ratio. From the derivative of equation (5.6) and taken into account the charge balance $\frac{\partial q_i + q_e}{\partial t} = 0$, we obtain:

$$\frac{\partial q_i}{\partial t} = S_v C_m \frac{\partial \phi}{\partial t}.$$

The transmembrane current I_m is composed by the capacitance component depending on the rate of charge accumulation ($\frac{\partial q}{\partial t}$) and by the ionic term I$_{ion}$. That is,

$$I_m = S_v \left(C_m \frac{\partial \phi}{\partial t} + I_{ion} \right) \tag{5.7}$$

Combining this last equation with (5.4) and (5.5) we obtain the bidomain model for cardiac tissue:

$$\begin{aligned} \nabla \cdot \mathbf{G}_i \left(\nabla \phi \ + \nabla u_e \right) &= S_v \left(C_m \frac{\partial \phi}{\partial t} + I_{ion} \right) \\ \nabla \cdot \left(\left(\mathbf{G}_i + \mathbf{G}_e \right) \nabla u_e \right) &= -\nabla \cdot \left(\mathbf{G}_i \nabla \phi \right). \end{aligned} \tag{5.8}$$

Monodomain model A simplification of bidomain models is done by the monodomain model by making the assumption that the intracellular and extracellular anisotropy is the same. As a consequence, monodomain models assume that the conductivity of extracellular and intra cellular regions are proportional.

$$\mathbf{G}_e = \lambda \mathbf{G}_i \qquad \forall \lambda \in \mathbb{R}.$$

Substituting $\mathbf{G}_e$ on the bidomain equations (5.8), the system of two equation can be reduced to one that only depends on $\mathbf{G}_i$:

$$\frac{\lambda}{1+\lambda} \nabla \cdot \mathbf{G}_i \nabla \phi = S_v \left(C_m \frac{\partial \phi}{\partial t} + I_{ion} \right). \tag{5.9}$$

The effective conductivity, or conductivity for monodomain model, is defined as $\mathbf{G} = \frac{\lambda}{1+\lambda} \mathbf{G}_i$. And replacing it on equation (5.9), we obtain the mathematical description for the monodomain model for cardiac tissue:

$$\nabla \cdot \mathbf{G} \nabla \phi = S_v \left(C_m \frac{\partial \phi}{\partial t} + I_{ion} \right) \tag{5.10}$$

The last equation can be rewritten using the Einstein notation[1]:

$$C_m \frac{\partial \boldsymbol{\phi}}{\partial t} + \frac{\partial}{\partial x_i} \left(\frac{G_{ij}}{S_v} \frac{\partial \boldsymbol{\phi}}{\partial x_j} \right) + I_{ion} \left(\boldsymbol{\phi} \right) = 0. \tag{5.11}$$

---

[1] Einstein notation is called the summation notation convention on repeated indexes.

The conductivity tensor G_{ij} is built from the transversally isotropic conductivity tensor G^d_{kl}. This diagonal tensor G^d_{kl} is locally aligned with the fibre for each material point in the domain. The anisotropic G_{ij} is built by rotating it to global system using the transformation matrix T_{ij} which is the local fibre's orthonormal system, defining one vector along the fibres and two transversal ones.

$$G_{ij} = T_{ik}\, G^{\mathrm{d}}_{kl}\, T^{-1}_{lj}$$

The diffusion tensor diffusion tensor ($\mathbf{D}$) is defined by a transformation of the D^d_{kl} diagonal diffusion tensor that locally describes the diffusion coefficients in each direction (fibre, normal and sheet plane).

$$D^d_{kl} = \begin{pmatrix} D_f & 0 & 0 \\ 0 & D_n & 0 \\ 0 & 0 & D_s \end{pmatrix} \qquad D_{ij} = M_{ik}\, D^{\mathrm{d}}_{kl}\, M^{-1}_{lj}$$

where D_f, D_n and D_s are the diffusion coefficients longitudinal to the fibres, normal to the fibres and in the sheet plane; and M_{ij} is the matrix transformation. Myocardium is a transversely isotropic material, that is, the material properties are different in the main direction, longitudinal to fibres, and the transverse direction, perpendicular to fibres. In this type of materials, the diffusion and the conductivity tensor are related as describe in text equation:

$$D_{ij} = \frac{G_{ij}}{S_v C_m}. \tag{5.12}$$

So, the equation (5.11) describing the monodomain model for cardiac tissue can be rewritten as:

$$\frac{\partial \phi}{\partial t} + \frac{\partial}{\partial x_i}\left(D_{ij}\frac{\partial \phi}{\partial x_j}\right) + \frac{I_{ion}}{C_m}(\phi) = 0. \tag{5.13}$$

The monodomain model was the one chosen for our simulation. The computing cost of this formulation is smaller than in bidomain models [58, 67, 72, 30]. The implementation is described on the Section 5.2.

Boundary conditions Although the heart is not an isolated organ, we assume no electrical interaction on the boundaries. We consider that the heart is isolated to the tissue that is around it. In consequence the condition set on the boundary Γ is:

$$\Gamma : \quad \mathbf{n} \cdot (\mathbf{G}\nabla\phi) = 0, \tag{5.14}$$

where $\mathbf{n}$ is boundary normal. If we establish our equation depending on diffusion as in equation (5.13), the boundary conditions are defined as:

$$\Gamma : \quad \mathbf{n} \cdot (\mathbf{D}\nabla\phi) = 0. \tag{5.15}$$

It is worth to remark that this is a natural Neumann condition in the Finite Element Method.

5.1.1 Ionic cell model

On the monodomain model description the term I_{ion} was introduced as a part of the transmembrane current. This term describes the transmembrane current density. It is defined by a function depending on the transmembrane potential ϕ, the time t and a set of parameters related to the ion currents of the cell.

This function I_{ion} is modelled by a set of ODE that continuously describe the cellular dynamics. From the simple models of Hodgkin-Huxley formulation where only Na+ current was modelled, models have became more complex both mathematically and computationally. In the last decade a huge number of phenomenological cell models had been proposed (in chronological order): [55, 13, 50, 26, 29, 91, 18, 61]. On those models the degree of physiological detail and mathematical and computational complexity varies, due to the number of currents, pumps and exchangers describing the cell dynamics included. The wave shape will depend on the model chosen.

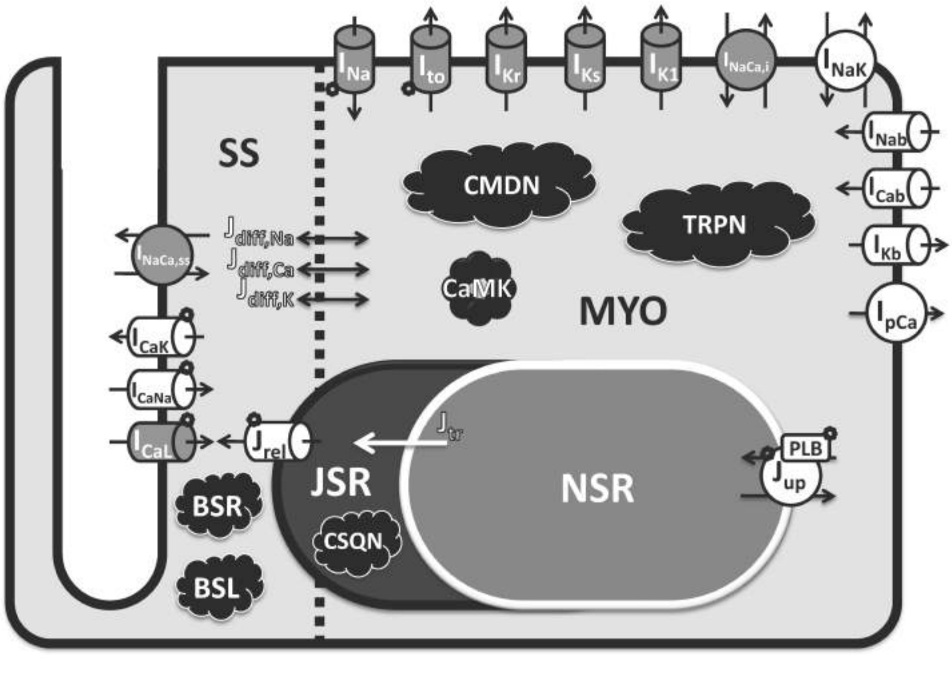

Figure 5.1: Governing equations. Cell dynamic scheme of the cell model proposed by O'Hara-Rudy. Image from [61].

The simulations included on this thesis used the O'hara-Rudy model [61], one of the most complete human cell models. The cell scheme in Figure 5.1 includes the main organelle implicated in the ion currents: the bulk myoplasm (MYO), the subspace near the T-tubules (SS), the junctional sarcoplasmic reticulum (JRS) and the network sarcoplasmic reticulum. The currents into myoplasm are: Na^+ current (I_{Na}) and the background currents (I_{Nab}, I_{Cab}); and outward the myoplasm are: transient outward K^+ current (I_{to}), rapid and slow rectifier K^+ current (I_{Kr}, I_{Ks}), inward rectifier K^+ current (I_{K1}), sarcolemmal Ca^{2+} pump current (I_{pCa}) and a background (I_{Kb}). The Na^+/K^+ pump current (I_{NaK}) and the 80% of the Na^+/Ca^{2+} exchange current are inward and outwards currents of the myoplasm. The other 20% of Na^+/Ca^{2+} exchange are inwards and outward current of the subspace SS, together with L-type Ca^{2+} current (I_{CaL} with components I_{CaNa} and I_{CaK}) into the subspace SS. Other intra cellular dynamics are also described on the Figure 5.1 that may affect the currents.

The used model includes ~ 50 equations that modulate 41 state variables in which there are included all the transmembrane currents and their different channels and exchangers (Figure 5.1). The authors used an ODE fitting technique to create this cell model.

This model is well accepted in the scientific community because it allows to model complex physiological, pathological and pharmacological problems [70, 102], and also it has been chosen by the Cardiac Safety Research Consortium [75], partially sponsored by the Food and Drug Administration (FDA), as the gold standard for electrophysiology modelling.

Pig model. The O'Hara-Rudy model is human based. The experimental measurements for the fitting model were taken from human samples. In the case simulations based on data form pigs, it is necessary to modify the O'Hara-Rudy model by eliminating the I_{to} current. This currents are not present in pigs. We assume that otherwise the dynamics are similar to the ones present in human myocytes.

5.2 Computational implementation

The numerical methods employed to solve the electrophysiology model, presented in Section 5.1, are described as follow. The continuum equation (5.10) can be rewritten as a system of ODE and PDE equations:

$$\begin{cases} \nabla \cdot \mathbf{D}\nabla\phi = \dfrac{\partial \phi}{\partial t} + \frac{1}{C_m} I_{ion}(\phi, p) \\ \dfrac{\partial p}{\partial t} = f(p, \phi, t) \\ \Gamma : \mathbf{n} \cdot (\mathbf{D} = 0) \end{cases} \tag{5.16}$$

where f is a system of ODEs describing the cell kinetics. The ion current function I_{ion} depends on the transmembrane potential ϕ and a set of parameters p, the solution or the ODEs system. In our simulations, the ODE system f was defined by the O'Hara-Rudy cell model proposed in [61]. The combination of PDE and ODE equations adds complexity to the system.

A Yanenko operator splitting technique was applied to discretize the system (5.16).

Following the Finite Elements Method, the linear diffusive terms can be integrated by parts. Once spatially and temporary discretized, the system (5.16) becomes:

$$\mathbf{M}\frac{\Delta\phi}{\Delta t} + \mathbf{K}\phi + I_{ion}(\phi, p) = 0. \tag{5.17}$$

where $\mathbf{M}$ is the mass matrix, $\mathbf{K}$ is the stiffness matrix and $\Delta\phi = \phi^{n+1} - \phi^n$ is the unknown difference between two time steps. The last equation can be rewritten as:

$$\left(\frac{\mathbf{M}}{\Delta t} + \theta \cdot \mathbf{K}\right)\Delta\boldsymbol{\phi} + \mathbf{M}\mathbf{I}_{ion} = -\mathbf{K}\boldsymbol{\phi}^n. \tag{5.18}$$

The scalar θ determines if the time integration scheme is Forward Euler (first order explicit, $\theta = 0$), Backward Euler (first order implicit, $\theta = 1$) or Crank-Nicolson (second order implicit, $\theta = 0.5$). On the ion current term $I_{ion}(\boldsymbol{\phi})$ close integration was applied to preserve the nodal character.

5.2.1 Solving strategy

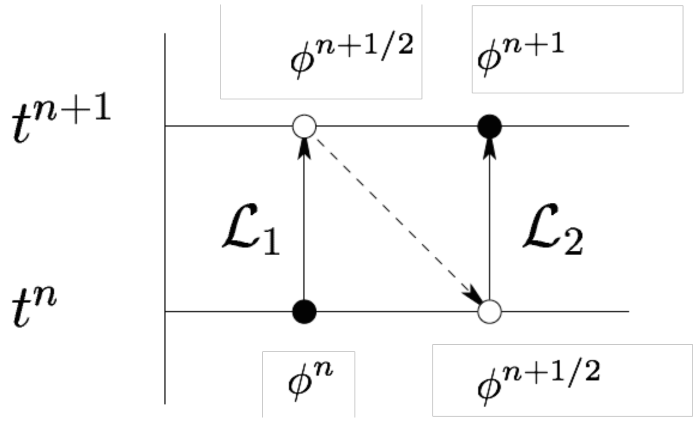

Figure 5.2: Computational implementation. Yanenko operatos splitting scheme.

As aforesaid, the discretized equations were solved using a first order Yanenko operator splitting (Figure 5.2). The steps followed are now described:

1. **Cell model:** The next ODEs system was solved using a Forward Euler explicit scheme for $t \in (t_n, t_{n+1/2})$:

$$\begin{cases} \frac{\Delta\phi^*}{\Delta t} + \mathbf{I}_{ion}(\phi, p, t) = 0 \\ \frac{\Delta p}{\Delta t} = f(p, \phi, t) \end{cases} \tag{5.19}$$

where $\Delta\phi^* = \phi^{n+1/2} - \phi^n$. We obtain the solutions ϕ and p at $t_{n+1/2}$, denoted as $\phi^{n+1/2}$ and $p^{n+1/2}$. This first step is represented as $\mathcal{L}_1$ operator in Figure 5.2.

2. **Tissue model:** A Backward Euler implicit scheme was use to solve the PDE for $t \in (t_{n+1/2}, t_{n+1})$:

$$\left(\frac{\mathbf{M}}{\Delta t} + \mathbf{K}\right) \Delta\tilde{\phi} = -\mathbf{K}\phi^{n+1/2} \tag{5.20}$$

where $\Delta\tilde{\phi} = \phi^{n+1} - \phi^{n+1/2}$. This second step is represented at Figure 5.2 as the operator $\mathcal{L}_2$.

3. **Update:** We obtain the updated ϕ^{n+1} from:

$$\phi^{n+1} = \phi^n + \Delta\phi^* + \Delta\tilde{\phi} \tag{5.21}$$

The cell model is solved explicit using a Forward Euler scheme and the tissue model is solved implicitly with either a Backward Euler or a Crank-Nicolson scheme. From numerical experiments we observed that the main limitation solving the electrophysiological model was the time limitation of the tissue model. The proposed combined scheme permits to simulate cardiac electrical propagation both efficient and accurate enough.

Computational implementation of electrophysiology model

$$\begin{aligned}
\textbf{Cell model}(\Delta\boldsymbol{\phi}^*):&\quad \frac{\Delta\boldsymbol{\phi}^*}{\Delta t} + \mathbf{I}_{ion}(\boldsymbol{\phi}) = 0\\
\textbf{Tissue model}(\Delta\tilde{\boldsymbol{\phi}}):&\quad \left(\frac{\mathbf{M}}{\Delta t} + \mathbf{K}\right)\Delta\tilde{\boldsymbol{\phi}} = -\mathbf{K}\boldsymbol{\phi}^*, \text{ where } \Delta\boldsymbol{\phi}^* = \boldsymbol{\phi}^* - \boldsymbol{\phi}^n\\
\textbf{Update}(\boldsymbol{\phi}^{n+1}):&\quad \boldsymbol{\phi}^{n+1} = \boldsymbol{\phi}^n + \Delta\boldsymbol{\phi}^* + \Delta\tilde{\boldsymbol{\phi}}.
\end{aligned}$$

5.3 Alya

The simulations on this Thesis were run in Alya, a code developed at Barcelona Supercomputing Center. It is designed and optimized of large-scale computers. The monodomain model for electrophysiology problem is implemented on Alya as described in Section 5.2.

This software is written in Fortran 90/95 and designed to run efficiently in high performance computers, with a tested scalability up to 100.000 cores [35, 100, 101, 19]. The structure of the code is done by modules, with a kernel in charge of the generic subroutines, solvers and parallelization. In each module a physical problem model is implemented, such as excitable media (electrophysiology), solid mechanics or compressible and incompressible fluids. The code is able to solve efficiently multiphysics problems using finite element method in parallel.

As cardiac simulations are computational problems are potentially large, the parallelization is the key to be able to run complex problem. In Alya, the problem domain Ω is partitioned using METIS [41] into several sub-domains Ω^1, Ω^2, Ω^3. Each sub-domain is distributed to a MPI [54] parallel threads.

Chapter 6

Simulation scenario from experimental data

A simulation scenario has to be defined to run the cardiac computational simulation. In the case of finite element methods, a geometry discretization is needed. In addition, for electrophysiological simulations, fibre orientation has to be included as a vector field on the model. In this chapter, we will explain how to obtain an adequate simulation scenario based on the experimental medical data processed in Part I of the thesis.

First of all, the ventricles geometry is discretized to build the computational mesh (Section 6.1). Then, the fibre orientation is incorporated to the mesh (Section 6.2). Two methodologies are proposed, one based on the fibre description given by experimental data from DTI, and the other one based on a rule-based mathematical model which describe synthetic fibres, commonly used when DTI data is not available. Both fibre orientations are incorporated to the mesh to perform a sensitivity analysis of electrophysiological model to fibres orientation. This analysis will be presented in Chapter 7. The electrical pacing activation maps are analysed to identify the pacing point and define the conduction velocity of the wavefronts (Section 6.4). Finally, we summarized the steps to perform a computational experiment based on experimental data.

6.1 Geometry discretization

Magnetic resonance imaging is an imaging tool able to provide the structural description of the heart through segmentation. Biventricular segmentations were performed as described in Chapter 3. The segmented post-contrast *ex vivo* CMR sequences were reconstructed from three dimensional surfaces describing the geometry of the ventricles. Afterwards the volumetric mesh was created from the biventricular geometry surfaces (Figure 6.1).

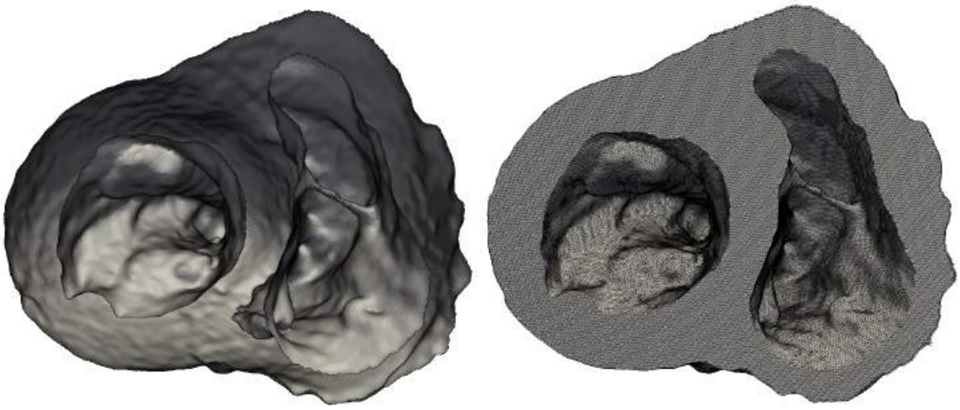

Figure 6.1: Geometry discretization. In the left, a biventricular geometry description and, in the right, the corresponding spatial discretization.

The mesh was obtained using the in-house code, MOH (Mesh by Octree Hierarchy). This code is based in isosurface stuffing [46]. An unstructured tetrahedral mesh was generated. This type of element can be easily adapted to complex geometries, such as ventricles. The electrophysiological models require a element size constrained to an element size under $\sim 500\mu$m [58]. For meshes with large elements, a mesh division technique [34] was employed to refine the meshes. This is also useful for example to analyse mesh convergence.

Mesh quality. To evaluate if the volume mesh computed is valid to run simulations, several mesh quality parameters were evaluated. Among others, we evaluated the element volume, shape and minimum dihedral angle [86, 45].

- The **volume** of all the elements composing the volume mesh were computed. The mesh must be uniform to assure an homogeneous depolarisation velocity. In addition, an homogeneous mesh makes can be subdivide if it is necessary to assess mesh convergence.
- The **minimum dihedral angle** α of a tetrahedra element is defined as the minimum of the dihedral angles of two adjacent faces of the tetrahedron. Given a edge $i \in 0, \cdots, 5$, the dihedral angle of two faces of a tetrahedron that are adjacent along the edge is:

  $$\alpha_i = \frac{180}{\pi} \arccos(\vec{n}_{i1}, \vec{n}_{i2}), \tag{6.1}$$

  where $\vec{n}_{i1}, \vec{n}_{i2}$ are unit vectors normal to the two tetrahedron faces that are adjacent to edge i. The angle α_i is measured in degrees. The minimum dihedral angle for each tetrahedron of the mesh is given by:

  $$\alpha = \min_{i \in 0, \cdots, 5} \alpha_i. \tag{6.2}$$

- The **shape** quality metric of an element $s \in [0, 1]$ is defined as:

$$s = \frac{3(J\sqrt{2})^{2/3}}{\frac{2}{3}\left(\vec{l}_0 \cdot \vec{l}_0 + \vec{l}_2 \cdot \vec{l}_2 + \vec{l}_3 \cdot \vec{l}_3\right) - \left(\vec{l}_0 \cdot (-\vec{l}_2) + \vec{l}_0 \cdot \vec{l}_3 - \vec{l}_2 \cdot \vec{l}_3\right)}, \quad (6.3)$$

  where $\vec{l}_0, \vec{l}_1, \vec{l}_2, \vec{l}_3$ are the vectors in the direction of the four edges. The Jacobian J of the element was defined as:

$$J = \left(\vec{l}_2 \times \vec{l}_0\right) \cdot \vec{l}_3. \quad (6.4)$$

  An acceptable value for the shape metric is between $[0.1, 1]$.

6.1.1 Mesh for controls

Both ventricles geometries from the control case were discretized. The resulting mesh was composed by 6.691.306 elements and 1.214.648 nodes.

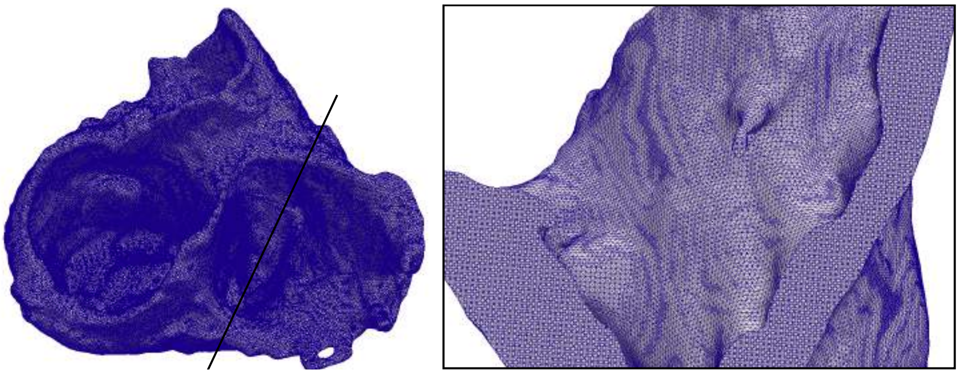

Figure 6.2: Geometry discretization. Control case volume mesh, including a slice view.

The mesh quality was measured by the element volume variability, the minimum dihedral angle of the elements and its shape. Also an approximation of the edge length of the elements was computed by supposing all the elements were regular tetrahedra.

Volume		**Approx. edge length**	
Average:	2.705×10^{-5}	Average:	612 μm
Minimum:	3.839×10^{-7}		
Maximum:	5.867×10^{-5}		

Dihedral angle		**Shape**	
Minimum:	7.84 deg	Minimum:	0.1941

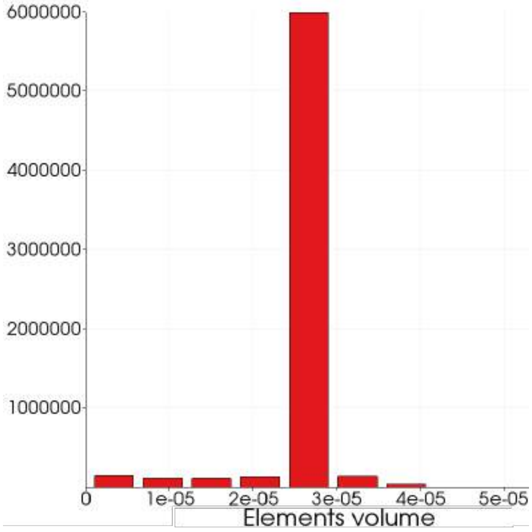

Figure 6.3: Geometry discretization. Histogram of the element volumes distribution in the control case mesh.

The volume distribution of the elements was almost homogeneous along the mesh. Moreover, the quality of the mesh was assured by the dihedral angle and the shape metric with good results. The minimum dihedral angle of the mesh was not close to 0 degrees. In the case of the shape, the minimum was over 0.1 and in addition, most of the elements were close to 1 (Figure 6.4). The averaged approximation of the edge length was larger than 500 μm, but it can be reduced if we refine the mesh by a divisor technique [34].

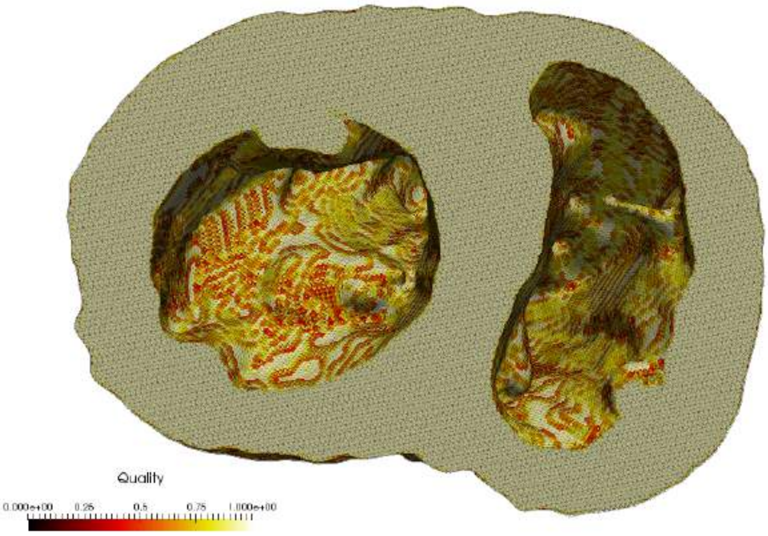

Figure 6.4: Geometry discretization. Element shape quality analysis of the control case mesh.

6.2 Fibre orientation

A fibre orientation description is required for electrophysiological simulations. Fibres determine the main direction of the electrical impulse propagation. Cardiac fibre description can be obtained from experimental data or using a mathematical model, when experimental data is not available. On simulations parametrized from *in vivo* data, generally the DTI is not available. As we described in Chapter 2, *in vivo* DTI is under development. This is the reason why mathematical fibre field description are very popular.

In this section, we describe how the fibres description is obtained from DTI and from Streeter rule-based model [88]. The resulting fibre orientation is incorporated to the computational mesh. Each node of the mesh will have associated the main direction vector describing the orientation of the fibre.

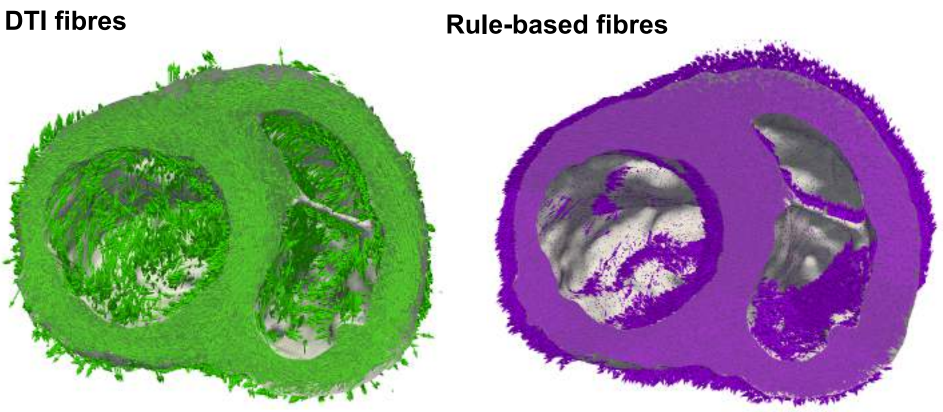

Figure 6.5: Fibre orientation. Main direction of fibres included on the compuational mesh. On the left, DTI fibre description; and on the right, rule-based fibre description.

6.2.1 DTI

An order two tensor is assigned to each voxel of DTI images, as described in Chapter 3. This tensor describes an ellipsoid. The principal long axis of the ellipsoids defines the main direction of the fibres. This information was extracted from the images using the DSIstudio software [107]. The main limitation of this technique is the resolution. The DTI acquisition resolution of our *ex vivo* sequences was 1.1 mm^3 isotropic, much coarse compared with the mesh discretization. A linear interpolation was needed to translate fibre description from DTI to all nodes of the mesh.

As a result, each of the node of the volume mesh had a vector describing the longitudinal direction of the fibre associated.

6.2.2 Rule-based model

Fibre orientation can also be defined mathematically using rule-based models. Several algorithms have been proposed to define the fibre field [87, 12, 24, 99]. These synthetic fibres are useful when DTI is not available, for example in clinical cases.

The methodology is based on finding the relative position for each node in the domain with respect to the endocardium and the epicardium and assigning a fibre direction. This model, based on the observation done by Streeter [88], will be now briefly described.

First, the minimal distance to endocardium (d_{endo}) and to epicardium (d_{epi}) are computed. Based on them, a thickness parameter e is defined as:

$$e = \frac{d_{endo}}{d_{endo} + d_{epi}}. \tag{6.5}$$

Fibres are built orthogonally to the local base generated , ensuring a smooth angle variation. The fibre orientation angle is determined by:

$$\alpha = \frac{\pi}{3}(1 - 2e)^n \tag{6.6}$$

where $n = 1$ determines a linear variation on the fibre orientation and $n = 3$ determines a cubic variation one (Figure 6.6). The maximum and the minimum angles for fibres were selected to be ±60° ($\pm\pi/3$).

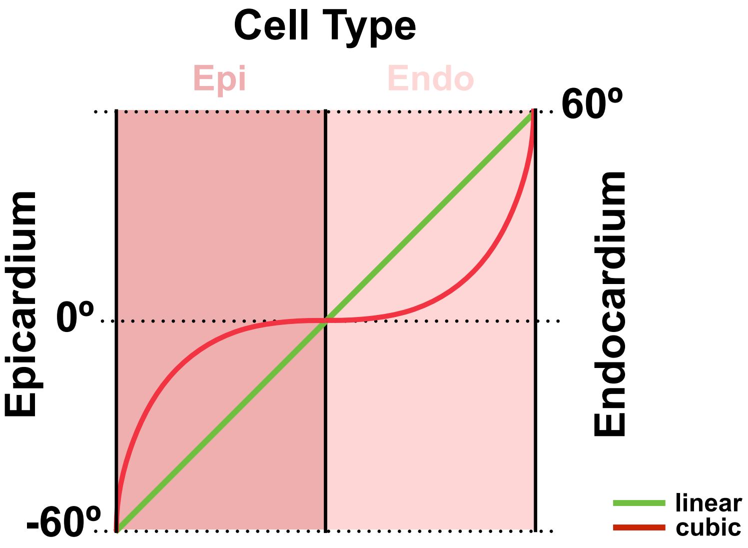

Figure 6.6: Fibre orientation. Angle for the fibre orientation on rule-bassed model porposed by [87]

.

The fibre orientation for LV and RV was obtained using the algorithm proposed in [67] in both cases. The distribution of RV fibres can be improved in future work including the implementation of [12, 24] in the algorithm.

6.3 Electrical characterization of the problem

During the experimental electrophysiological study, the activation maps were obtained (Chapter 2). These maps contain the time when the depolarization wave traverses each point of the ventricle wall surfaces. Activation maps of epicardium and LV and RV endocardium were obtained, during pacing. Moreover, to complete the electrical parametrization of the models, an approximation of the wave front velocity was computed from the activation maps. The pacing was done using a catheter screwed in the RV endocardium. Simulation results are compared against these maps in Chapter 7.

6.3.1 Pacing point location

We want to locate the pacing point location based on the information from the experimental activation maps. But, these maps have a lower resolution than the volume mesh. In addition, the geometry definition of the maps obtained during the electrophysiological experimental study is not accurate, as discussed in Chapter 3.

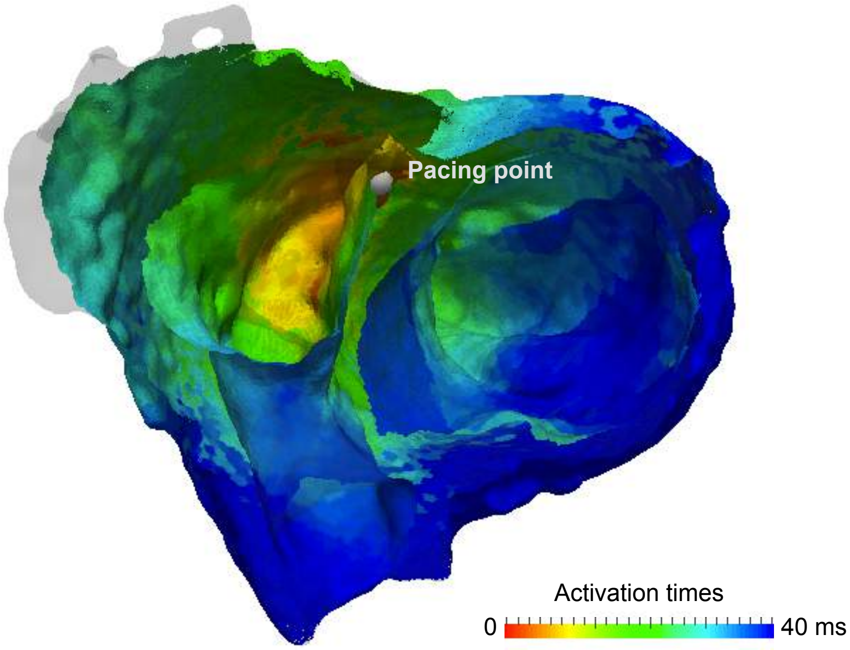

Figure 6.7: Electrical charazterization of the problem. Resgitered activatio points into the mesh and location the pacion point

As need to locate the pacing point on the volume mesh, the epicardial and RV endocardial activation maps needs to be in the same orientation and scale than the mesh. Through a combination of landmark registration and ICP method, the maps were registered into the the wall of the mesh. For further detail of the methodology employed on the registration refer to Chapter 3.

Once the maps were registered, the first activation point on RV was located. The coordinates of the closer node of the volume mesh were chosen to locate the impulse on the computational models. The first activated point in the epicardium was also identified and compared with the pacing point selected, to assure it was not an artefact.

6.3.2 Wave propagation velocity

Electrophysiological models require calibration before running the simulations. The wave velocity is one of the most important values that has to be incorporated in the model through diffusion parameters. Analysing the activation maps, we can extract information about the wavefront velocity during pacing.

The velocity of the wavefront $\vec{v}$ can be defined as spatial variation of the wave ds in a period of time dt, but this operation cannot be directly done from the experimental activation maps data. The direction of the wave is unknown on the maps, as a consequence the direction of the velocity cannot be identified. In a two dimensional example (Figure 6.8), the apparent velocity in the axis direction is $\vec{v}_x = \frac{dx}{dt}$ in the x direction and $\vec{v}_z = \frac{dz}{dt}$ in the z direction, while the real velocity $\vec{v} = \frac{ds}{dt}$. Both apparent velocities $\vec{v}_x$ and $\vec{v}_z$ always exceed the wavefront speed $\vec{v}$.

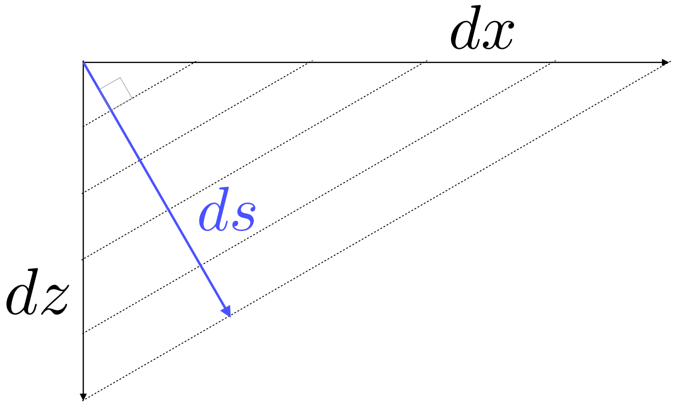

Figure 6.8: Electrical charazterization of the problem. Wavefront scheme representing the spatial variation on the direction of the wave, ds, and on the axis direction dx, dz.

In an ordinary wave propagation, energy propagates perpendicularly to the wavefront (Figure 6.8). The slowness vector $\vec{w}$ is defined as a vector perpendicular to the wavefront with a magnitude inverse to the velocity. In three dimensions, it is defined as:

$$w = \left(\frac{dt}{dx}, \frac{dt}{dy}, \frac{dt}{dz} \right) \tag{6.7}$$

The velocity vector was computed from the slowness vector as follows:

$$\vec{v} = \frac{\vec{w}}{\|\vec{w}\|^2} \tag{6.8}$$

The vector $\vec{v}$ describes the velocity of the wave front and it has the same direction as $\vec{w}$. The magnitude of both vectors is inverse. These can be easily verified:

$$\|v\| = \left\| \frac{w}{\|w\|^2} \right\| = \frac{\|w\|}{\|w\|^2} = \frac{1}{\|w\|}$$

The wavefront velocity of the activation maps was computed locally. The slowness vector and the velocity vector were computed in all the triangles composing the surfaces. The elements edges were considered as the local axis and barycentric coordinates were employed.

Slowness vector computation. The slowness vector was computed on all the triangular elements of the activation maps as follows.

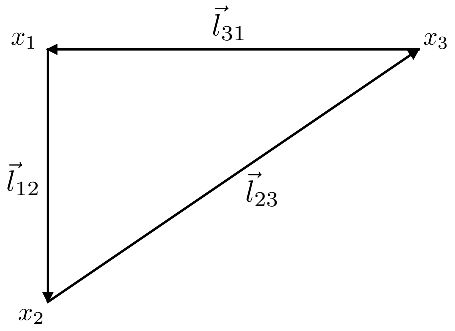

Figure 6.9: Electrical charazterization of the problem. Triangular element scheme.

Each element was composed by three vertices x_1, x_2, x_3 and three edges. The unitary vectors describing the directions of the triangle edges were calculated by:

$$\vec{r}_{12} = \frac{\vec{l}_{12}}{||\vec{l}_{12}||}, \quad \vec{r}_{23} = \frac{\vec{l}_{23}}{||\vec{l}_{23}||} \quad \text{and} \quad \vec{r}_{31} = \frac{\vec{l}_{31}}{||\vec{l}_{31}||},$$

where $\vec{l}_{ij} = \vec{x}_j - \vec{x}_i$ with $i, j = 1, 2, 3$. The $\vec{x}_i$ vectors described the coordinates of the element vertex. Inside the element, all points can be described by:

$$\vec{x} = \sum_{i=1}^{3} \lambda_i \vec{x}_i, \tag{6.9}$$

where λ_i are the barycentric coordinates of the points inside the triangle. The gradient of the barycentric coordinates of a given point $\vec{x}$ are:

$$\nabla\lambda_1(\vec{x}) = -\frac{l_{12} \cdot \vec{n}_1}{J}, \tag{6.10}$$

$$\nabla\lambda_2(\vec{x}) = -\frac{l_{23} \cdot \vec{n}_2}{J}, \tag{6.11}$$

$$\nabla\lambda_3(\vec{x}) = -\frac{l_{31} \cdot \vec{n}_3}{J}, \tag{6.12}$$

where J is the determinant of the Jacobian and $\vec{n}_i$ with $i = 1, 2, 3$ is the normal vectors to each edge. Using the Heron's formula the Jacobian of a triangular element can be easily computed based on the triangle area A, $J = 2 \cdot A$. The normals $\vec{n}_i$ with $i = 1, 2, 3$ were computed as:

$$\vec{n}_i = \vec{r}_i \times \vec{n}$$

where $\vec{n} = \vec{r}_1 \times \vec{r}_2$.

Finally, the slowness vector was computed as:

$$w_1 = t_3 \cdot \nabla\lambda_1(\vec{x}) \tag{6.13}$$

$$w_2 = t_1 \cdot \nabla\lambda_2(\vec{x}) \tag{6.14}$$

$$w_3 = t_2 \cdot \nabla\lambda_3(\vec{x}) \tag{6.15}$$

where t_i is activation time of the wave in the node i of the triangular element with barycentric coordinates $\lambda_1, \lambda_2, \lambda_3$. The sum of the 3 vectors w_i with $i = 1, 2, 3$ defined the slowness vector of the triangle $w = w_1 + w_2 + w_3$.

Experimental wavefront velocity The described procedure was applied on the activation maps to obtain an approximated value of the wavefront velocity. The velocities obtained were not homogeneous along the surface(Figure 6.10).

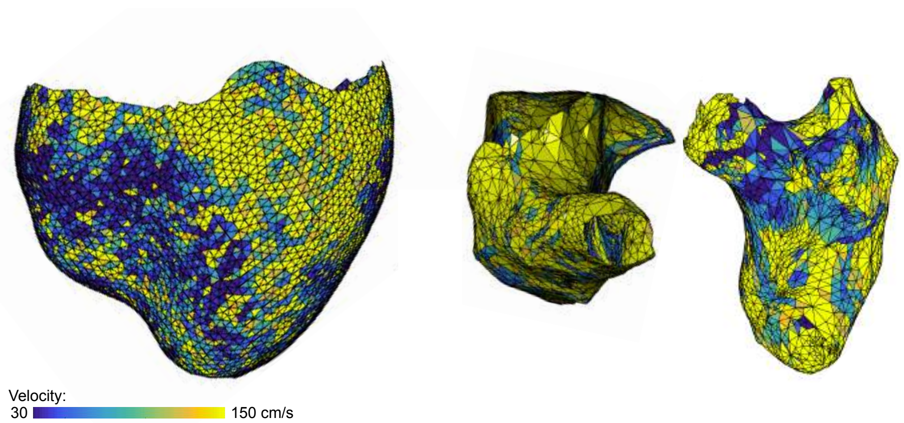

Figure 6.10: Electrical charazterization of the problem. Form left to right, epicardial RV endocardial and LV endocardial surfaces including the local wavefront velocity of each surface element.

Differences in local wavefront velocity can be found depending on the area of the surface evaluated (Figure 6.10). In median, the endocardial surfaces of the control case had a higher velocity than the epicardial surface, as shown in the next table:

Table 6.1: Wavefront velocity from activation maps of control during pacing.

	Median [cm/s]	**Interquartile range** [cm/s]
LV endocardium	119.855	(69.428, 238.845)
RV endocardium	152.795	(91.166, 248.634)
Epicardium	69.289	(34.836, 139.768)

Changes in the local velocity were also found within regions of each surfaces. In the case of epicardium, areas corresponding to RV epicardium were slower that the ones on LV epicardium. Differences on the velocity can be due to the limitations on the mapping techniques, such as noise in the acquisition data or differences when capturing voltage in a concave or a convex surface. Local differences can also be associated to the anisotropy of the fibres. It can also be hypothesized that involvement of the conduction system could be associated to differences on the electrical propagation. On the next chapter we will discuss the differences between the experimental wavefront velocity against computational results.

6.4 Computational electrophysiology experiments methodology

The first step was to build the simulation scenario. The spatial discretization of the biventricular geometry was needed. Given the *ex* *vivo* CMR segmentations, we computed a unstructured volume mesh with an homogeneous element distribution and fine enough to run electrophysiological models. Then, the fibre orientation was incorporated as a nodal vector field describing the longitudinal direction of the fibre. This fibre orientation was extracted from DTI or computed by a rule-based model.

The boundary condition for electrophysiological models is a zero flux condition along the boundaries. But, in this thesis we wanted to reproduce the cardiac behaviour during pacing, so a stimulus was imposed in the pacing point. The boundary condition for electrophysiological models during pacing were set as no influx with the boundaries all over the mesh, except the pacing point placed in the RV endocardium. To define the point, the experimental activation maps of the RV endocardium were registered on the volume mesh. In the first point activated on the registered map a current of -80 mV was set during 0.0002 s. This current started the depolarization wave.

The next step was to parametrise the models. A large amount of parameters are related with the electrophysiological models. A cell simulation was run Matlab using the O'Hara-Rudy model and imposing a cycle length of 400 ms. The initial ionic current to parametrize the tissue simulations in Alya were obtained from this cell simulation ran in Matlab, once the steady state was achieved at $\sim$ 1000 beats.

A sensitivity analysis of the model to the diffusion parameter was performed before running the biventricular simulations. This analysis aim to relate the diffusion coefficient with the propagation velocity of the wavefront. The parametrization was done taking into account this analysis and the wavefront velocity extracted from the experimental activation maps.

We have focused the main objective of the computational experiments in analysis how fibre orientation affects to the patterns of the wave propagations. One of the control cases from the experimental data processed in the first part of the thesis was selected. The control case was simulated as explained in Chapter 7 and the results were compared against experimental electrical data. The control simulation aims to perform describe the first steps toward an accurate validation of the electrophysiology model.

Chapter 7

Computational simulations results

In this chapter the computational electrophysiology experiments will be presented. We will present the results of the simple numerical verification test of the electrophysiological model in Section 7.1. The correct implementation of the model will be tested through an n-version verification to compare the results against solutions given by other published codes [58]. The test will be adapted to pig tissue properties and a sensitivity analysis of the diffusion parameter will be performed for the pig model in Section 7.2. Finally, a electrophysiological biventricular simulations of a healthy control case will be presented in Section7.3 and compared against experimental data. It will be also included a comparison between simulations including DTI and rule-based fibre descriptions.

7.1 Electrophysiological model verification

Numerical verification is essential to know if the model is correctly implemented in our code. For electrophysiological models, the main verification test was published by Niederer et al [58].

Mesh convergence of electrophysiological models was evaluated by multiple codes with the N-version verification test proposed in [58]. We have replicated the test, using the same geometry, boundary conditions and mesh, but using the O'Hara-Rudy cell model [61]. Results were compared against the presented in the cited publication.

Problem definition. The slab described in Figure 7.1 was employed to create the computational mesh. A mesh division technique [34] was employed to refine the grid and perform a mesh convergence test. On the refinement, each tetrahedral element of the original mesh ir divided into eight subtetrahedrons. When the mesh was refined ones we denote the new mesh by div1. In the case that the refinement algorithm was applied two or three times, the resulting meshes were denoted by div2 or div3, respectively. We employed a monodomain O'hara-Rudy cell model instead of the original the ten-Tusscher [91] model used in the test. A sensitivity analysis of the model to the spatial and the time discretization was performed.

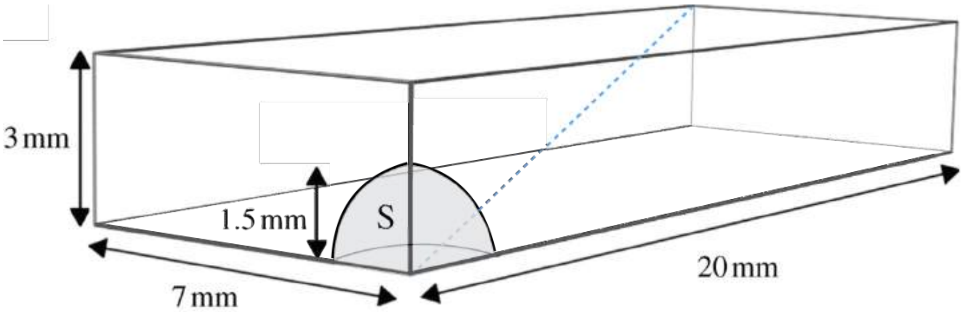

Figure 7.1: Electrophysiological model verification. Scheme of the simulation domain. The stimulus applied was in the partial sphere S. Modified from [58].

Longitudinal fibre orientation was defined in the long axis of the slab direction. All boundaries had zero-flux condition. An stimulus of -50 mV was imposed during 2 ms on the slab corner of point $(0, 0, 0)$ for the O'Hara-Ruddy model. A cycle length of 857 ms was imposed and the diffusion longitudinal and transversal were defined as 0.0009529 and 0.000125757 (cm^2/s), respectively. The cell model initial variables are described in Table 7.1.

Table 7.1: Cell model variables

Membrane potential	-85.23 mV	L-type Ca current d gate	3.373×10^{-5}
Rapid K current X_{r1} gate	0.00621	L-type Ca current f gate	0.7888
Rapid K current X_{r2} gate	0.4712	L-type Ca current f2 gate	0.9755
Slow K current X_s gate	0.0095	L-type Ca current fCass gate	0.9953
Fast Na current m gate	0.00172	Transient outward current s gate	0.999998
Fast Na current h gate	0.7444	Transient outward current s gate	2.42×10^{-8}
Fast Na current j gate	0.7045	Ryanodine receptor R_{prime}	0.9073
Sarcoplasmatic reticulum Ca	3.64 mM	Intracellular Ca	0.000126 mM
Intracellular Na	8.604 mM	Subspace Ca	0.00036 mM
Intracellular K	136.89 mM		

The electrical depolarization velocity was measured along the major diagonal of the slab, from the stimulation corner to the opposite one (Figure 7.1). Plotting the activation time as a function of the distance on the diagonal, shows a curve which has a slope equal to the inverse of the propagation velocity.

The time discretizations employed on the analysis were $\Delta t = 0.05$, 0.01 and 0.005 ms. In the case of spatial discretization, for each Δt several Δx

were evaluated as described in Table 7.2.

Table 7.2: Element characteristics of the meshes

	Elements	**Volume** [cm^3]	**Edge length range** [cm]
Original mesh	20664	2.032×10^{-5}	(0.05, 0.07)
div1	165312	2.540×10^{-6}	(0.025, 0.035)
div2	1322496	3.176×10^{-7}	(0.0125, 0.0175)
div3	10579968	3.970×10^{-8}	(0.00625, 0.00875)

Mesh convergence. The mesh convergence analysis was performed using a time discretization of $\Delta t = 0.05$ ms. The activation time is plotted as a function of the distance along the mentioned diagonal (Figure 7.2).

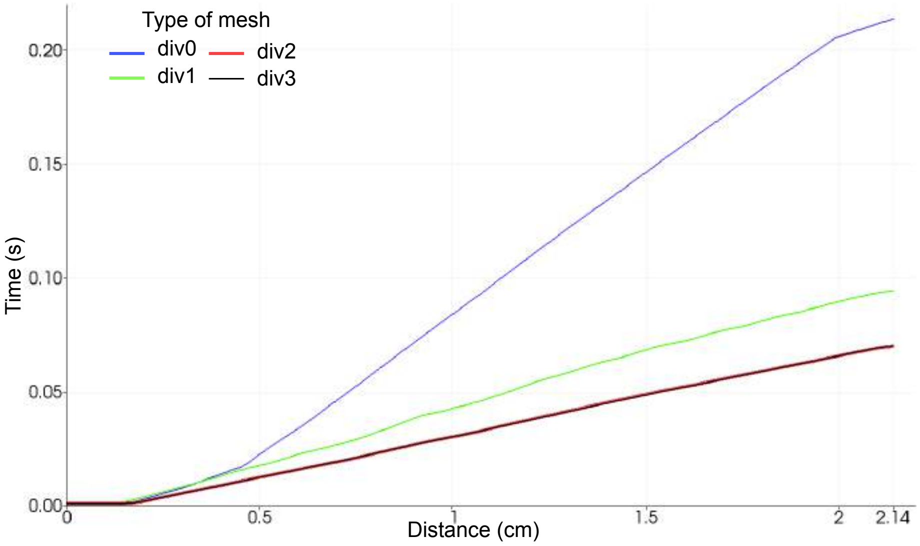

Figure 7.2: Electrophysiological model verification. Activation time against distance to the origin on the main dianagonal. A time discratization of $\Delta t = 0.05$ s and Δx defined by the refinements (div1, div2, div3) applied to the original mesh (div0). The curves corresponding to div2 and div3 were coincident.

The results are comparable to those presented in [58]. In meshes with larger elements, the wave velocity is slower. If we refine the mesh, the curves showed on Figure 7.2 converge. Moreover, the curves from simulations using div2 and div3 meshes are almost identical and the activation patterns are also similar (Figure 7.3). The corresponding to simulations on the meshes where divisor was applied 2 and 3 time are almost identical. The corresponding wavefront velocities are 26.936 cm/s and 27.262 cm/s, for div2 and div3 respectively (Table 7.3). This means that for volumetric elements equal or smaller than 3.176×10^{-7} the results were converged at $\Delta t = 0.05$. The electrical depolarisation patterns are equal for elements smaller than this value (Figure 7.3).

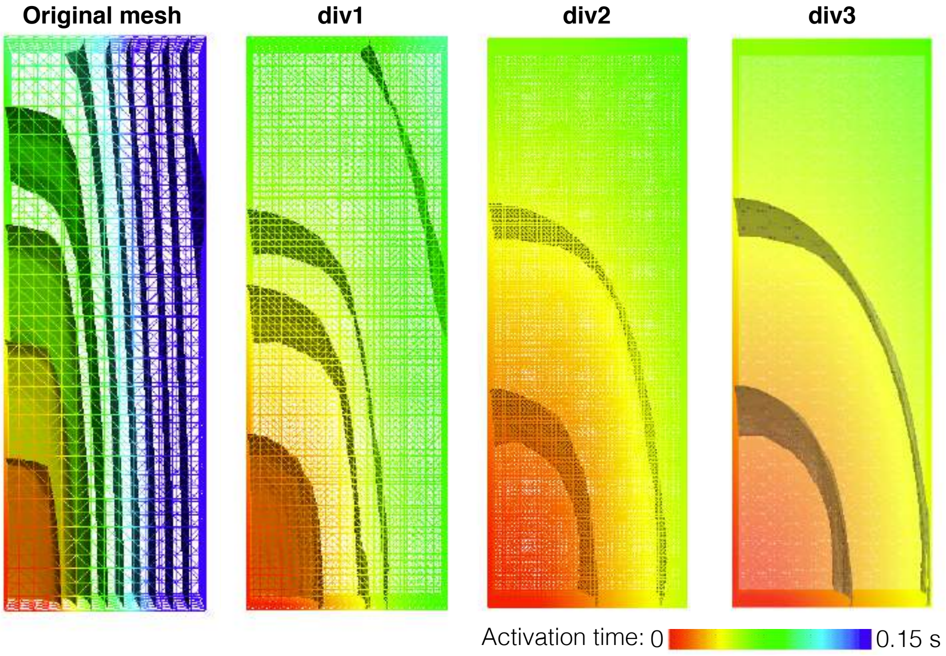

Figure 7.3: Electrophysiological model verification. Activation time of the four simulations of the original mesh and one (div1), two (div2) or three times (div3) refined, the isochrones or the activation times are ploted every 0.02 s.

Time convergence. We have run the simulations employed at three different time discretizations of the meshes and refinements described above up div2, where mesh was converged. The variations on the time step size Δt did not substantially affect to the velocity conduction.

Table 7.3: Conduction velocity depending on element size and Δ_t.

	$\Delta_t = 0.05$ms	$\Delta_t = 0.01$ms	$\Delta_t = 0.005$ms
Original mesh	8.0465	8.014	8.034
div1	19.630	19.330	19.209
div2	26.9367	26.626	26.364

7.2 Sensitivity analysis to diffusion

The electrophysiological models depend on several parameters, which include diffusion, that cannot directly be extracted from experimental data. The diffusion tensor **D** was defined in Chapter 5 as a 3×3 diagonal matrix. Values on the diagonal correspond to the fibres longitudinal, normal and sheet plane diffusion. We considered a transversely isotropic material medium and we assumed that the normal and sheet plane diffusion were the same. We define a longitudinal fibres diffusion D_l and a transversal to fibres diffusion D_t. Therefore we built the diffusion tensor $\mathbf{D}$ of the model as:

$$\mathbf{D} = \begin{pmatrix} D_l & 0 & 0 \\ 0 & D_t & 0 \\ 0 & 0 & D_t \end{pmatrix}$$

The diffusion is related to the depolarization wave velocity. We aim to describe how variations in the diffusion affect the propagation velocity. To do so, we have performed a sensitivity analysis of the model to the diffusion parameters and after we have quantified the velocity changes. The objective is to be able to approximate diffusion values based on the depolarization velocity given by the activation maps. The description about how extract the velocity from the experimental data was described in Chapter 6.

Problem definition. The slab, employed on the test verification in Section 7.1, was also chosen to perform the diffusion sensitivity analysis. We imposed a uniform time discretization of $\Delta t = 0.05$ ms and several spatial discretization Δx were evaluated refining the mesh.

The cell model employed was an adaptation of the O'Hara-Rudy model for of pig tissue. The main difference on the swine model was the elimination of the transient outward K^+ current (I_{to}), in pigs this currents is inexistent. To define the cell model initial variables at the desirable cycle length of 400 ms, a cell simulation was previously run in Matlab. The O'Hara-Ruddy without I_{to} was employed to run the cell simulation where a stimulus was imposed every 400 ms and the cell model was run up to a steady state, $\sim$ 1000 ms. The resulting cell currents were saved and incorporated to the tissue simulations as initial variables. We made the assumption that there was a cellular homogeneity and all the cells were considered as endocardial cells.

On the slab simulation the cycle length was defined at 400 ms, the same as on the experimental electrophysiological procedure described in Chapter 1. The diffusion D_l and D_t were set to 0.001171 and 0.00039033, respectively [18].

First, a mesh convergence was performed. We have evaluated the wave velocity in the diagonal v_d, longitudinal v_l and transversal v_t direction. The velocities along the slab diagonal were calculated as in the verification test described in Section 7.1. The propagation velocity along the longitudinal fibre direction coincides with the long direction of the slab and defines the maximum propagation velocity. In the case of the tranversal direction, it is coincident with the velocity in the direction the small edges of the slab and defines the minimum propagation velocity. The maxim and the minimum propagation velocities were calculated by plotting the activation time along the longitudinal and transversal fibre direction, respectively.

The velocities calculated on the mesh convergence analysis of this problems are summarized in Table 7.4.

Table 7.4: Velocities along the slab diagonal and the longitudinal and transversal direction to fibres to evaluate mesh convergence.

	Edge length [cm]		**Velocity**	[cm/s]
		$\mathbf{v_d}$	$\mathbf{v_l}$	$\mathbf{v_t}$
Original mesh	(0.05, 0.07)	21.569	23.310	9.488
div1	(0.025, 0.035)	27.582	29.070	15.014
div2	(0.0125, 0.175)	32.537	34.247	19.967
div3	(0.00625, 0.00875)	34.187	36.900	22.284

Diffusion sensitivity test. Taking as a reference the velocities summarized in Table 7.4, the simulations were run using different values of the diffusion. The references values for D_l and D_t were the ones employed on the mesh convergence performed during the problem definition of this section. This reference diffusion were multiplied by a range of values from 1 to 20 times in the slab simulations for the sensitivity test. Three spatial discretizations were employed for each diffusion set.

The results from the different simulations are summarized in Table 7.5 and Figure 7.4. The longitudinal and transverse propagation velocities obtained on meshes where the divisor was applied once or twice were comparable. Also, it was observed that the ratio between the longitudinal and transversal velocities was approximately 2 in all cases.

Table 7.5: Wave velocity of different diffusions

Diffusion (D_l, D_t)	**Original mesh**	**div1** (v_l, v_t)	**div2** (v_l, v_t)
×1	9,488, 23.310	15.014, 29.070	19.967, 34.246
×2.5	18.533, 42,508	26.258, 50.891	33.240, 56.497
×5	28.571, 65.146	39.933, 76.046	80.645, 46.377
×7.5	37.037, 83.507	50.000, 94.340	55.299, 98.039
×10	44.486, 98.765	58.968, 111.111	64.603, 112.359
×12.5	54.115, 118.3432	68.866, 129.870	73.733, 131.579
×15	60.530, 131.147	76.677, 140.845	79.867, 142.857
×17.5	66.667, 143.369	83.333, 153.846	87.114, 156.250
×20	71.429, 153.846	87.114, 162.602	91.255 166.667

The curves in Figure 7.4 describe how the velocities in the fibre direction and transversal to it change with the diffusion coefficients. Results showed that the model is very sensitive to diffusion coefficients, so it has to be taken into account when parametrizing the simulations. To achieve bigger conduction velocities, the coefficient must be increased.

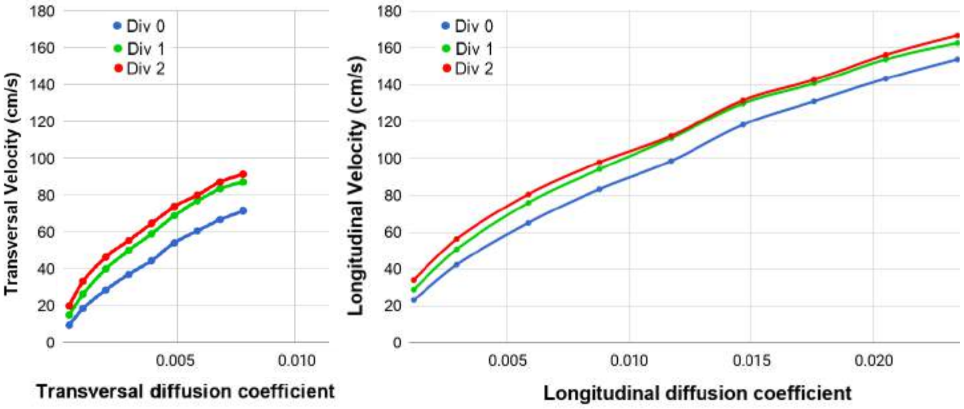

Figure 7.4: Senstitivity analysis to diffusion. Tranversal and longitudinal velocities changes with the tranverse and longitudindal diffusion coefficient respectively.

We have describe how propagation velocity change with the diffusion coeficient for a paraticular cell model parametrizations. The main application of this achivement is that if we know a priori the depolarization velocity desirable for our computational model, we can employ the curves in Figure 7.4 to approximate the diffusion parameters required to run electrophysiological simulations. This is useful to reduce the parametrization process on complex geometries that run under the same cell model conditions as the described above.

7.3 Control case

The biventricular electrophysiological simulations were run to evaluate its power when reproducing the beat of a healthy heart. The results were compared against experimental data from a control subject. The computational scenario was build based on the experimental data of one of the control cases analysed in the first part of the thesis.

In general, cardiac electrophysiological simulation must include a Purkinje activation system in the model. However, the experimental scenario that we want to simulate includes pacing, so the electrical activation begins in the catheter tissue interface. As a consequence, and assuming that Purkinje network cannot be retrogradely activated by the pacing stimulus, we can neglect the Purkinje network for our simulation during pacing.

The cell model properties were equal to the ones imposed on the diffusion sensitivity analysis in the slab (Section 7.2). Based on mentioned diffusion analysis, the following diffusion coefficients were chosen: 0.0231858 cm^2/s for the longitudinal diffusion and 0.007728534 cm^2/s for the longitudinal diffusion to obtain the desirable propagation velocity.

The computational mesh, built from segmented CMR on Chapter 6, had an average element volume of 2.7055×10^{-5} cm^3. This element size is comparable with the one of the original slab mesh (2.032×10^{-5} cm^3). To ensure that the simulation results are accurate, we applied the divisor once. The refinement technique was used to obtain a 53.530.448 elements mesh with an averaged elements volume of 3.3819×10^{-6} cm^3, similar to element volume of the div1, slab mesh (2.540×10^{-6} cm^2).

The following simulations were run on the refined mesh composed by 53 millions of elements. On this mesh, 10000 times steps were needed to run simulation of 500 ms in 196 cores, with a total calculation time of 30 minutes.

In this section we have first performed two type of simulations: one including DTI fibre orientation and another including synthetic fibre orientation described by a mathematical rule-based model. Both simulations were compared against the activation maps from the experimental protocol. The main objective was to evaluate the power of simulations when reproducing the beats of a healthy heart and describe the sensitivity of the model to the fibre distribution. Then, we have introduced two types of cells, endocardial and epicadial cells, on the model with DTI fibre orientation. We have evaluated the action potential in both types of cells and we have performed a S1-S2 protocol to calculate the electrical restitution curves and compare them against the experimental ones. The main objective was to evaluate the cell model and compare it with the experimental data and build a reference case for future parametrization of the cell properties on the model.

7.3.1 Numerical and experimental description of a beat

A cardiac beat starting with a external stimulus on a point in the RV endocardium was described by computational models including different fibre orientations (DTI and synthetic) and by the experimental activation maps. The time activations discribed the moent in which the activation wave pass through each point of the myocardium. The activation times, its gradients and the wavefront propagation velocity were calculated and compared. This comparisons between experimental and numerical data were done to analyse the accuracy of the computational models, as a first step towards validation of computational models.

Total activation time on simulation including DTI fibres is similar to experimental data and larger than simulation with synthetic fibres. The total activation time on the two computational models are different. The one resulting from the simulation including DTI fibres is 83.85 ms and 105.55 s in the case of simulation including rule-based fibres. In the case of the experimental activation maps of the control case have a total activation time of 71.9 ms, closer to the one of the simulation including

DTI.

Moreover, the differences between the experimental and numerical, including DTI fibre orientation, total activation time are mostly due to the basal geometry. At the total activation time for experimental DTI data, on 71 ms, the epicardium is almost completely activated in the simulation (Figure 7.5). The areas of the computational model that last more to be activated, remarked in grey in the figure, are due to geometrical details that only appear on the computational model, built from *ex vivo* CMR segmentation. As we discuss on the first part of the thesis, the accuracy of the *ex vivo* CMR imaging tool is larger than electrophysiological experimental studies, such as activation maps.

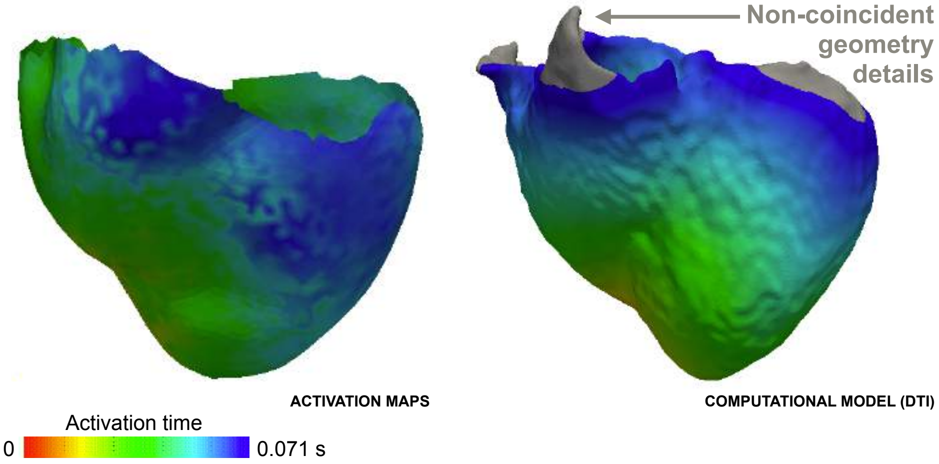

Figure 7.5: Control case. Epicardial activatiom map geometry and the simulation including DTI fibres. For a local activation time of 0.071 s, the differences on the simulation case were due to geometrical details.

The fact that the depolarization is slower in simulation including rule-based fibres instead of DTI fibres is related with the different activation patterns of both simulation (Figure 7.5).

Activation patterns from the computational model including DTI agree with the experimental data. The activation patterns were described by the isochrones of the activation maps (Figure 7.5).

The simulated wavefront patterns, in the case including DTI fibres, are similar to the ones from the experimental activation maps (Figure 7.5). In both cases, we observe that isochrones are parallel to the base on the RV epicardium and endocardium (anterior view) and dramatically descend to the base on the LV. This pattern is not observed in the case of the simulation including rule-based fibres in which isochrones are parallel to the base in the epicaridal and endocardial surfaces.

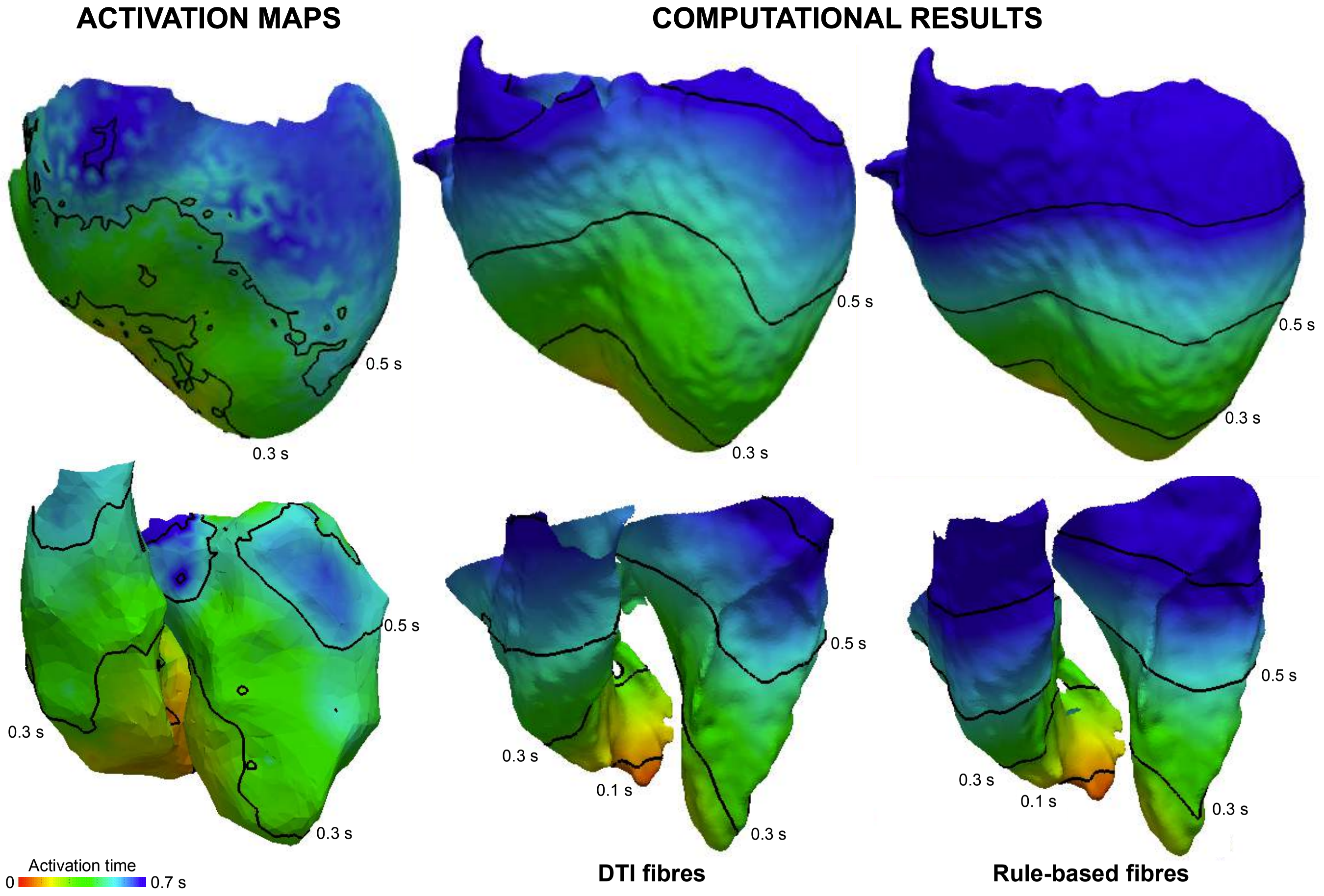

Figure 7.6: Control case. Activation maps including isochrones of the epicardium and the endocardium from experimental and simulation data.

The gradients of the activation times vary between LV and RV epicardium. The differences on the shape of the wavefront were characterized by the activation time gradients. These gradients are clearly different between the RV and LV epicardium, as shown in Figure 7.7.

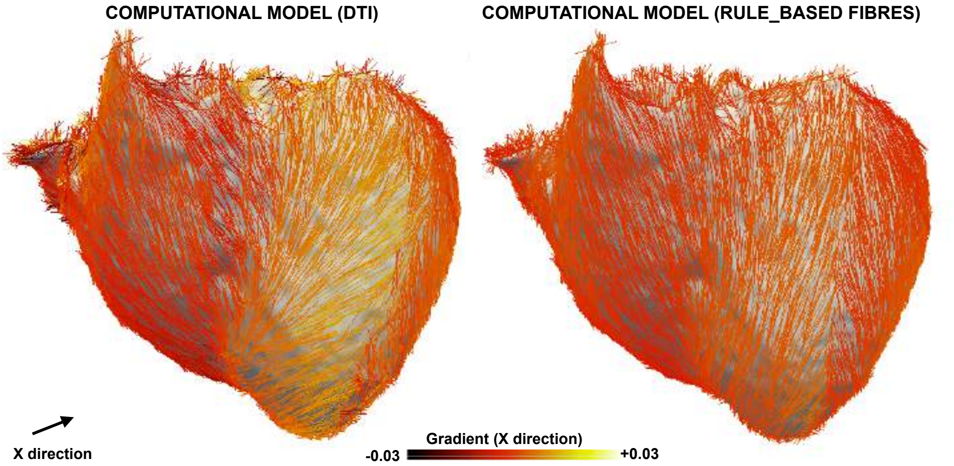

Figure 7.7: Control case. Gradient of the activation time field of simulation including DTI and synthetic fibres. The colour code correspond to the X direction of the gradients.

If we compare the gradients from simulation results against the gradients of the experimental activation maps (Figure 7.8), it is difficult to extract any conclusion as the experimental data was more noisy. The activation maps were affected by the movement of the heart and technical limitations during the experimental procedure.

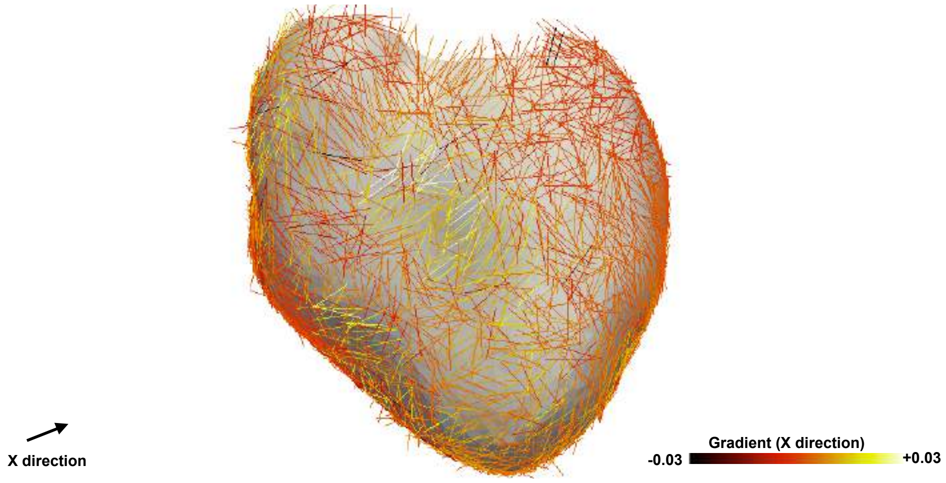

Figure 7.8: Control case. Gradient of the activation time from experimental data. The color code correspond to the X direction of the gradients.

Despite the noise, looking in detail the gradients of the experimental data, we can observe that gradients on epicardial region have different behaviours in LV and RV. This was coherent with the observed behaviour on the simulations including DTI, but the noise is too large to affirm there is a real correlation.

Endocardial wavefront velocities are well reproduced. The propagation velocity of the wavefront was computed as described in Chapter 6. The median experimental propagation velocities are: 69.289 cm/s (epicardium), 119.855 cm/s (LV endocardium) and 152.795 cm/s (RV endocardium).

The same algorithm was applied to the activation maps from electrophysiological simulations. We obtained that the median velocity for the simulations including DTI fibres were 116.870 cm/s in the endocardium and 137.94 cm/s in the epicardium. Similar velocities were found in the simulations including synthetic fibres. The median propagation velocity was 100.94 in the endocardium and 116.018 in the epicardium.

It is remarkable that the propagation wavefront is faster in the endocardium for experimental data and on the epicardium for computational models. Although this, velocities in the LV endocardium from experimental data and from simulations including DTI fibres were very close.

7.3.2 S1-S2 protocol to compare experimental and simulated restitution curves

The control model including DTI fibres was the one that better reproduce the wave propagation of the healthy control case. We aim to provide more detailed comparison taking into account the action potential that the model is able to reproduce.

Cell heterogeneity was included on the model to have more detailed description of the endocardial and epicardial cell models and analyse its action potential. The cell differentiation was done by the middle layer of the myocardium.

A S1-S2 protocol was run and its results were compared to the ones form the S1-S2 experimental protocol performed in the electrophysiological animal study. Experimental and simulated restitution curves describing the cell recovery after a S2 stimulus were computed.

The action potential shape on the endocardial coincides with on the epicardial cells due to electronic coupling. In one cell simulation the shape of the action potential is different in epicardial an endocardial cells [61]. The heart is simulations are done from a tissue level, so the action potentials of endocardial and epicardial cells are affected by the cellular electronic coupling (Figure 7.9). The two sample action potentials shown are almost identical with a delay due to the activation time differences. The wave activated first the selected point on the endocardium and then the epicardial point chosen.

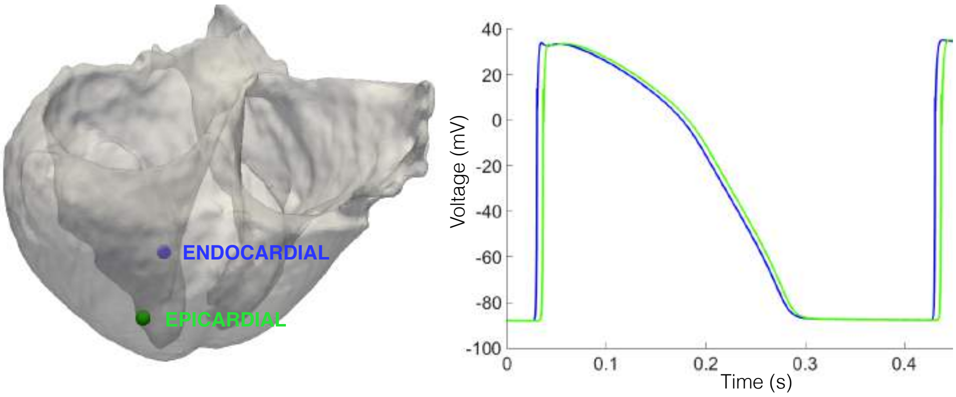

Figure 7.9: Control case. Action potential of one endocardial point and one epicardial point represented on the biventricular mesh, in the right.

As a consequence, none relevant different was found between the ventricular simulations including just endocardial cell and those including epicardial and endocardial cells. Neither it was in the case of the total activation time of both simulations.

The restitution curves from experimental data and from simulations have similar slopes. The S1-S2 protocol included 10 continuous S1 stimulus every 400 ms and a S2 stimulus at 340 ms, in the animal experiments. The same protocol was repeated changing the S2 stimulus, that was decreased up to refractory period where cell is not ready to for a second stimulus. This protocol was adapted for simulations (Figure 7.10).

Three S1 stimulus every 400 ms were imposed in the computational model. The second stimulus S2 was also 340 ms. This simulation was repeated for each different S2 stimulus that was decreasing from 340 ms by 10 ms step up to refractory period (Figure 7.10).

The restitution curves were fitted from the point obtained on the S1-S2 protocol. These curves are describe the APD recovery after S2 stimulus as a function of the previous DI (Figure 7.10). The restitution curves obtained from the experimental and simulated S1-S2 protocols ar showed in Figure 7.11.

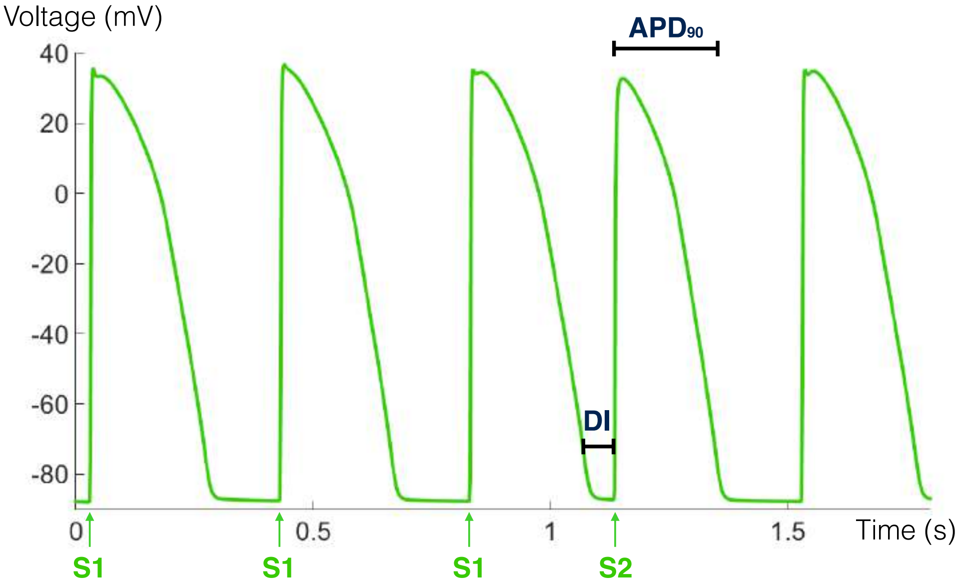

Figure 7.10: Control case. Simulated S1-S2 protocol of a epicardial cell. Three S1 stimulus were imposed every 400 ms and a S2 stimulus was imposed at 300 ms.

The restitution curves were the solution of a fitting to logarithmic function of the experimental and numerical data obtained on the S1-S2 protocols (Figure 7.11). In the case of the endocardial cell, the curves were: $y = 108.66 + 14.18 \cdot \log x$ for the experimental data and $y = 155.34 + 14.08 \cdot \log x$ for the numerical data. The fitted restitution curves form epicardial cells were defined by: $y = 67.69 + 23.09 \cdot \log x$ for the experimental data and $y = 153.89 + 14.18 \cdot \log x$ for the numerical results. The restitution curves of a endocardial and a epicardial cell from simulations are almost identical.

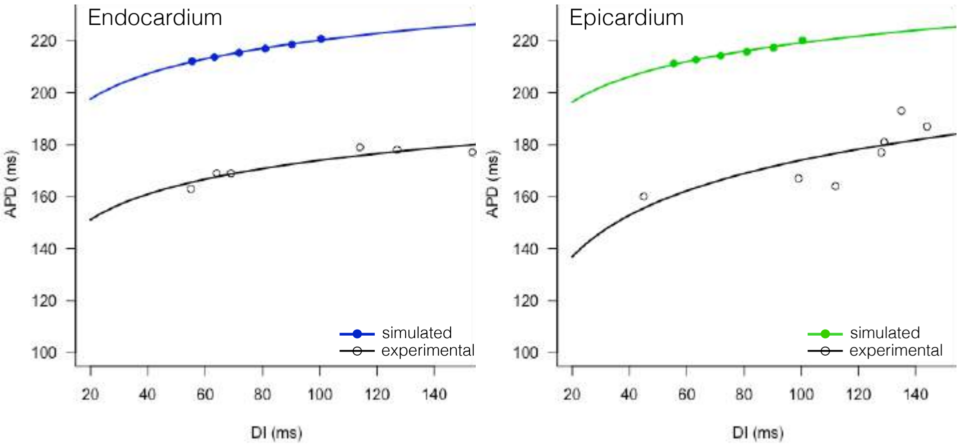

Figure 7.11: Control case. Restitution curve from experimental and simulatated S1-S2 protocols in endoacardial and epicardial cells.

The maximum slope of the restitution curve fitted from a experimental endocardial point 0.7063 is almost identical to the one from simulations 0.7018 (Figure 7.11). More differences were found on the case of epicardial cells where the maximum slope was 1.1503 in the experimental data and 0.7066 in the simulated one (Figure 7.11).

The difference between curves can be related with many factors. Ones related to the limitations of the experimental procedure, signal obtained with the catheter had an intrinsic error, and the heart is moving during the procedure. Other factors are related with the cell model parametrization. We haver employed the model proposed by O'Hara-Rudy for human cell with the unique adaptation of eliminating the I_{to} current. A detailed parametrization of the model employing optimization technique to find the adequate cell parametrization will be the next of the study in the close future.

7.4 Main conclusions of computational electrophysiology experiments

The major funding of the cardiac simulation computational experiments are summarized in this section. The discussion of these results, as well as the limitations of the computational study will be described in Chapter 8. Here, we enumerate the main computational results:

1. **The implementation of the electrophysiological model is verified against published results.**
2. **Electrophysiological models are highly sensitive to the diffusion coefficients.**
3. **Fibre orientation affects the cardiac simulations.**
4. **Electrophysiological simulation including DTI fibre reproduce well the behaviour of the healthy heart during pacing.**
5. **The total activation time is smaller in simulations including DTI fibre orientation compared with rule-based fibre orientation.**
6. **The activation time gradients varies between LV and RV epicardium.**
7. **The propagation velocity measured in the epicardial wall is similar in experiment and numerical results.**
8. **The action potential shapes of simulated endocardial and epicardial cells coincide due to the electronic coupling.**

9. **The restitution curves from experimental data and from simulations have similar slopes.**

Chapter 8

Discussion, limitations and future work

In this chapter, the main conclusions of the thesis are presented in Section 8.1 and summarized in Section 8.3. The limitations of the study are described in Section 8.2. Some of the main work lines that are followed in the future are presented in Section 8.4. Finally, the publications derived from this thesis will be summarized in Section 8.5.

8.1 Discussion

Scar characterization. The experimental study design allowed the characterization of the MI substrate located in both ventricles. The scar defined on voltage maps, obtained using conventional mapping/ablation catheters, matched with the surface scar projections from CMR at the subendocardial or subepicardial layer of 1 mm from the wall: A difference of a $\sim 5\%$ was found on the normalized surface scar area among techniques using this optimal thickness layer for CMR scar projection.

Voltage mapping provided an average information of $\sim$ 1 mm deep of the mapped regions. These maps failed to identify surviving endocardial tissue within low voltage areas defined as scar, even though they were identified as healthy tissue by high-resolution *ex vivo* CMR. Therefore, we have detected a resolution limitation on the voltage maps from EAM for detailed substrate characterization. This issue could be solved by increasing the mapping resolution using multipolar catheters with smaller electrodes, which reduces the voltage-derived scar areas and identifies more surviving region within very low voltage areas [90, 95].

The *in vivo* CE-CMR sequences showed larger volume scar tissue in comparison to *ex vivo* high-resolution post-contrast CMR. It may be due to partial volume effects that affect *in vivo* lower resolution images especially in thinner walls [79]. This showed that state-of-the-art *in vivo* post-contrast CMR sequences [5] have limitations to identify healthy tissue within heterogeneous or dense scar. However, since the distance projection chosen, 1 mm, it was close to the *in vivo* CMR acquisition resolution, these differences between *in vivo* and *ex vivo* scar from CMR were reduced after the projection onto the ventricular surfaces.

For both *ex vivo* and *in vivo* post-contrast CMR, there is still a lack of a gold standard methodology to segment the scar [6, 90, 4]. We performed a highly precise and time-consuming (∼24-48 h) manual refinement of the ventricular myocardial segmentations. On the resulting ventricle segmentation, we characterized the signal intensity thresholdings from *in vivo* and *ex vivo* sequences to get optimum threshold to obtain accurate classifications of the types of tissue: healthy, heterogeneous and dense scar.

In addition, the cardiac segmentations performed in this thesis were also employed to study the differences between DTI parameters in healthy and scar tissue in the work [31].

The obtained scar characterization results allows us to describe the technical limitations that may affect clinical interpretation of the data.

Ventricular arrhythmia inducibility. The LVEF is the most used marker of VT risk. The analysis described in [31] on the same experimental data set as the employed in this thesis showed that there was not any statistically difference on LVEF from only VF inducible or VT inducible animals. This result could be biased due to the limited number of samples ($n = 15$), but it is in concordance with reported clinical studies [38, 78, 22, 27].

Dense and heterogeneous scar volumes from *in vivo* and *ex vivo* post-contrast CMR did not differentiate among groups of animals. Despite the low number of cases of our study ($n = 12$), the results are in concordance with the fact that CMR is not incorporated to clinical guidelines for arrhythmia risk stratification and VT characterization after MI yet [38]. Moreover, they are supported by a previous clinical study where the scar volume did not show statistical significant differences on VT features of patients with and without VT recurrences [2]. However, two small clinical series reported that 12-to-13 VT beats cycle length correlated with scar extension [3, 105]. Also, another study reported in which heterogeneous scar correlates with sustained monomorphic ventricular tachycardia (SMVT) inducibility after programmed ventricular stimulation [78]. But, we have to take into account that the acquisition resolution of the CMR sequences in the last mentioned study was 1.5×2.4 mm with 8-mm slice thickness, a big limitation according to the differences found in our scar characterization study between isotropic resolution of 1.5 mm^3 and 0.6 mm^3.

In addition, a study complementary to this thesis [31] has analysed the role of fibre orientation inside our segmented scar from *ex vivo* CMR in ventricular arrhythmias.

Computational models. In this thesis we have tried to follow a path of Verification, Validation and Uncertainty Quantification (VVUQ) for computational electrophysiology.

Verification was achieved by reproducing the N-version test published in [58]. Thanks to a set of controlled experiments of unprecedented quality, we have carried on the first, but solid steps to achieve validation by analysing a control. We acknowledge that the analysis presented here is based more on qualitative than quantitative comparisons, but we are carrying out a deeper assessment with the same data and simulations results. Finally, we have attempted to measure uncertainty on input parameters through a systematic swept on diffusion coefficients, fibre field definition, time steps, mesh sizes, etc. This analysis is done not only on the academic set-up but also on the large scale real geometries.

The parametrization of electrophysiological models involves the diffusion coefficient and the initial conditions of the cell model variables. The depolarization propagation velocity of the numerical results is highly dependent on the diffusion coefficients chosen. So, a sensitivity analysis was performed in order to quantify the uncertainty derived from the diffusion coefficients selection. Moreover, the longitudinal and transversal to fibre propagation velocities were described as a function of the diffusion coefficients. So that, under the same cell model parametrization and cycle length imposed, we can employ this function to set the diffusion coefficients corresponding to the desirable propagation velocity.

Two types of fibre orientations were incorporated to the model, based on experimental DTI and based on a rule-based models [88]. The results of this thesis showed that fibre orientation has been underestimated in computational models generally more focussed on the electrical properties differences assigned to each type of tissue.

The activation patterns in cardiac simulations for the healthy control case including DTI fibres were similar to the experimental measures from activation maps. We observe that this did not happened in the simulations including rule-based fibre orientations. Electrophysiological models are dependent on the fibre orientations. A previous study [99] described the variations on the propagation depending on the fibre orientations defined, but they did not compare their results against any experimental data of the electrical activity.

An algorithm, adapted from the geophysics field, was proposed to compute the wavefront propagation velocity. The median propagation velocity was similar on the endocardium for the experimental and of the numerical results, in the case of simulation including DTI fibre orientation. However, significant differences were found on the epicardial velocities.

In previous studies, the ventricle and scar reconstruction from CMR including substrate characterization has been used to generate computational models aiming at predicting arrhythmia risk or target areas during ventricular tachycardia ablation [10, 93], but no comparison against experimental activation maps was provided. In addition, in human VT simulation studies [23] the CMR acquisition resolution is the main constrain: $1.77 \times 1.77 \times 8$ mm^3. This resolution was much more coarse than our swine *in vivo* CMR study. In the scar characterization study performed in this thesis we found that low CMR resolution was related with inaccurate scar characterizations. This inaccurate scar definition affects to the computational models, since the electrophysiological properties are assigned to wrong healthy, dense scar or heterogeneous scar regions.

In this thesis we have defined adequately a tool to perform VT simulations in the close future. We have described a set of post-processing tools that were able to accurately describe the ventricles, the scar and the fibre orientation from experimental data. Moreover, we have verified and quantified the uncertainty of the diffusion coefficients on the electrophysiology model implemented in Alya. In addition, we have compared the experimental and simulated activation maps of a healthy heartbeat with good results.

8.2 Limitations

Scar characterization and VT inducibility study limitations

- The **small number of cases** makes difficult to generalized the conclusions. Moreover, they are based on animal experimental data obtained by a specific protocol. Changes on the protocol, such as CMR resolution or scar segmentation, could create variations on the results.

- **Fat areas** were mainly limited to the interventricular course of the LAD coronary artery in the pig model. Patients with structural heart disease present larger areas of epicardial fat [65]. CMR sequences using fat suppression or computed tomography studies can provide additional value to increase CMR-based substrate characterization in the epicardium.

- Although high-resolution *ex vivo* CMR studies provided detailed characterization of ventricular substrate after MI, the **resolution** could be still a limitation in areas with thinner myocardial walls, such as RV free wall or atria.

- Substrate segmentation of the post-contrast CMR is affected by signal intensity thresholding, which varies among series. Furthermore, there is a lack of uniform consensus on the gold standard methodology to classify the scar tissue [5, 4]. **Any change on the segmentation method could change the substrate characterization**.

- For further validation of the scar, **a histopathology study** could be performed, but was not done within this protocol.

- The arrhythmia study was done with VT and VF induced by a programmed stimulation study. **The study cannot be extrapolated for spontaneous arrhythmias**. In addition, alternative pacing sites could have induced change results of VT inducibility.

Computational electrophysiology study limitations

- The simulations were **not completely blinded to experimental data**, since we needed to parametrize some aspects such as the pacing point or the depolarization velocity.

- Comparisons against experimental data were only possible for activation. The **repolarization was not compared at all against experimental data yet**.

- The **DTI resolution** was lower than the volume mesh discretization. The fibre description from DTI was interpolated to the mesh nodes.

- The **pacing location was approximately selected** on the registered activation maps from experimental data.

- The **cell model parametrization** was based literature parameters for human cells, waiting for future optimizations based on the restitution curves.

- The model was not completely validated, we have just performed quantitative comparisons against some of the experimental data available.

- The experimental data employed to compare had noise related to the **limitations of the acquisition technique** and the movement of the heart.

8.3 Achievements of this thesis

The goals proposed in this thesis were achieved. We will summarise the major achievements of the thesis.

Multi-modal scar characterization. The scar was defined in EAM by the classical voltage thresholds. A new methodology based on FWHM method was proposed to find the optimum threshold for scar segmentation on a set of post-contrast *in vivo* CMR obtained with the same conditions. In addition, this methodology was adapted to post-contrast *ex vivo* CMR, R1 sequences, by incorporating a wall thickness criteria.

Limitations of *in vivo* clinical tools were described. The scar was well defined by the post-contrast *in vivo* CMR, but significant limitations were found to characterize the scar into dense and heterogeneous tissue. In addition, lower resolution images like *in vivo* CMR were affected more by partial volume effects. In the case of *in vivo* EAM, this technique did not detect the healthy regions within the scar. In both cases, the high-resolution reference was considered to be the *ex vivo* post contrast CMR.

Biventricular multi-modal comparison described a correct interpretation of the techniques. A biventricular multi-modal comparison was done between endocardial and epicardial surface scars from the three techniques. The comparison included the RV endocardium, which is really rare. A new methodology was proposed to project the CMR volume scar into the walls based on the Eikonal equation. The main advantage was that we did not predefine a subendoacardial layer, all the possible layers can be compared on the same scar projection map. The EAM scar described the average voltage that corresponds to a $\sim$ 1 mm subendocardial/subepicardial layer of the ventricles segmented from CMR.

Scar volume from either *ex vivo* or *in vivo* CMR segementation was not related with VT inducibility. The dense and the heterogeneous scar volumes were not significantly different in cases in which VT was induced and cases in which only VF was induced.

Verification and sensitivity to diffusion of the electrophysiology computational model. The implementation of the electrophysiology model employed to simulate the cardiac beat was verified by a test in a slab geometry. We also verified mesh convergence and the sensitivity to the temporal discretizations. Moreover, we evaluated the sensitivity of the model to the diffusion parameters. The relationship between the diffusion coefficients and the longitudinal and transversal to fibre propagation velocity was described.

Activation patterns on the simulated activation maps match with the patterns on the experimental activation maps. The cardiac simulations were compared against experimental activation maps performed during pacing. The simulations for the control case including DTI fibres reproduced well the patterns described in the experimental data.

The fibre orientation determines the activation patterns on cardiac simulations. The fibre orientation has a important role in cardiac simulation. Fibres from experimental DTI and fibres described by a rule based model determine different depolarization patterns in the control case simulations. The total activation time was larger in the case of simulations including rule-based fibres.

The restitution curves from experimental and simulations were similar. The S1S2 protocol was simulated and the restitution curves were calculated to quantified the recovery of the action potential to a S2 stimulus. The model was able to reproduce curves with similar slope than the experimental ones. However, the curves are not coincident. Improvements in the cell parametrization must be done to achieve the matching between experimental and simulated restitution curves.

8.4 Future work

This thesis opens a whole world of work to be done. Next studies for scar characterization should address the optimal resolutions during acquisition to achieve consistent and comparable results among series. In addition, a histopathology study should be done for further validation of the scar.

The computational models should incorporate a pseudo-ECG in the simulation protocol. The pseudo-ECG give extra information useful for validations of the computational model based on experimental data.

Fibre orientation from complex rule-based models [24] will be incorporated to go further in the sensitivity test. Finding a good synthetic model for fibres is key due to the limitations of the DTI acquisition in *in vivo* CMR sequences.

A parametrization based on restitution curves should be included to get accurate initial conditions for the cell model employed. On a small region of the computational mesh, we will investigate the optimal cell model parametrization by reproducing the S1S2 protocol changing the conductance values of the cell model using Dakota [1]. This code would select the optimal initial values for currents that best reproduce the S1S2 protocol in three points: one in RV endocardium, another in the LV endocardium and the last one in the epicardium.

The control simulation presented in this thesis will be a reference case in which the parametrization improvements described above should be incorporated. Once the optimum parametrization is achieved, we will move to the rest of control cases to evaluate the improvements and the accuracy of the models.

A complete campaign of electrophysiology simulations should be done to assess Alya, following a methodical strategy of VVUQ based on the experimental data obtained in CNIC and processed in this thesis. This will put Alya at the forefront of computational cardiac modelling.

The scar characterization performed in this thesis will be incorporated to computational models. We aim to evaluate the powerful of computational models when predicting VT. The post-infarction simulations should include different electrical properties in healthy and scar tissue, and they should incorporate the DTI fibre orientation description. Moreover, the simulations should be blinded to the VT inducibility information.

In addition, the fluid-electromechanical coupling could be included in the post-infarction case in order to study the interactions of the full multiphysics heart in a pathological state described from experimental data.

8.5 Scientific Work

In this section we summarize the scientific work done in this thesis[1].

Publications in peer-reviewed journals:

- Mariña López-Yunta, Daniel García-León, Jose-Manuel Alsonso-Alzamán, Manuel Marina-Breysse, Jorge G. Quinatnilla, Javier Sánchez-González, Carlos Galán-Arriola, Victoria Cañadas-Godoy, Daniel Enriquez-Vazquez, Carlos Torres, Borja Ibañez, Julián Pérez-Villacastín, Nicassio Pérez-Castellano, José Jalife, Mariano Vázquez, Jazmín Aguado-Sierra, and David Filgueiras-Rama. Implications of Imaging Approaches in Biventricular Substrate Characterization after Myocardial Infarction. European Heart Journal: Cardiovascular Imaging (submited).
- Daniel García-León, Mariña López-Yunta, Jose-Manuel Alsonso-Alzamán, Manuel Marina-Breysse, Jorge G. Quinatnilla, Javier Sánchez-González, Carlos Galán-Arriola, Borja Ibañez, Julián Pérez-Villacastín, Nicassio Pérez-Castellano, José Jalife, Mariano Vázquez, Jazmín Aguado-Sierra, and David Filgueiras-Rama. Cardiac fiber disorganization determines the arrhythmia risk and ventricular tachycardia features after myocardial infarction. (2018) Nature Communications. (submited).

- Santiago, A., Aguado-Sierra, J., Arís, R., Casoni, E., Lopez-Yunta, M., Rivero, M., Sacco, F., Houzeaux, G., Vazquez, M. Coupled fluid-electro-mechanical cardiac computational model for device testing applications. (2017). Frontiers in physiology. (in revision).
- Vázquez, M., Arís, R., Aguado-Sierra, J., Houzeaux, G., Santiago, A., López, M., Cajas, J. C. Alya Red CCM: HPC-Based Cardiac Computational Modelling. (2015). Selected Topics of Computational and Experimental Fluid Mechanics, 189. DOI: 10.1007/978-3-319-11487-3 11

---

[1] Updated list of publications in https://orcid.org/0000-0003-4986-8516 and https://scholar.google.es/citations?user=kri0GhUAAAAJ&hl=es&oi=ao

Conferences, seminars and workshop:

- **2018**

  - Multimodal charactization of post-infarct substrate of in vivo VT model. López-Yunta, M. CompBioMed & VHeart workshop.

- **2017**

  - Electrophysiological cardiac simulation scenmario from experimental medical data. Lopez-Yunta, M., Aguado-Sierra, J., Filgueiras, D., Vazquez, M. 23 rd Congress of the European Society of Biomechanics.

- **2016**

  - Modelo computacional cardiaco de 3 campos: sangre, electrofisiologia y tejido. Lopez-Yunta, M., Santiago, A., Aguado-Sierra, J., Cassoni, E., Houzeaux, G., Sacco. Congreso Anual de la Sociedad Española de Ingenieria Biomedica.

  - Electromechanical heart simulation based on MRI images. Lopez-Yunta, M. 4 Jordandes de Investigadors Predoctorals Interdisciplinaria.

- **2015**

  - Simulacion electromecanica del corazon basada en imagen de resonancia Lopez-Yunta, M., Santiago,A., Vazquez, M., Casoni,E., Aguado-Sierra, J, Rivero,M., Aris,R. V reunion del capitulo español de la Sociedad Europa de Biomecanica.

  - Generation of a simulation scenario from medical data: Carto and MRI. López-Yunta, M., Roca, X., Aguado-Sierra, J., Vázquez, M. BSC 2nd International Doctoral Symposium 2015.

  - A dimensionally heterogeneous coupled HPC cardiac-vascular model using a black box decomposition approach. A. Santiago, M. Vázquez, P. J. Blanco, G. Houzeaux, J. Aguado-Sierra, S. Watanabe, M. Lopez Yunta, M. Rivero. 1st Pan-American Congress on Computational Mechanics.

- **2014**

  - Fully-Coupled Electromechanical Simulations of the LV Dog Anatomy Using HPC: Model Testing and Verification. Aguado-Sierra, J., Santiago, A., Rivero, M.I., López-Yunta, M., Soto- Iglesias, D., Dux-Santoy, L., Camara, O., Vazquez, M. (2014). Statistical Atlases and Computational Models of the Heart - Imaging and Modelling Challenges. STACOM 2014. Lecture Notes in Computer Science, vol 8896. Springer. DOI:10.1007/978-3-319-14678-2 12

Bibliography

[1] Brian M Adams, Lara E Bauman, William J Bohnhoff, Keith R Dalbey, John P Eddy, Mohamed S Ebeida, Michael S Eldred, Patricia D Hough, Kenneth T Hu, John D Jakeman, et al. Dakota, a multilevel parallel object-oriented framework for design optimization, parameter estimation, uncertainty quantification, and sensitivity analysis: Version 5.4 user's manual.

[2] Sana M Al-Khatib, William G Stevenson, Michael J Ackerman, William J Bryant, David J Callans, Anne B Curtis, Barbara J Deal, Timm Dickfeld, Michael E Field, Gregg C Fonarow, et al. 2017 aha/acc/hrs guideline for management of patients with ventricular arrhythmias and the prevention of sudden cardiac death: A report of the american college of cardiology/american heart association task force on clinical practice guidelines and the heart rhythm society. *Journal of the American College of Cardiology*, page 24390, 2017.

[3] Joachim Alexandre, Eric Saloux, Alain Lebon, Audrey Emmanuelle Dugué, Adrien Lemaitre, Vincent Roule, Fabien Labombarda, Laure Champ-Rigot, Sophie Gomes, Arnaud Pellissier, et al. Scar extent as a predictive factor of ventricular tachycardia cycle length after myocardial infarction: implications for implantable cardioverter-defibrillator programming optimization. *Europace*, 16(2):220–226, 2013.

[4] Luciano C Amado, Bernhard L Gerber, Sandeep N Gupta, Dan W Rettmann, Gilberto Szarf, Robert Schock, Khurram Nasir, Dara L Kraitchman, and João AC Lima. Accurate and objective infarct sizing by contrast-enhanced magnetic resonance imaging in a canine myocardial infarction model. *Journal of the American College of Cardiology*, 44(12):2383–2389, 2004.

[5] David Andreu, Antonio Berruezo, José T Ortiz-Pérez, Etelvino Silva, Lluis Mont, Roger Borràs, Teresa María de Caralt, Rosario Jesús Perea, Juan Fernández-Armenta, Hrvojka Zeljko, et al. Integration of 3d electroanatomic maps and magnetic resonance

scar characterization into the navigation system to guide ventricular tachycardia ablationclinical perspective. *Circulation: Arrhythmia and Electrophysiology*, 4(5):674–683, 2011.

[6] David Andreu, Diego Penela, Juan Acosta, Juan Fernández-Armenta, Rosario J Perea, David Soto-Iglesias, Teresa M de Caralt, Jose T Ortiz-Perez, Susana Prat-González, Roger Borràs, et al. Cardiac magnetic resonance–aided scar dechanneling: influence on acute and long-term outcomes. *Heart rhythm*, 14(8):1121–1128, 2017.

[7] Elad Anter, Cory M Tschabrunn, Alfred E Buxton, and Mark E Josephson. High-resolution mapping of post-infarction reentrant ventricular tachycardia: electrophysiological characterization of the circuit. *Circulation*, pages CIRCULATIONAHA–116, 2016.

[8] Charles Antzelevitch. Basic mechanisms of reentrant arrhythmias. *Current opinion in cardiology*, 16(1):1–7, 2001.

[9] Ángel Arenal, Esther Pérez-David, Pablo Ávila, Javier Fernández-Portales, Verónica Crisóstomo, Claudia Báez, Javier Jiménez-Candil, José L Rubio-Guivernau, María J Ledesma-Carbayo, Gerard Loughlin, et al. Noninvasive identification of epicardial ventricular tachycardia substrate by magnetic resonance–based signal intensity mapping. *Heart Rhythm*, 11(8):1456–1464, 2014.

[10] Hermenegild Arevalo, Gernot Plank, Patrick Helm, Henry Halperin, and Natalia Trayanova. Tachycardia in post-infarction hearts: insights from 3d image-based ventricular models. *PloS one*, 8(7):e68872, 2013.

[11] Ruth Arís Sánchez. *Electromechanical large scale computational models of the ventricular myocardium.* PhD thesis, Universitat Politècnica de Catalunya.

[12] Jason D Bayer, Robert C Blake, Gernot Plank, and Natalia A Trayanova. A novel rule-based algorithm for assigning myocardial fiber orientation to computational heart models. *Annals of biomedical engineering*, 40(10):2243–2254, 2012.

[13] Go W Beeler and H Reuter. Reconstruction of the action potential of ventricular myocardial fibres. *The Journal of physiology*, 268(1):177–210, 1977.

[14] Olivier Bernus, Ronald Wilders, Christian W Zemlin, Henri Verschelde, and Alexander V Panfilov. A computationally efficient electrophysiological model of human ventricular cells. *American Journal of Physiology-Heart and Circulatory Physiology*, 282(6):H2296–H2308, 2002.

[15] Paul J Besl, Neil D McKay, et al. A method for registration of 3-d shapes. *IEEE Transactions on pattern analysis and machine intelligence*, 14(2):239–256, 1992.

[16] Frank M Bogun, Benoit Desjardins, Eric Good, Sanjaya Gupta, Thomas Crawford, Hakan Oral, Matthew Ebinger, Frank Pelosi, Aman Chugh, Krit Jongnarangsin, et al. Delayed-enhanced magnetic resonance imaging in nonischemic cardiomyopathy: utility for identifying the ventricular arrhythmia substrate. *Journal of the American College of Cardiology*, 53(13):1138–1145, 2009.

[17] Philipp Boyé, Hassan Abdel-Aty, Udo Zacharzowsky, Steffen Bohl, Carsten Schwenke, Rob J van der Geest, Rainer Dietz, Alexander Schirdewan, and Jeanette Schulz-Menger. Prediction of life-threatening arrhythmic events in patients with chronic myocardial infarction by contrast-enhanced cmr. *JACC: Cardiovascular Imaging*, 4(8):871–879, 2011.

[18] Alfonso Bueno-Orovio, Elizabeth M Cherry, and Flavio H Fenton. Minimal model for human ventricular action potentials in tissue. *Journal of theoretical biology*, 253(3):544–560, 2008.

[19] E Casoni, Antoine Jérusalem, Cristóbal Samaniego, Beatriz Eguzkitza, Pierre Lafortune, DD Tjahjanto, Xavier Sáez, Guillaume Houzeaux, and Mariano Vázquez. Alya: computational solid mechanics for supercomputers. *Archives of Computational Methods in Engineering*, 22(4):557–576, 2015.

[20] Radomir Chabiniok, Vicky Y Wang, Myrianthi Hadjicharalambous, Liya Asner, Jack Lee, Maxime Sermesant, Ellen Kuhl, Alistair A Young, Philippe Moireau, Martyn P Nash, et al. Multiphysics and multiscale modelling, data–model fusion and integration of organ physiology in the clinic: ventricular cardiac mechanics. *Interface focus*, 6(2):20150083, 2016.

[21] RH Clayton, Olivier Bernus, EM Cherry, Hans Dierckx, FH Fenton, L Mirabella, AV Panfilov, Frank B Sachse, G Seemann, and H Zhang. Models of cardiac tissue electrophysiology: progress, challenges and open questions. *Progress in biophysics and molecular biology*, 104(1-3):22–48, 2011.

[22] Stefan de Haan, Thomas A Meijers, Paul Knaapen, Aernout M Beek, Albert C van Rossum, and Cornelis P Allaart. Scar size and characteristics assessed by cmr predict ventricular arrhythmias in ischaemic cardiomyopathy: comparison of previously validated models. *Heart*, pages heartjnl–2011, 2011.

[23] Dongdong Deng, Hermenegild J Arevalo, Adityo Prakosa, David J Callans, and Natalia A Trayanova. A feasibility study of arrhythmia risk prediction in patients with myocardial infarction and preserved ejection fraction. *EP Europace*, 18(suppl_4):iv60–iv66, 2016.

[24] Rubén Doste, David Soto-Iglesias, Gabriel Bernardino, Rafael Sebastian, Sophie Giffard-Roisin, Rocio Cabrera-Lozoya, Maxime Sermesant, Antonio Berruezo, Damián Sánchez-Quintana, and Oscar Camara. A rule-based method to model myocardial fiber orientation for simulating ventricular outflow tract arrhythmias. In *International Conference on Functional Imaging and Modeling of the Heart*, pages 344–353. Springer, 2017.

[25] Dirk Durrer, R Th Van Dam, GE Freud, MJ Janse, FL Meijler, and RC Arzbaecher. Total excitation of the isolated human heart. *Circulation*, 41(6):899–912, 1970.

[26] Flavio Fenton and Alain Karma. Vortex dynamics in three-dimensional continuous myocardium with fiber rotation: Filament instability and fibrillation. *Chaos: An Interdisciplinary Journal of Nonlinear Science*, 8(1):20–47, 1998.

[27] Glenn I Fishman, Sumeet S Chugh, John P DiMarco, Christine M Albert, Mark E Anderson, Robert O Bonow, Alfred E Buxton, Peng-Sheng Chen, Mark Estes, Xavier Jouven, Raymond Kwong, David A Lathrop, Mascette, Alice M, Jeanne M Nerbonne, Brian O'rourke, Richard L Page, Dan M Roden, David S Rosenbaum, Nona Sotoodehnia, and Natalia A Trayanova. Sudden cardiac death prediction and prevention: report from a national heart, lung, and blood institute and heart rhythm society workshop. *Circulation*, 122(22):2335–2348, 2010.

[28] Andrew S Flett, Jonathan Hasleton, Christopher Cook, Derek Hausenloy, Giovanni Quarta, Cono Ariti, Vivek Muthurangu, and James C Moon. Evaluation of techniques for the quantification of myocardial scar of differing etiology using cardiac magnetic resonance. *JACC: cardiovascular imaging*, 4(2):150–156, 2011.

[29] Jeffrey J Fox, Jennifer L McHarg, and Robert F Gilmour Jr. Ionic mechanism of electrical alternans. *American Journal of Physiology-Heart and Circulatory Physiology*, 282(2):H516–H530, 2002.

[30] P Colli Franzone, LF Pavarino, and B Taccardi. Simulating patterns of excitation, repolarization and action potential duration with cardiac bidomain and monodomain models. *Mathematical biosciences*, 197(1):35–66, 2005.

[31] Daniel García-León, Mariña López-Yunta, Jose-Manuel Alsonso-Alzamán, Manuel Marina-Breysse, Jorge G. Quinatnilla, Javier Sánchez-González, Carlos Galán-Arriola, Borja Ibañez, Julián Pérez-Villacastín, Nicassio Pérez-Castellano, José Jalife, Mariano Vázquez, Jazmín Aguado-Sierra, and David Filgueiras-Rama. Cardiac fiber disorganization determines the arrhythmia risk and ventricular tachycardia features after myocardial infarction.

[32] Larraitz Gaztañaga, Francis E Marchlinski, and Brian P Betensky. Mecanismos de las arritmias cardiacas. *Revista Española de Cardiología*, 65(2):174–185, 2012.

[33] Alan L Hodgkin and Andrew F Huxley. A quantitative description of membrane current and its application to conduction and excitation in nerve. *The Journal of physiology*, 117(4):500–544, 1952.

[34] Guillaume Houzeaux, Raúl de la Cruz, Herbert Owen, and Mariano Vázquez. Parallel uniform mesh multiplication applied to a navier–stokes solver. *Computers & Fluids*, 80:142–151, 2013.

[35] Guillaume Houzeaux, Mariano Vázquez, Romain Aubry, and José María Cela. A massively parallel fractional step solver for incompressible flows. *Journal of Computational Physics*, 228(17):6316–6332, 2009.

[36] EW Hsu, AL Muzikant, SA Matulevicius, RC Penland, and CS Henriquez. Magnetic resonance myocardial fiber-orientation mapping with direct histological correlation. *American Journal of Physiology-Heart and Circulatory Physiology*, 274(5):H1627–H1634, 1998.

[37] Daniel E Hurtado, Sebastián Castro, and Pedro Madrid. Uncertainty quantification of two models of cardiac electromechanics. *International journal for numerical methods in biomedical engineering*, 2017.

[38] Borja Ibanez, Stefan James, Stefan Agewall, Manuel J Antunes, Chiara Bucciarelli-Ducci, Héctor Bueno, Alida LP Caforio, Filippo Crea, John A Goudevenos, Sigrun Halvorsen, et al. 2017 esc guidelines for the management of acute myocardial infarction in patients presenting with st-segment elevation: The task force for the management of acute myocardial infarction in patients presenting with st-segment elevation of the european society of cardiology (esc). *European heart journal*, 39(2):119–177, 2017.

[39] Hangyi Jiang, Peter CM Van Zijl, Jinsuh Kim, Godfrey D Pearlson, and Susumu Mori. Dtistudio: resource program for diffusion tensor

computation and fiber bundle tracking. *Computer methods and programs in biomedicine*, 81(2):106–116, 2006.

[40] Rashed Karim, R James Housden, Mayuragoban Balasubramaniam, Zhong Chen, Daniel Perry, Ayesha Uddin, Yosra Al-Beyatti, Ebrahim Palkhi, Prince Acheampong, Samantha Obom, et al. Evaluation of current algorithms for segmentation of scar tissue from late gadolinium enhancement cardiovascular magnetic resonance of the left atrium: an open-access grand challenge. *Journal of Cardiovascular Magnetic Resonance*, 15(1):105, 2013.

[41] George Karypis and Vipin Kumar. Multilevelk-way partitioning scheme for irregular graphs. *Journal of Parallel and Distributed computing*, 48(1):96–129, 1998.

[42] Raymond J Kim, David S Fieno, Todd B Parrish, Kathleen Harris, Enn-Ling Chen, Orlando Simonetti, Jeffrey Bundy, J Paul Finn, Francis J Klocke, and Robert M Judd. Relationship of mri delayed contrast enhancement to irreversible injury, infarct age, and contractile function. *Circulation*, 100(19):1992–2002, 1999.

[43] André G Kléber and Yoram Rudy. Basic mechanisms of cardiac impulse propagation and associated arrhythmias. *Physiological reviews*, 84(2):431–488, 2004.

[44] Igor Klem, Jonathan W Weinsaft, Tristram D Bahnson, Don Hegland, Han W Kim, Brenda Hayes, Michele A Parker, Robert M Judd, and Raymond J Kim. Assessment of myocardial scarring improves risk stratification in patients evaluated for cardiac defibrillator implantation. *Journal of the American College of Cardiology*, 60(5):408–420, 2012.

[45] Patrick M Knupp. Algebraic mesh quality metrics for unstructured initial meshes. *Finite Elements in Analysis and Design*, 39(3):217–241, 2003.

[46] François Labelle and Jonathan Richard Shewchuk. Isosurface stuffing: fast tetrahedral meshes with good dihedral angles. In *ACM Transactions on Graphics (TOG)*, volume 26, page 57. ACM, 2007.

[47] Pierre Lafortune, Ruth Arís, Mariano Vázquez, and Guillaume Houzeaux. Coupled electromechanical model of the heart: parallel finite element formulation. *International journal for numerical methods in biomedical engineering*, 28(1):72–86, 2012.

[48] CD Lloyd. Assessing the effect of integrating elevation data into the estimation of monthly precipitation in great britain. *Journal of Hydrology*, 308(1-4):128–150, 2005.

[49] Mariña López-Yunta, Daniel García-León, Jose-Manuel Alsonso-Alzamán, Manuel Marina-Breysse, Jorge G. Quinatnilla, Javier Sánchez-González, Carlos Galán-Arriola, Victoria Cañadas-Godoy, Daniel Enriquez-Vazquez, Carlos Torres, Borja Ibañez, Julián Pérez-Villacastín, Nicassio Pérez-Castellano, José Jalife, Mariano Vázquez, Jazmín Aguado-Sierra, and David Filgueiras-Rama. Implications of imaging approaches in biventricular substrate characterization after myocardial infarction.

[50] Ching-hsing Luo and Yoram Rudy. A model of the ventricular cardiac action potential. depolarization, repolarization, and their interaction. *Circulation research*, 68(6):1501–1526, 1991.

[51] Michael Lynch, Ovidiu Ghita, and Paul F Whelan. Automatic segmentation of the left ventricle cavity and myocardium in mri data. *Computers in biology and medicine*, 36(4):389–407, 2006.

[52] Martina Perazzolo Marra, Loira Leoni, Barbara Bauce, Francesco Corbetti, Alessandro Zorzi, Federico Migliore, Maria Silvano, Ilaria Rigato, Francesco Tona, Giuseppe Tarantini, et al. Imaging study of ventricular scar in arrhythmogenic right ventricular cardiomyopathyclinical perspective: Comparison of 3d standard electroanatomical voltage mapping and contrast-enhanced cardiac magnetic resonance. *Circulation: Arrhythmia and Electrophysiology*, 5(1):91–100, 2012.

[53] Daniel R Messroghli, Aleksandra Radjenovic, Sebastian Kozerke, David M Higgins, Mohan U Sivananthan, and John P Ridgway. Modified look-locker inversion recovery (molli) for high-resolution t1 mapping of the heart. *Magnetic resonance in medicine*, 52(1):141–146, 2004.

[54] MPI Forum. Message Passing Interface (MPI) URL. `http://www.mpi-forum.org/`.

[55] Jinichi Nagumo, Suguru Arimoto, and Shuji Yoshizawa. An active pulse transmission line simulating nerve axon. *Proceedings of the IRE*, 50(10):2061–2070, 1962.

[56] Shiro Nakahara, Marmar Vaseghi, Rafael J Ramirez, Carissa G Fonseca, Chi K Lai, J Paul Finn, Aman Mahajan, Noel G Boyle, and Kalyanam Shivkumar. Characterization of myocardial scars: electrophysiological imaging correlates in a porcine infarct model. *Heart Rhythm*, 8(7):1060–1067, 2011.

[57] Martyn P Nash and Alexander V Panfilov. Electromechanical model of excitable tissue to study reentrant cardiac arrhythmias. *Progress in biophysics and molecular biology*, 85(2-3):501–522, 2004.

[58] Steven A Niederer, Eric Kerfoot, Alan P Benson, Miguel O Bernabeu, Olivier Bernus, Chris Bradley, Elizabeth M Cherry, Richard Clayton, Flavio H Fenton, Alan Garny, et al. Verification of cardiac tissue electrophysiology simulators using an n-version benchmark. *Phil. Trans. R. Soc. A*, 369(1954):4331–4351, 2011.

[59] Sonia Nielles-Vallespin, Choukri Mekkaoui, Peter Gatehouse, Timothy G Reese, Jennifer Keegan, Pedro F Ferreira, Steve Collins, Peter Speier, Thorsten Feiweier, Ranil Silva, et al. In vivo diffusion tensor mri of the human heart: reproducibility of breath-hold and navigator-based approaches. *Magnetic resonance in medicine*, 70(2):454–465, 2013.

[60] Jana M Nührich, Lukas Kaiser, Ruken Özge Akbulak, Benjamin N Schäffer, Christian Eickholt, Michael Schwarzl, Pawel Kuklik, Julia Moser, Mario Jularic, Stephan Willems, et al. Substrate characterization and catheter ablation in patients with scar-related ventricular tachycardia using ultra high-density 3d mapping. *Journal of cardiovascular electrophysiology*, 2017.

[61] Thomas O'Hara, László Virág, András Varró, and Yoram Rudy. Simulation of the undiseased human cardiac ventricular action potential: model formulation and experimental validation. *PLoS computational biology*, 7(5):e1002061, 2011.

[62] Farhad Pashakhanloo, Daniel A Herzka, Hiroshi Ashikaga, Susumu Mori, Neville Gai, David A Bluemke, Natalia A Trayanova, and Elliot R McVeigh. Myofiber architecture of the human atria as revealed by submillimeter diffusion tensor imaging. *Circulation: Arrhythmia and Electrophysiology*, 9(4):e004133, 2016.

[63] Pras Pathmanathan and Richard A Gray. Ensuring reliability of safety-critical clinical applications of computational cardiac models. *Frontiers in physiology*, 4:358, 2013.

[64] Emerson C Perin, Guilherme V Silva, Rogerio Sarmento-Leite, Andre LS Sousa, Marcus Howell, Raja Muthupillai, Brenda Lambert, William K Vaughn, and Scott D Flamm. Assessing myocardial viability and infarct transmurality with left ventricular electromechanical mapping in patients with stable coronary artery disease. *Circulation*, 106(8):957–961, 2002.

[65] Sebastiaan RD Piers, Carine FB van Huls van Taxis, Qian Tao, Rob J van der Geest, Said F Askar, Hans-Marc J Siebelink, Martin J Schalij, and Katja Zeppenfeld. Epicardial substrate mapping for ventricular tachycardia ablation in patients with non-ischaemic cardiomyopathy: a new algorithm to differentiate between scar and viable myocardium developed by simultaneous integration of computed tomography and contrast-enhanced magnetic resonance imaging. *European heart journal*, 34(8):586–596, 2012.

[66] Robert Plonsey and Dennis B Heppner. Considerations of quasi-stationarity in electrophysiological systems. *The Bulletin of mathematical biophysics*, 29(4):657–664, 1967.

[67] Mark Potse, Bruno Dubé, Jacques Richer, Alain Vinet, and Ramesh M Gulrajani. A comparison of monodomain and bidomain reaction-diffusion models for action potential propagation in the human heart. *IEEE Transactions on Biomedical Engineering*, 53(12):2425–2435, 2006.

[68] Leo Priebe and Dirk J Beuckelmann. Simulation study of cellular electric properties in heart failure. *Circulation research*, 82(11):1206–1223, 1998.

[69] Jordan Ringenberg, Makarand Deo, Vijay Devabhaktuni, David Filgueiras-Rama, Gonzalo Pizarro, Borja Ibañez, Omer Berenfeld, Pamela Boyers, and Jeffrey Gold. Automated segmentation and reconstruction of patient-specific cardiac anatomy and pathology from in vivo mri. *Measurement Science and Technology*, 23(12):125405, 2012.

[70] Byron N Roberts, Pei-Chi Yang, Steven B Behrens, Jonathan D Moreno, and Colleen E Clancy. Computational approaches to understand cardiac electrophysiology and arrhythmias. *American Journal of Physiology-Heart and Circulatory Physiology*, 303(7):H766–H783, 2012.

[71] Blanca Rodríguez, James C Eason, and Natalia Trayanova. Differences between left and right ventricular anatomy determine the types of reentrant circuits induced by an external electric shock. a rabbit heart simulation study. *Progress in biophysics and molecular biology*, 90(1-3):399–413, 2006.

[72] Bradley J Roth. Meandering of spiral waves in anisotropic cardiac tissue. *Physica D: Nonlinear Phenomena*, 150(1-2):127–136, 2001.

[73] Sébastien Roujol, Tamer A Basha, Alex Tan, Varun Khanna, Raymond H Chan, Mehdi H Moghari, Hussein Rayatzadeh, Jaime L

Shaw, Mark E Josephson, and Reza Nezafat. Improved multimodality data fusion of late gadolinium enhancement mri to left ventricular voltage maps in ventricular tachycardia ablation. *IEEE Transactions on Biomedical Engineering*, 60(5):1308–1317, 2013.

[74] Eloi Ruiz-Gironés, Xevi Roca, and Josep Sarrate. The receding front method applied to hexahedral mesh generation of exterior domains. *Engineering with computers*, 28(4):391–408, 2012.

[75] Philip T Sager, Gary Gintant, J Rick Turner, Syril Pettit, and Norman Stockbridge. Rechanneling the cardiac proarrhythmia safety paradigm: a meeting report from the cardiac safety research consortium. *American heart journal*, 167(3):292–300, 2014.

[76] Pasquale Santangeli and Francis E Marchlinski. Substrate mapping for unstable ventricular tachycardia. *Heart Rhythm*, 13(2):569–583, 2016.

[77] Alfonso Santiago. *Fluid-Electro-Mechanical model of the human heart for supercomputers.* PhD thesis, Universitat Politècnica de Catalunya.

[78] André Schmidt, Clerio F Azevedo, Alan Cheng, Sandeep N Gupta, David A Bluemke, Thomas K Foo, Gary Gerstenblith, Robert G Weiss, Eduardo Marbán, Gordon F Tomaselli, et al. Infarct tissue heterogeneity by magnetic resonance imaging identifies enhanced cardiac arrhythmia susceptibility in patients with left ventricular dysfunction. *Circulation*, 115(15):2006–2014, 2007.

[79] Karl H Schuleri, Marco Centola, Richard T George, Luciano C Amado, Kristine S Evers, Kakuya Kitagawa, Andrea L Vavere, Robert Evers, Joshua M Hare, Christopher Cox, et al. Characterization of peri-infarct zone heterogeneity by contrast-enhanced multidetector computed tomography: a comparison with magnetic resonance imaging. *Journal of the American College of Cardiology*, 53(18):1699–1707, 2009.

[80] E Schulte, LM Ross, and ED Lamperti. *Thieme Atlas of Anatomy: Neck and Internal Organs*, volume 4. Thieme, 2006.

[81] Jeanette Schulz-Menger, David A Bluemke, Jens Bremerich, Scott D Flamm, Mark A Fogel, Matthias G Friedrich, Raymond J Kim, Florian von Knobelsdorff-Brenkenhoff, Christopher M Kramer, Dudley J Pennell, et al. Standardized image interpretation and post processing in cardiovascular magnetic resonance: Society for cardiovascular magnetic resonance (scmr) board of trustees task force on standardized post processing. *Journal of Cardiovascular Magnetic Resonance*, 15(1):35, 2013.

[82] David F Scollan, Alex Holmes, Raimond Winslow, and John Forder. Histological validation of myocardial microstructure obtained from diffusion tensor magnetic resonance imaging. *American Journal of Physiology-Heart and Circulatory Physiology*, 275(6):H2308–H2318, 1998.

[83] James A Sethian. A fast marching level set method for monotonically advancing fronts. *Proceedings of the National Academy of Sciences*, 93(4):1591–1595, 1996.

[84] David Soto-Iglesias, Constantine Butakoff, David Andreu, Juan Fernández-Armenta, Antonio Berruezo, and Oscar Camara. Integration of electro-anatomical and imaging data of the left ventricle: an evaluation framework. *Medical image analysis*, 32:131–144, 2016.

[85] AF Stanley Kent. Observations on the auriculo-ventricular junction of the mammalian heart. *Quarterly Journal of Experimental Physiology: Translation and Integration*, 7(2):193–195, 1913.

[86] CJ Stimpson, CD Ernst, P Knupp, PP Pébay, and D Thompson. The verdict library reference manual. *Sandia National Laboratories Technical Report*, 9, 2007.

[87] Daniel D Streeter and David L Bassett. An engineering analysis of myocardial fiber orientation in pig's left ventricle in systole. *The Anatomical Record*, 155(4):503–511, 1966.

[88] Daniel D Streeter, Henry M Spotnitz, Dali P Patel, John Ross, and Edmund H Sonnenblick. Fiber orientation in the canine left ventricle during diastole and systole. *Circulation research*, 24(3):339–347, 1969.

[89] Joakim Sundnes, Glenn Terje Lines, Xing Cai, Bjørn Frederik Nielsen, Kent-Andre Mardal, and Aslak Tveito. *Computing the electrical activity in the heart*, volume 1. Springer Science & Business Media, 2007.

[90] Yasuaki Tanaka, Martin Genet, Lik Chuan Lee, Alastair J Martin, Richard Sievers, and Edward P Gerstenfeld. Utility of high-resolution electroanatomic mapping of the left ventricle using a multispline basket catheter in a swine model of chronic myocardial infarction. *Heart Rhythm*, 12(1):144–154, 2015.

[91] KHWJ Ten Tusscher, Denis Noble, Peter-John Noble, and Alexander V Panfilov. A model for human ventricular tissue. *American Journal of Physiology-Heart and Circulatory Physiology*, 286(4):H1573–H1589, 2004.

[92] Natalia A Trayanova. Whole-heart modeling: applications to cardiac electrophysiology and electromechanics. *Circulation research*, 108(1):113–128, 2011.

[93] Natalia A Trayanova and Patrick M Boyle. Advances in modeling ventricular arrhythmias: from mechanisms to the clinic. *Wiley Interdisciplinary Reviews: Systems Biology and Medicine*, 6(2):209–224, 2014.

[94] Natalia A Trayanova, Patrick M Boyle, and Plamen P Nikolov. Personalized imaging and modeling strategies for arrhythmia prevention and therapy. *Current Opinion in Biomedical Engineering*, 2017.

[95] Cory M Tschabrunn, Sebastien Roujol, Nicole C Dorman, Reza Nezafat, Mark E Josephson, and Elad Anter. High-resolution mapping of ventricular scar: comparison between single and multielectrode catheters. *Circulation: Arrhythmia and Electrophysiology*, 9(6):e003841, 2016.

[96] Cory M Tschabrunn, Sébastien Roujol, Reza Nezafat, Beverly Faulkner-Jones, Alfred E Buxton, Mark E Josephson, and Elad Anter. A swine model of infarct-related reentrant ventricular tachycardia: electroanatomic, magnetic resonance, and histopathological characterization. *Heart Rhythm*, 13(1):262–273, 2016.

[97] Leslie Tung. *A bi-domain model for describing ischemic myocardial dc potentials.* PhD thesis, Massachusetts Institute of Technology, 1978.

[98] Roderick Tung, Steve Kim, Daigo Yagishita, Marmar Vaseghi, Daniel B Ennis, Sarah Ouadah, Olujimi A Ajijola, Jason S Bradfield, Srijoy Mahapatra, Paul Finn, et al. Scar voltage threshold determination using ex vivo magnetic resonance imaging integration in a porcine infarct model: Influence of interelectrode distances and three-dimensional spatial effects of scar. *Heart Rhythm*, 13(10):1993–2002, 2016.

[99] Fijoy Vadakkumpadan, Hermenegild Arevalo, Can Ceritoglu, Michael Miller, and Natalia Trayanova. Image-based estimation of ventricular fiber orientations for personalized modeling of cardiac electrophysiology. *IEEE transactions on medical imaging*, 31(5):1051–1060, 2012.

[100] Mariano Vazquez, R Arís, G Houzeaux, R Aubry, P Villar, J Garcia-Barnés, D Gil, and F Carreras. A massively parallel computational electrophysiology model of the heart. *International Journal for*

Numerical Methods in Biomedical Engineering, 27(12):1911–1929, 2011.

[101] Mariano Vázquez, Guillaume Houzeaux, Seid Koric, Antoni Artigues, Jazmin Aguado-Sierra, Ruth Arís, Daniel Mira, Hadrien Calmet, Fernando Cucchietti, Herbert Owen, et al. Alya: Multiphysics engineering simulation toward exascale. *Journal of Computational Science*, 14:15–27, 2016.

[102] Jose Vicente, Lars Johannesen, Loriano Galeotti, and David G Strauss. Mechanisms of sex and age differences in ventricular repolarization in humans. *American heart journal*, 168(5):749–756, 2014.

[103] Adrianus P Wijnmaalen, Rob J van der Geest, Carine FB van Huls van Taxis, Hans-Marc J Siebelink, Lucia JM Kroft, Jeroen J Bax, Johan HC Reiber, Martin J Schalij, and Katja Zeppenfeld. Head-to-head comparison of contrast-enhanced magnetic resonance imaging and electroanatomical voltage mapping to assess post-infarct scar characteristics in patients with ventricular tachycardias: real-time image integration and reversed registration. *European heart journal*, 32(1):104–114, 2010.

[104] Gavin P Winston. The physical and biological basis of quantitative parameters derived from diffusion mri. *Quantitative imaging in medicine and surgery*, 2(4):254, 2012.

[105] Leik Woie, Trygve Eftestøl, Kjersti Engan, Jan Terje Kvaløy, Dennis WT Nilsen, and Stein Ørn. The heart rate of ventricular tachycardia following an old myocardial infarction is inversely related to the size of scarring. *Europace*, 13(6):864–868, 2011.

[106] Andrew T Yan, Adolphe J Shayne, Kenneth A Brown, Sandeep N Gupta, Carmen W Chan, Tuan M Luu, Marcelo F Di Carli, H Glenn Reynolds, William G Stevenson, and Raymond Y Kwong. Characterization of the peri-infarct zone by contrast-enhanced cardiac magnetic resonance imaging is a powerful predictor of post–myocardial infarction mortality. *Circulation*, 114(1):32–39, 2006.

[107] Fang-Cheng Yeh, Timothy D Verstynen, Yibao Wang, Juan C Fernández-Miranda, and Wen-Yih Isaac Tseng. Deterministic diffusion fiber tracking improved by quantitative anisotropy. *PloS one*, 8(11):e80713, 2013.